UCONN LIBRARY

University of Connecticut
OpenCommons@UConn

Doctoral Dissertations | University of Connecticut Graduate School

9-4-2014

Comprehensive Numerical Modeling of Heat Pipe-Assisted Latent Heat Thermal Energy Storage Systems

Nourouddin Sharifi
noursharifi@yahoo.com

Follow this and additional works at: https://opencommons.uconn.edu/dissertations

Recommended Citation
Sharifi, Nourouddin, "Comprehensive Numerical Modeling of Heat Pipe-Assisted Latent Heat Thermal Energy Storage Systems" (2014). *Doctoral Dissertations*. 553.
https://opencommons.uconn.edu/dissertations/553

Comprehensive Numerical Modeling of Heat Pipe-Assisted Latent Heat Thermal Energy Storage Systems

Nourouddin Sharifi, PhD

University of Connecticut, 2014

Latent heat thermal energy storage (LHTES) is capable of higher energy storage densities effectively reducing storage volume and cost compared to other thermal energy storage systems. However, most inexpensive phase change materials (PCMs) exhibit low thermal conductivities, potentially limiting the rates of heat transfer, and consequently, the use of LHTES in a variety of applications. To compensate for this major drawback, three different approaches to improve heat transfer rates are presented in this work: (i) utilization of fins, (ii) incorporation of heat pipes (HPs), and (iii) use of combined HP/foils. These heat transfer enhancements are investigated both experimentally and numerically. The numerical model simulates the melting augmentation of a PCM housed within an internally-finned metal enclosure, followed by a derivation of analytical correlations. The experiments are conducted to generate and report data associated with the outward melting of a PCM induced by a heated rod under various tilt angles to investigate three dimensional effects. The benefits associated with exploiting HPs in LHTESs are also numerically investigated. A detailed and efficient numerical model is developed to simulate the conjugate and transient transport phenomena including vapor-liquid and melting-solidification phase changes in the HP-PCM system. The numerical model is extended to consider different modes of operation including charging-only, simultaneous charging and discharging, and discharging-only. Finally, a combined HP-Foil-PCM system is investigated for further improvement of heat transfer rates experimentally as well as computationally. It was found that, in general, HPs exhibit higher heat transfer rates to/from the PCM compared to fins, especially when it is used in combination with foils (HP-Foil).

Comprehensive Numerical Modeling of Heat Pipe-Assisted Latent Heat Thermal Energy Storage Systems

Nourouddin Sharifi

B.S., Ferdowsi University of Mashhad, 2002

M.S., University of Tehran, 2005

A Dissertation

Submitted in Partial Fulfillment of the

Requirement for the Degree of Doctor of Philosophy

at the

University of Connecticut

2014

APPROVAL PAGE

Doctor of Philosophy Dissertation

Comprehensive Numerical Modeling of Heat Pipe-Assisted Latent Heat Thermal Energy Storage Systems

Presented by:

Nourouddin Sharifi, B.S., M.S.

Major Advisor_____
Amir Faghri

Associate Advisor_____
Theodore L. Bergman

Associate Advisor_____
Ugur Pasaogullari

Associate Advisor_____
Tai-Hsi Fan

Associate Advisor_____
Tianfeng Lu

Associate Advisor_____
Michael Pettes

University of Connecticut

2014

Acknowledgements

I would like to take this opportunity to thank the individuals who have contributed to my PhD career. I would like to express my gratitude to Professor Amir Faghri for his guidance, support and encouragement over the past five and a half years. Without his advice and persistent help this work would not have been possible.

I would like to extent my appreciation to my associate advisors, Professors Theodore L. Bergman, Ugur Pasaogullari, Tai-Hsi Fan, Tianfeng Lu and Michael Pettes. I am grateful for your invaluable impact on my education through your courses, suggestions, and advices.

In particular, I would also like to acknowledge and thank Professor Theodore L. Bergman for his guidance with my research, scientific advice, and knowledge, and many insightful discussions and suggestions. It is an honor to have worked with Professor Bergman during my PhD career and I have learned a lot from him.

To all my fellow lab-mates, thank you for your support, assistance, encouragement, and friendship with my school and research efforts.

Last but not least, I would like to thank my family for their financial, spiritual and encouraging support throughout my life.

Table of Contents

List of Tables

List of Figures

Chapter 1. Enhancement of PCM Melting in Enclosures with Horizontally-Finned Internal Surfaces

A numerical model for simulating the melting of a phase change material (PCM) housed within an internally-finned metal enclosure is developed. A finite volume approach, utilizing the temperature-transforming model for phase change, is used to predict the conjugate heat transfer in the cavity walls and fins, as well as within the molten PCM. The influence of the number of fins, the fin length and thickness, and the hot wall temperature on the melting process is reported. With horizontal fins, rapid melting occurs during the early stages of the phase change, followed by a second, slow melting regime. Analytical correlations are developed that can be used to quickly estimate melting rates during both melting regimes, and it is shown that the predictions of the correlations are in good agreement with those of the detailed model.

1.1. Introduction

Latent heat thermal energy storage (LHTES) has advantages over various sensible thermal energy storage (STES) or chemical energy storage (CTES) techniques. Relative to STES, LHTES has a high energy density and, in principle, allows for energy storage at a nearly constant (phase change) temperature. However, as is well known many phase change materials (PCMs) have low thermal conductivities, which leads to large temperature differences between various heat transfer surfaces and the solid-liquid interface of the PCM.

Reviews of LHTES, heat transfer in PCMs, and heat transfer augmentation techniques to promote melting (or solidification) of PCMs are available [1-4]. Strategies to counteract the low thermal conductivities of PCMs include but are not limited to (i) use of high thermal

conductivity porous matrices embedded with PCM [5, 6], (ii) incorporation of dispersed high thermal conductivity particles within the PCM [7], (iii) micro-encapsulation of the PCM [8], and (iv) use of extended surfaces and/or heat pipes [9-16].

This study is focused on the use of fins to enhance heat transfer in a low thermal conductivity PCM during the melting process. In related work, Lacroix and Benmadda [11] considered PCM melting in a rectangular enclosure with horizontal fins extending into the PCM from a heated wall. A two-dimensional enthalpy model was used to solve the phase change problem numerically. The study considered the effect of the number and length of fins on the melting rate. It was concluded that a few longer fins were more effective in increasing the melting rate than a large number of shorter fins. In a related study, Lacroix and Benmadda [12] considered vertical fins. It was found that the onset of natural convection in the melt was delayed when the distance between the fins was decreased. According to their results, the optimum fin spacing decreases as the Rayleigh number increases.

Huang et al. [13] numerically and experimentally investigated fin-enhanced PCM melting to cool photovoltaic devices. An improvement in the thermal performance was achieved by using metal fins. Heat transfer within the PCM was augmented through the effect of natural convection within the molten PCM. However, use of a large number of fins was found to limit advection within the molten PCM, decreasing the beneficial effects of natural convection on reducing the thermal resistance between the hot wall and the PCM solid-liquid interface.

Shatikian et al. [14] numerically simulated PCM melting in a thermal energy storage unit using a finite volume approach and enthalpy model. Their predictions illustrate how the melting rates are affected by geometric parameters such as fin length, fin thickness, and fin spacing. It was concluded that the melting rate increases when the fins were spaced closely. At higher fin-

to-fin spacing the fluid motion is enhanced. As in other studies, it was noted that fluid motion in the molten PCM was suppressed for cases involving tightly-packed fins. Likewise, Akhilesh et al. [15] numerically studied a rectangular module with vertical fins, heated from above. Heat transfer by conduction only was included in the study. The analysis showed that more fins increase the rate at which energy can be stored in the melting PCM. However, beyond a critical value, increasing the number of fins no longer improved performance. Gharebagi and Sezai [16] considered an enclosure with vertical fins added to a horizontal heated wall. The results indicate that heat transfer rates to the melting PCM can be increased by adding fins. Also, vertical heated walls with horizontal fins exhibited better performance than horizontal heated walls with vertical fins.

From the computational perspective, predicting PCM melting remains a challenge because of two main concerns [17-22]. The first is the relatively long computational time needed to generate accurate predictions, especially for high Rayleigh numbers ($\approx 10^9$). Second, inconsistencies in the solid-liquid interface location have been reported by numerous investigators.

Based upon the literature review, the objectives of this study are to: (i) use an efficient approach to simulate heat transfer during PCM melting in an enclosure including the effects of transient conduction in the enclosure walls and fins, (ii) investigate the sensitivity of PCM melting on various fin parameters, (iii) develop physics-based analytical expressions that can be used to quickly estimate the PCM melting rate in enclosures equipped with fins and (iv) validate the new analytical expressions through comparison with the numerical predictions.

1.2. The model

The $H \times H$ computational domain, shown in Fig. 1.1, includes both PCM (octadecane) and the solid material of the enclosure and fins (copper). The domain shown corresponds to half of the physical domain, which is symmetric about $x = H$. Walls of thickness t_w, and horizontal fins of length L_f and thickness t_f are included. Initially, the PCM is solid at its fusion temperature and melting is initiated when the temperature at $x = 0$ is raised to T_h. The thermophysical properties of octadecane and copper are provided in Table 1.1. The cavity dimension is $H = 20$ mm.

1.2.1. Governing equations and the temperature transforming model

To develop the governing equations, the following assumptions have been made. Heat transfer processes are two-dimensional. The PCM (and copper) is a pure, homogeneous substance with constant thermophysical properties in each phase. Flow within the molten PCM, which is a Boussinesq and Newtonian fluid, is incompressible and laminar with negligible viscous dissipation. Finally, the solid PCM is assumed to remain fixed spatially. That is, possible close-contact melting associated with the solid falling to the floor of the enclosure is not modeled. Similarly, PCM expansion upon melting is not accounted for.

Based on foregoing assumptions, the governing equations for the PCM are as follows [23].

Continuity equation

$$\frac{\partial(\rho u)}{\partial x} + \frac{\partial(\rho v)}{\partial y} = 0 \tag{1}$$

Momentum equations

$$\frac{\partial(\rho u)}{\partial t}+\frac{\partial\left(\rho u^{2}\right)}{\partial x}+\frac{\partial(\rho u v)}{\partial y}=-\frac{\partial p}{\partial x}+\frac{\partial}{\partial x}\left(\mu\frac{\partial u}{\partial x}\right)+\frac{\partial}{\partial y}\left(\mu\frac{\partial u}{\partial y}\right) \tag{2}$$

$$\frac{\partial(\rho v)}{\partial t}+\frac{\partial(\rho u v)}{\partial x}+\frac{\partial\left(\rho v^{2}\right)}{\partial y}=-\frac{\partial p}{\partial y}+\frac{\partial}{\partial x}\left(\mu\frac{\partial v}{\partial x}\right)+\frac{\partial}{\partial y}\left(\mu\frac{\partial v}{\partial y}\right)+\rho g\,\beta(T-T_{m}) \tag{3}$$

Energy equation

$$\frac{\partial(\rho h)}{\partial t}+\frac{\partial(\rho u h)}{\partial x}+\frac{\partial(\rho v h)}{\partial y}=\frac{\partial}{\partial x}\left(k\frac{\partial T}{\partial x}\right)+\frac{\partial}{\partial y}\left(k\frac{\partial T}{\partial y}\right) \tag{4}$$

The velocities are zero in the solid phase. Defining a scaled temperature as $T^{*}=T-T_{m}$, and expressing the enthalpy through application of the temperature transforming model [23-30],

$$h=cT^{*}+s \tag{5}$$

where, for an arbitrary small temperature different δT,

$$c=\begin{cases}c_{s} & T^{*}<-\delta T\\ \dfrac{c_{s}+c_{\ell}}{2}+\dfrac{h_{s\ell}}{2\delta T} & -\delta T\le T^{*}\le\delta T\\ c_{\ell} & T^{*}>\delta T\end{cases} \tag{6}$$

$$s=\begin{cases}c_{s}\delta T & T^{*}<-\delta T\\ \dfrac{c_{s}+c_{\ell}}{2}\delta T+\dfrac{h_{s\ell}}{2} & -\delta T\le T^{*}\le\delta T\\ c_{s}\delta T+h_{s\ell} & T^{*}>\delta T\end{cases} \tag{7}$$

With the temperature transforming model, the energy equation can be written as

$$\frac{\partial(\rho cT^{*})}{\partial t}+\frac{\partial(\rho ucT^{*})}{\partial x}+\frac{\partial(\rho vcT^{*})}{\partial y}=\frac{\partial}{\partial x}\left(k\frac{\partial T^{*}}{\partial x}\right)+\frac{\partial}{\partial y}\left(k\frac{\partial T^{*}}{\partial y}\right)-\left[\frac{\partial(\rho s)}{\partial t}+\frac{\partial(\rho us)}{\partial x}+\frac{\partial(\rho vs)}{\partial y}\right] \tag{8}$$

where the properties are evaluated separately for each phase of the PCM,

$$k=\begin{cases}k_s & T^*<-\delta T\\ k_s+(k_\ell-k_s)\dfrac{(T^*+\delta T)}{2\delta T} & -\delta T\le T^*\le\delta T\\ k_\ell & T^*>\delta T\end{cases} \tag{9}$$

and each material (copper versus PCM).

The boundary conditions are shown in Fig. 1.1.

1.2.2. Dimensionless Parameters and Equations

Non-dimensionalization of the governing equations, boundary conditions, and geometrical dimensions lead to the following dimensionless parameters.

$$\begin{aligned}&X=\frac{x}{H},Y=\frac{y}{H},U=\frac{uH}{\nu_\ell},V=\frac{\upsilon H}{\nu_\ell},Pr=\frac{\nu}{\alpha},\tau=\frac{\nu_\ell t}{H^2}=Pr_\ell Fo_H,\theta=\frac{T-T_m}{T_h-T_m},\delta\theta=\frac{\delta T}{T_h-T_m},\\ &Ste=\frac{c_\ell(T_h-T_m)}{h_{s\ell}},\ P=\frac{\rho H^2}{\mu_\ell^2}(p+\rho gy),Ra=\frac{g\beta H^3}{\nu_\ell\alpha_\ell}(T_h-T_m),S=\frac{s}{c_\ell(T_h-T_m)},C_{s\ell}=\frac{c_s}{c_\ell},K_{s\ell}=\frac{k_s}{k_\ell},\\ &C_{f\ell}=\frac{(\rho c)_f}{(\rho c)_\ell},K_{f\ell}=\frac{k_f}{k_\ell},T_f=\frac{t_f}{H},\lambda_f=\frac{L_f}{H},T_w=\frac{t_w}{H}\end{aligned} \tag{10}$$

Velocities within the solid phase are zero. Therefore, the dynamic viscosity is expressed as [25, 29]

$$\mu=\begin{cases}\mu_\ell & T^*<-\delta T\\ \mu_\ell+(\mu_\ell-\mu_s)\dfrac{(T^*-\delta T)}{2\delta T} & -\delta T\le T^*\le\delta T\\ \mu_s & T^*>\delta T\end{cases} \tag{11}$$

where μ_s is assigned a large value such as 10^{10}.

The energy equation in walls and fins is

$$\frac{\partial(\rho cT^*)}{\partial t}=\frac{\partial}{\partial x}\left(k\frac{\partial T^*}{\partial x}\right)+\frac{\partial}{\partial y}\left(k\frac{\partial T^*}{\partial y}\right) \tag{12}$$

1.2.3. Numerical methodology

The numerical methodology is described in [30] with the following exceptions. First, the viscosity is treated as described in Eq. (11). Second, advection terms are described by the power law scheme instead of central difference scheme. Diffusion terms are modeled using central differencing [31]. The pressure and energy equations are discretized in fully implicit format and a nonuniform grid is used throughout the computational domain overlaying the PCM as well as the solid walls and fins. All equations are solved with the multigrid solver and utilize a strongly implicit procedure (SIP) as a smoother [32, 33]. Preliminary predictions were performed using grid sizes up to 120 × 120. An 80 × 80 grid with a dimensionless time step of $\tau = 0.01$ was found to be sufficient to achieve grid size and time step independent solutions. A convergence criterion of 10^{-8} was specified for all independent variables.

1.3. Results and Discussion

To facilitate discussion of the predictions, a dimensionless thermal resistance is defined as

$$R_{th}(Ste\,Fo_H) = \frac{\theta(0,Y,SteFo_H) - \min[\theta(1,Y,\ SteFo_H)]}{q^{\circ}(Ste\,Fo_H)} \tag{13}$$

where the dimensionless heat rate is

$$q^{\circ}(Ste\,Fo_H) = \int_0^1 \frac{\partial\theta(0,Y,SteFo_H)}{\partial X}\,dY \tag{14}$$

Predictions associated with thin walls and no fins ($T_w = 0.04$, $\lambda_f = 0$, $Ste = 0.04$, $Ra_H = 3.2 \times 10^5$) are presented in Fig. 1.2. Initially, heat transfer is conduction-dominated and warm temperatures propagate relatively quickly through the copper walls. Correspondingly, at early times the solid-liquid interface propagates away from the walls at a nearly uniform rate (Fig.

1.2a, $SteFo_H = 0.01$). As melting proceeds ($SteFo_H \gtrsim 0.03$), free convection becomes established in the liquid phase, leading to variations in local melting rates along the solid-liquid interface, similar to the experimental observations made by Henze and Humphrey [34]. Representative isotherms and streamlines at $SteFo_H = 0.04$ are shown in Figs. 1.2b and 1.2c, respectively. The simulation proceeds until all of the PCM is melted and, as evident in Fig. 1.2d, the dimensionless heat transfer rate and dimensionless thermal resistance gradually evolve as melting proceeds.

Melting phenomena with thin walls and two fins ($T_w = 0.04$, $\lambda_f = 0.4$, $T_f = 0.04$, $Ste = 0.04$, $Ra_H = 3.2 \times 10^5$) are shown in Fig. 1.3. Again, heat transfer is initially conduction-dominated. For example, at $SteFo_H = 0.01$, the solid-liquid interface exhibits symmetry about $Y = 0.5$, and a melt region coats the walls and fins in a relatively uniform manner. As melting proceeds, free convection becomes established but is influenced by the fins, as evident in the isotherms and streamlines shown in Figs. 1.3b and 1.3c, respectively. As for the case without fins, the dimensionless heat transfer rate (thermal resistance) decays (increases), as shown in Fig. 1.3d. Comparison of Figs. 1.2d and 1.3d reveals that the fins accelerate the melting of the PCM. However, less PCM is available when the fins are present. Hence, a tradeoff exists between (*i*) the speed at which PCM can be melted and (*ii*) the amount of energy that can ultimately be stored in the PCM.

1.3.1. PCM melting rates

The influence of the number of fins, as well as their thickness and length, on the melting rate is shown in Fig. 1.4 ($Ste = 0.04$, $Ra_H = 3.2 \times 10^5$). In Figs. 1.4a and 1.4c, the absolute liquid fraction f_ℓ is defined as the amount of liquid relative to the amount of PCM initially in the enclosure. Hence, $f_\ell = 1$ corresponds to complete melting. In Figs. 1.4b and 1.4d, a *modified*

liquid fraction $\tilde{f}_\ell$ is defined as the amount of liquid relative to the amount of PCM initially contained in the enclosure with no fins; when all the PCM is melted in configurations involving fins, $\tilde{f}_\ell$ attains a final value less than unity. As evident in Fig. 1.4a ($T_w = T_f = 0.04$), incorporation of fins can accelerate melting rates significantly. In each case considered here, increased melting rates occur in response to either (*i*) increasing the number of fins or (*ii*) increasing their length. Note that melting rates associated with $N = 2$ fins of length $\lambda_f = 0.8$ exceed those associated with either two or four fins with $\lambda_f = 0.2$, similar to the observations of Lacroix and Benmadda [11]. Although longer fins hamper natural convection, incorporation of longer fins decreases the total melting time for all cases considered here.

In most applications $\tilde{f}_\ell$ (not f_ℓ) is the appropriate figure of merit when considering use of fins to enhance heat transfer rates. Figure 1.4b illustrates the tradeoff between (*i*) the increased speed at which PCM can be melted by incorporating fins and (*ii*) the reduction in the amount of PCM that ultimately can be melted; the steady-state value of $\tilde{f}_\ell$ is reduced as the number of fins or their length is increased. In contrast to the results of Fig. 1.4a, it is not possible to draw any general conclusion regarding the speed with which the PCM can be melted as the number of fins, or the fin length, is modified. For example, inspection of Fig. 1.4b reveals that $N = 6$ fins of length $\lambda_f = 0.8$ provide better performance relative to $N = 4$ fins of the same length, if an ultimate value of $\tilde{f}_\ell = 0.6$ is desired. However, if $\tilde{f}_\ell = 0.75$ is targeted, $N = 4$ fins of length $\lambda_f = 0.8$ will outperform six fins.

The effect of fin thickness is shown in Figs. 1.4c and 2.4d ($Ste = 0.04$, $Ra_H = 3.2 \times 10^5$). As expected, increasing the fin thickness modestly increases the PCM melting rate for all cases, if f_ℓ is used as the basis for comparison (Fig. 1.4c). When $\tilde{f}_\ell$ histories are compared (Fig. 1.4d) general conclusions cannot be drawn because of the competing effects previously discussed.

1.3.2. Rapid melting regime

Inspection of Figs. 1.4a – 1.4d suggests that, in general, melting rates are initially rapid, and subsequently decay. In addition, for cases involving fins the transition from rapid to slow melting is relatively sharp, especially for large numbers of fins.

The two melting regimes are further elucidated in Fig. 1.5. Specifically, Fig. 1.5a includes results for $N = 6$ fins with $T_f = T_w = 0.04$, and $Ste = 0.02$, 0.06 and 0.1 ($Ra_H = 1.6 \times 10^5$, 4.8×10^5 and 8.0×10^5). For each fin length, λ_f, the transition from the rapid melting regime to the slow melting regime occurs at a liquid fraction $f_\ell \approx \lambda_f$. This transition point is expected because heat transfer is conduction-dominated at early times. As the number of fins is reduced ($N = 4$ and 2 in Figs. 1.5b and 1.5c, respectively), the melting rate decreases, as expected, but the transition from rapid to slow melting consistently occurs at $f_\ell / \lambda_f \approx 1$.

Rapid melting rates may be estimated as follows. It is assumed that (i) heat transfer is conduction-dominated at early times, (ii) one-dimensional conduction occurs within the molten PCM, (iii) the walls and fins are isothermal at $\theta = 1$, and (iv) Ste is small. In other words, a one-dimensional melt front is assumed to propagate outward from the (artificially straightened) short-dashed line of Fig. 1.1 into the PCM. A linear temperature distribution is assumed in the liquid phase. The resulting analytical expression for the time variation of f_ℓ / λ_f is

$$\frac{f_\ell}{\lambda_f} = C_1 \sqrt{Ste\, Fo_a} \tag{15a}$$

where the length scale in the Fourier number is the inter-fin spacing, a, shown in Fig. 1.1 and C_1 is a constant determined solely from the geometry of the enclosure (using the geometrical variables N, T_f, T_w, λ_f). Specifically,

$$C_1 = \frac{\sqrt{2}}{\lambda_f} \times \frac{(1-2T_w) - NT_f}{N+1} \times \frac{3-4T_w+2N\lambda_f}{1-3T_w+2T_w^2-N\lambda_f T_f} \tag{15b}$$

Representative values of f_ℓ / λ_f obtained from Eq. (15) as well as those generated by the detailed model are shown in Fig. 1.6. (To avoid clutter, predictions of the detailed model are shown as data points.) Regardless of the thermal conditions or fin geometry, agreement between the analytical expression and the detailed predictions is considered to be good. However, in all cases Eq. (15) over-predicts the actual liquid fraction f_ℓ, primarily because of the assumption of instantaneous propagation of the applied boundary temperature through the walls and fins. Nonetheless, for the conditions considered here, Eq. (15) may be used to estimate *maximum possible* melting rates during the rapid melting phase.

Figure 1.7 includes predictions of the modified liquid fraction $\tilde{f}_\ell$ response. The observations noted in conjunction with Fig. 1.5 still apply. However, the transition from rapid to slow melting occurs at $\tilde{f}_\ell < \lambda_f$ because $\tilde{f}_\ell < f_\ell$.

Subject to the same assumptions used to develop Eq. (15), the following expression may be derived

$$\frac{\tilde{f}_\ell}{\lambda_f} = C_2 \sqrt{Ste\, Fo_a} \tag{16a}$$

where C_2 is expressed in terms of the enclosure geometry

$$C_2 = C_1 \left[\frac{1-3T_w+2T_w^2-N\lambda_f T_f}{1-3T_w+2T_w^2} \right] \tag{16b}$$

with C_1 given in Eq. (15b). Predictions based on Eq. (16) are compared to those of the detailed model in Fig. 1.8. (Again, representative results of the full model are shown as data points to avoid clutter). Except for situations involving long fins and $\tilde{f}_\ell / \lambda_f \approx 1$ (Fig. 1.8d and, to a lesser

extent, Fig. 1.8c) Eq. (16) predicts the melting rates quite well. The poor agreement between the analytical expression and the predictions of the detailed model, evident for $N = 6$ fins and $\lambda_f = 0.8$ at $\tilde{f}_\ell / \lambda_f = 1$ (Fig. 1.8d) for example, is traceable to the definition of the modified liquid fraction $\tilde{f}_\ell$. Specifically, the maximum value of $\tilde{f}_\ell$ corresponding to complete melting is $\tilde{f}_{\ell,\, max} = 0.783$ as shown in Fig. 1.7a. Hence, the poor agreement between melting rates predicted by the analytical solution and the full model evolves when melting is nearly complete. From the practical perspective, melting rates just prior to complete melting are seldom of interest, and full melting is usually avoided in LHTES. Hence, throughout the range of practical interest, the predictions of Eq. (16) are considered to be of reasonable accuracy. Furthermore, Eq. (16) has been used to predict independent results reported in the literature. For example, for $N = 19$, $T_w = 0.015$, $T_f = 0.001$, no top or bottom walls, $\lambda_f = 0.15$, $Ste = 0.466$, $Ra_H = 8.08\times10^9$, and $\tilde{f}_\ell / \lambda_f = 1$, Eq. (16) yields $\sqrt{Ste\, Fo_a} = 0.295$ compared to $\sqrt{Ste\, Fo_a} \approx 0.32$ predicted by Lacroix and Benmadda [11]. Again, the agreement between the analytical expression and detailed numerical predictions is considered to be good.

1.3.3. Slow melting regime

A second, slow melting regime is also evident in Figs. 1.5a – 1.5c; the onset of slow melting consistently occurs at $f_\ell / \lambda_f \approx 1$. During slow melting, the fins are not as influential in driving the melting process. Rather, as evident in Fig. 1.3, molten PCM of temperature $\theta \approx 1$ occupies the inter-fin regions and melting to the right of the fin tips proceeds in a manner similar to that of a PCM held within a cavity of size $2(1 - \lambda_f - T_w) \times (1 - 2T_w)\, H^2$ with heated walls.

Slow melting rates may be approximated as follows. Melting is assumed to occur in a hypothetical sub-cavity with neither fins nor walls of height of $H_1 = (1 - 2T_w)H$ and width $(1 - \lambda_f - T_w)\ H$ as defined by the long-dashed volume of Fig. 1.1. No-slip boundary conditions are applied to the left vertical surface of the sub-cavity (coincident with the fin tips) while the left surface temperature (and top and bottom temperatures) is held at $\theta = 1$. The right vertical surface of the sub-cavity is assumed to be solid PCM at the fusion temperature $\theta = 0$. The liquid fraction in the sub-cavity is initially zero. With this approach, existing correlations for natural convection-augmented melting in rectangular enclosures may be applied.

Okada's melting correlation [35] was originally developed to describe the total energy stored in a PCM held in a rectangular enclosure with a uniform temperature left wall and insulated bottom and top walls. Okada assumed the PCM is initially at its fusion temperature and extends to infinity on the right. The Okada correlation was modified to account for the sensible energy stored in the liquid phase and, in turn, predict the liquid fraction history. The resulting expression is

$$\frac{f_\ell}{\lambda_f} = C_3\ Ste\ Fo_H Ra_H^{\frac{1}{4}} \tag{17a}$$

where C_3 is related to the enclosure geometry and Stefan number as

$$C_3 = \frac{1}{\lambda_f}\ \frac{0.99}{1+\frac{Ste}{2}}\ \frac{\left(1-2T_w\right)^{\frac{3}{4}}}{1-3T_w+2T_w{}^2-N\lambda_f T_f} \tag{17b}$$

Figures 1.9a-1.9d show representative dimensionless absolute liquid fraction histories, as predicted by Eq. (17) and as obtained from the detailed model (again, shown as data points).

Note that Eq. (17) is applied with f_ℓ / λ_f initially equal to unity, and the length scale in the Fourier and Rayleigh numbers is H. As evident, the influence of the number of fins on the melting rate is small. Eq. (17) also exhibits little sensitivity to the Stefan number or Rayleigh number for the conditions of this study. Of course the melting rate predicted by Eq. (17) in the sub-cavity of Fig. 1.1 is independent of the fin length. However, since the liquid fraction associated with $f_\ell / \lambda_f = 1$ is greater for longer fins, the additional melting in the slow melting regime has less influence on increasing f_ℓ / λ_f for the cases involving longer fins. Finally, only results are reported that correspond to solid PCM at $X = 1$ and $0 < Y < 1$ to be consistent with the Okada correlation developed for a semi-infinite PCM. Overall, the agreement between Eq. (17) and the predictions of the detailed model is considered to be good.

An expression for the modified liquid fraction may be derived using the same assumptions used to develop Eq. (17). The resulting expressions are

$$\frac{\tilde{f}_\ell}{\lambda_f} = C_4 \; Ste \, Fo_H Ra_H^{\frac{1}{4}} \tag{18a}$$

where C_4 is expressed in terms of the enclosure geometry

$$C_4 = C_3 \left[\frac{1 - 3T_w + 2T_w^{\,2} - N\lambda_f T_f}{1 - 3T_w + 2T_w^{\,2}} \right] \tag{18b}$$

The predictions of Eq. (18) are compared to those of the detailed model in Fig 1.10. Again, the agreement between the analytical expression and the predictions of the detailed model are considered to be good, except for the late stages of melting in cases involving relatively long fins, as evident in Figs. 1.10c and 10d. The poor agreement at the final stages of melting for long

fins is expected, based upon the discussion of Fig. 1.8, and melting at these times is seldom of practical interest.

1.4. Conclusions

A numerical model has been developed that shows, quantitatively, the effect of adding internal horizontal rectangular fins to enhance the melting of a PCM within an enclosure. The model accounts for conduction heat transfer in the enclosure walls and fins, as well as natural convection in the liquid phase of the PCM. Of primary interest is the rate at which the liquid fraction of the PCM evolves. Both absolute liquid fractions (based upon the initial amount of PCM in a particular enclosure) and modified liquid fractions (based upon the initial amount of PCM in an enclosure with no fins) are reported.

For the range of conditions and the PCM considered here, utilization of horizontal rectangular fins initially promotes rapid melting, followed by slower melting once the PCM in the inter-fin regions has been liquefied. The transition between the slow and rapid melting regimes is relatively sharp, and is related to the dimensionless fin length.

Analytical expressions have been derived that can be used to predict melting rates for both the rapid (fin dominated) and slow (natural convection dominated) melting regimes to within an acceptable degree of accuracy. Specifically, four new correlations are presented for the entire melting duration that can be used to predict either the absolute liquid fraction or the modified liquid fraction of the PCM.

The numerical methodology and the concept of deriving analytical expressions and correlations for both rapid and slow melting may be applicable to any horizontal-finned configuration melting scenario involving an opaque PCM undergoing laminar free convection in

the molten phase. Additional investigation is needed to determine the extent to which the new analytical expressions may be applied to other enclosure geometries, turbulent flow conditions, or PCMs characterized by, for example, low Prandtl numbers.

Nomenclature

a	inter-fin spacing (m)
c	specific heat ($kJ/kg{\cdot}K$)
C	dimensionless heat capacity
C_1, C_2, C_3, C_4	constants
f_ℓ	absolute liquid fraction
$\tilde{f}_\ell$	modified liquid fraction
Fo	Fourier number
g	gravitational acceleration (m/s^2)
h	enthalpy (kJ/kg)
$h_{s\ell}$	latent heat of fusion (kJ/kg)
H	cavity dimension (m)
k	thermal conductivity ($W/m{\cdot}K$)
K	dimensionless thermal conductivity
L	length (m)
N	number of fins
p	pressure (Pa)
P	dimensionless pressure
Pr	Prandtl number
q^o	dimensionless heat rate
R_{th}	dimensionless thermal resistance
Ra	Rayleigh number
Ste	Stefan number
t	time (s); thickness (m)
T^*	scaled temperature (K)
T	dimensionless thickness, temperature (K)
T_m	melting temperature (K)
u, v	velocity components (m/s)
U, V	dimensionless velocity components

x, y coordinates (m)

X, Y dimensionless coordinates

Greek

α thermal diffusivity (m^2/s)

β thermal expansion coefficient (K^{-1})

δT small temperature difference (K)

$\delta\theta$ dimensionless δT

θ dimensionless temperature

λ dimensionless fin length

μ viscosity ($P \cdot s$)

ν kinematic viscosity (m^2/s)

ρ density (kg/m^3)

τ dimensionless time

Subscripts

f fin

h hot wall

ℓ liquid phase

s solid phase

w wall

Table 1.1. Thermophysical properties of octadecane and copper

Properties	Octadecane [30]	Copper [36]
Melting point, T_m (K)	303	-
Latent heat of fusion, $h_{s\ell}$ (kJ/kg)	125	-
Density, ρ (kg/m^3)	800	8933
Specific heat, c $(kJ/kg{\cdot}K)$	1.25	0.385
Thermal conductivity, k $(W/m{\cdot}K)$	0.2	401
Liquid viscosity, μ $(Pa\ s)$	8×10^{-3}	-
Thermal expansion coefficient, β (K^{-1})	2×10^{-3}	-
Thermal diffusivity, α (m^2/s)	2×10^{-7}	-
Kinematic viscosity, v (m^2/s)	10^{-5}	-
Prandtl number, Pr	50	-

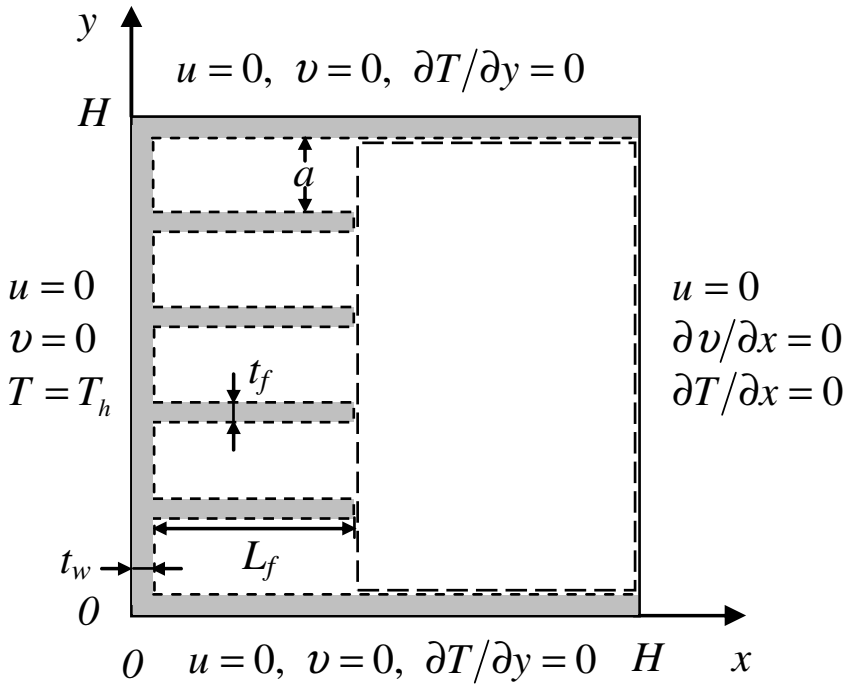

Fig. 1.1. Schematic of the LHTES system. The short-dashed line and rectangular control volume are pertinent to the development of analytical expressions for the melting rate.

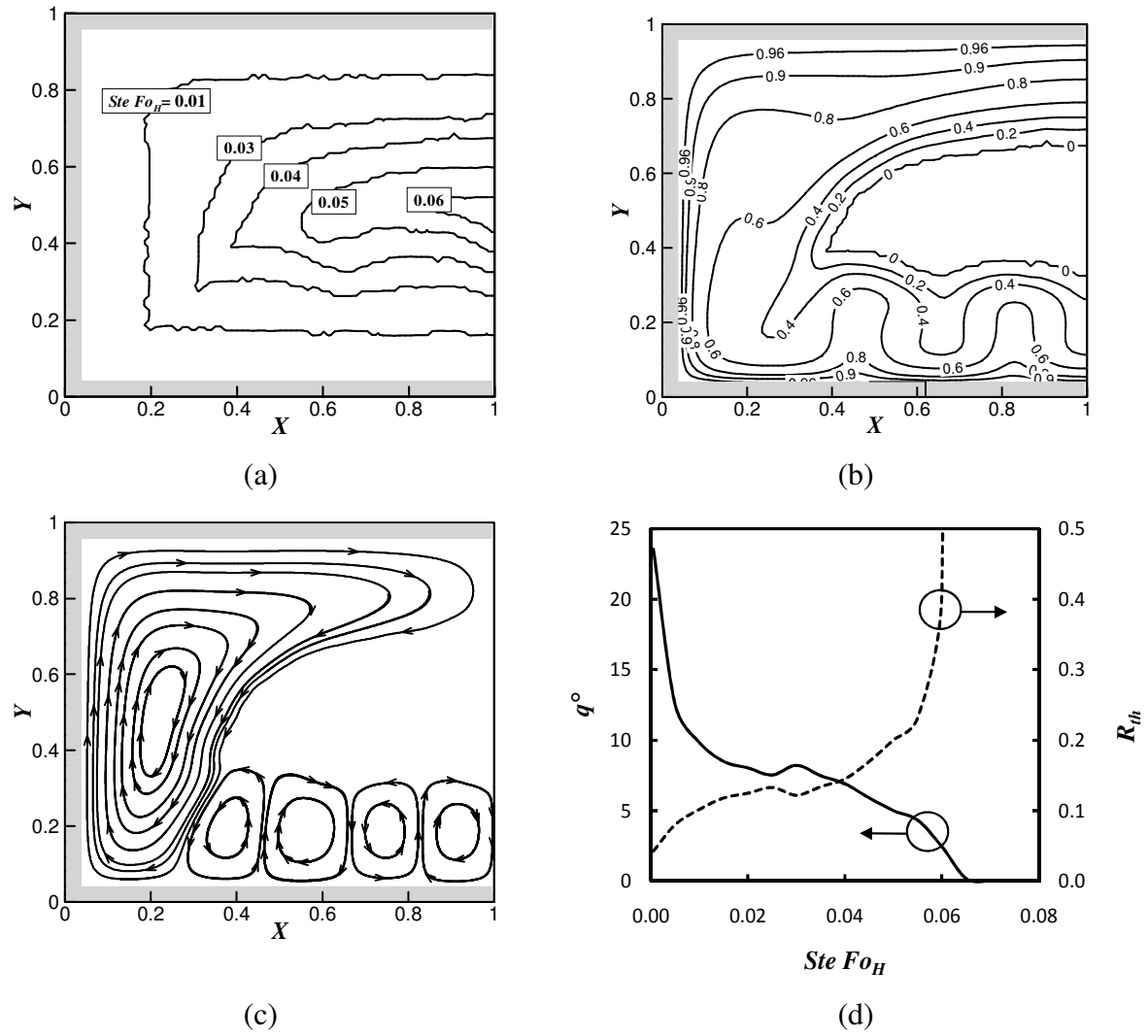

Fig. 1.2. System response with no fins (T_w = 0.04, λ_f = 0, Ste_H = 0.04, $Ra_H = 3.2 \times 10^5$) (a) solid-liquid interface locations, (b) isotherms at $SteFo_H$ = 0.04, (c) streamlines at $SteFo_H$ = 0.04, (d) dimensionless heat rate and thermal resistance histories.

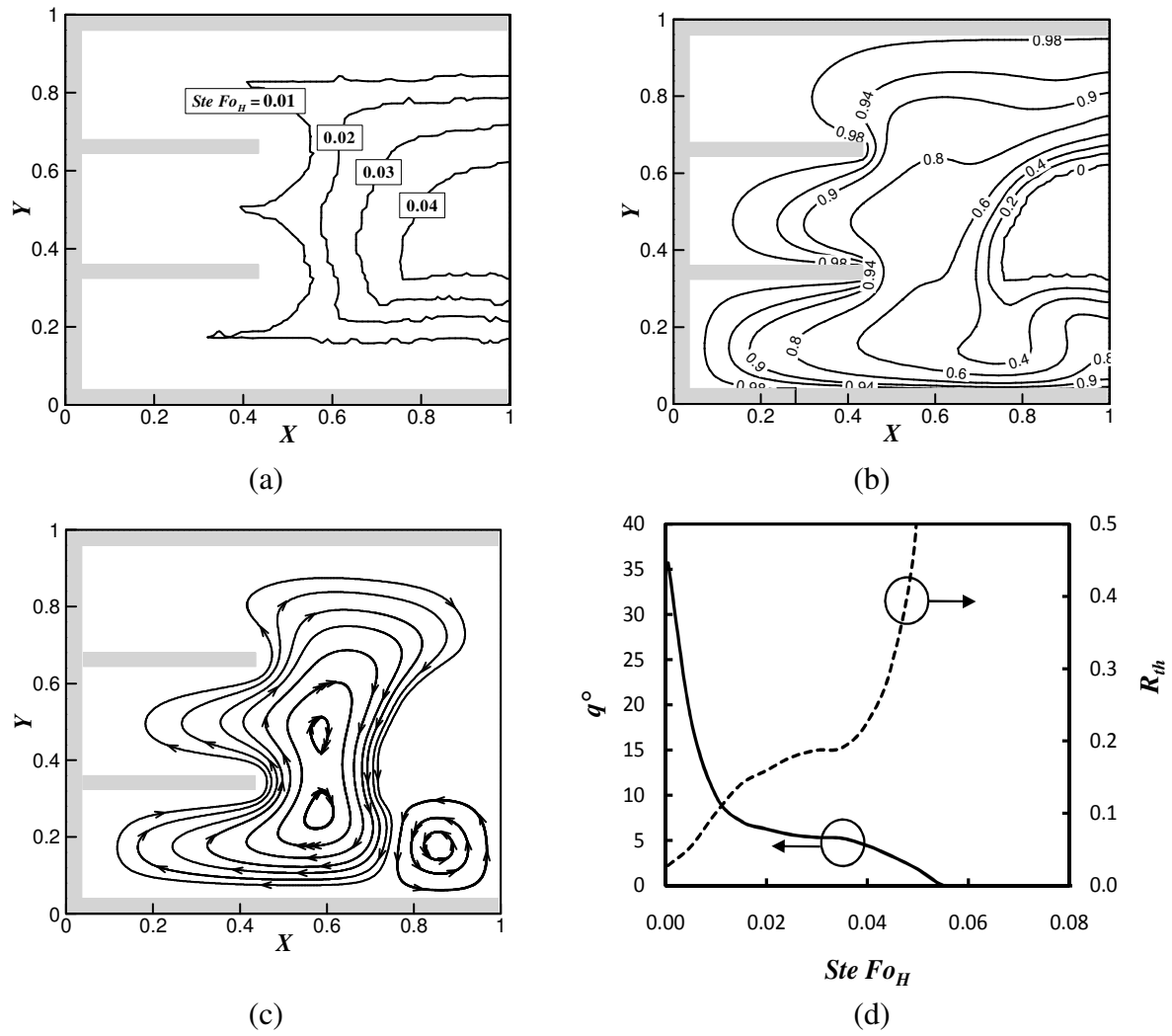

Fig. 1.3. System response with two fins (T_w = 0.04, λ_f = 0.4, T_f = 0.04, Ste = 0.04, Ra_H = 3.2 × 10^5) (a) solid-liquid interface locations, (b) isotherms at $SteFo_H$ = 0.04, (c) streamlines at $SteFo_H$ = 0.04, (d) dimensionless heat flux and thermal resistance histories.

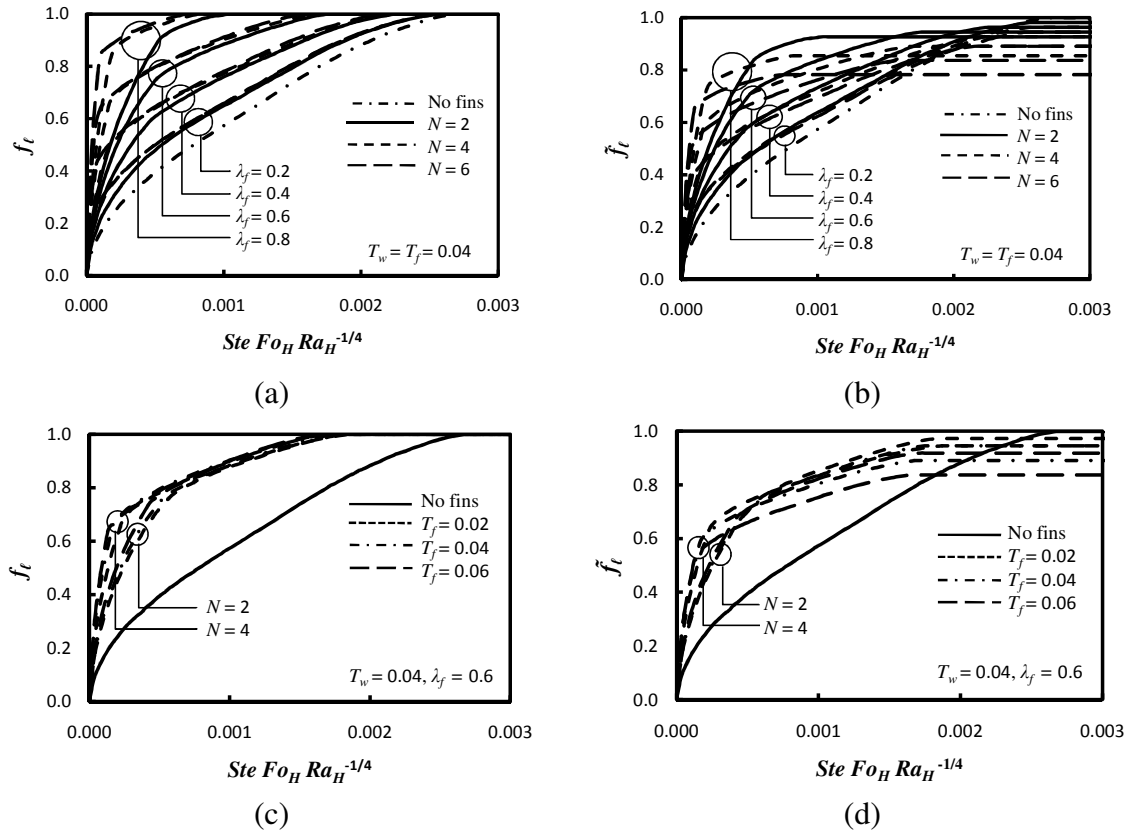

Fig. 1.4. Liquid fraction history (Ste = 0.04, Ra_H = 3.2 × 10^5), (a) f_ℓ for different N, (b) $\tilde{f}_\ell$ for different N, (c) f_ℓ for different T_f, (d) $\tilde{f}_\ell$ for different T_f.

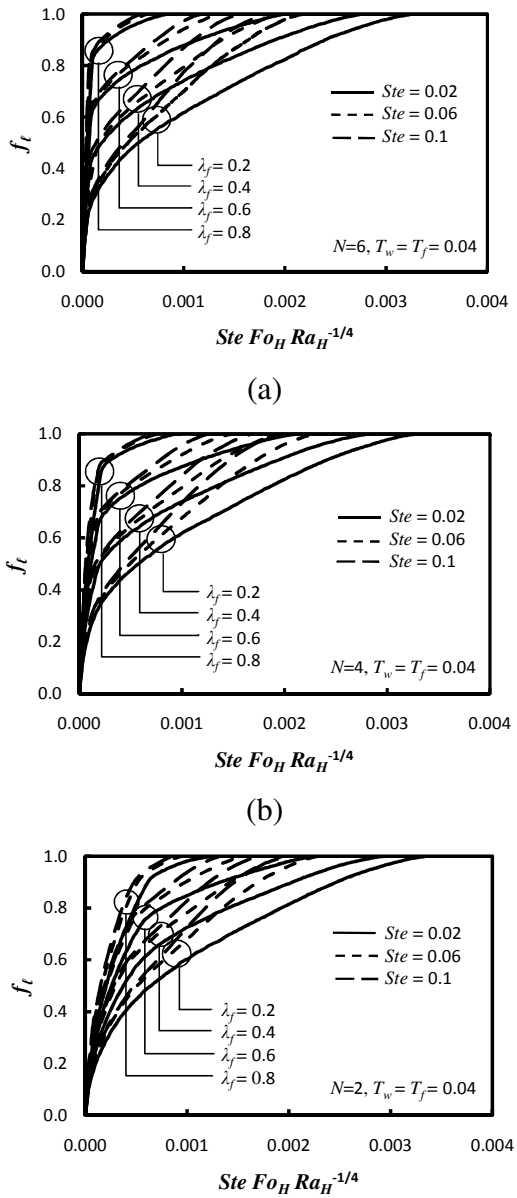

Fig. 1.5. Absolute liquid fraction history, (a) $N = 6$, (b) $N = 4$, (c) $N = 2$. Rayleigh numbers are $Ra_H = 1.6 \times 10^5$, 4.8×10^5 and 8.0×10^5 for $Ste = 0.02$, 0.06 and 0.1, respectively.

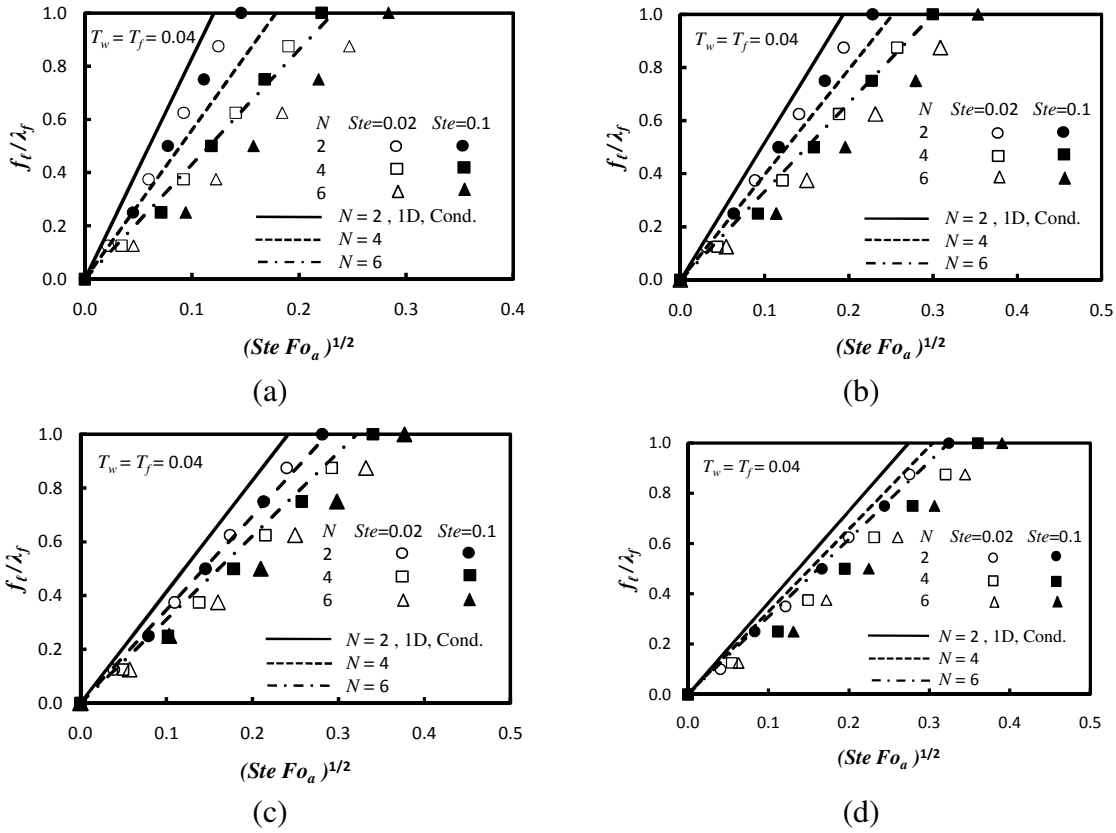

Fig. 1.6. Absolute liquid fraction histories for the rapid melting regime, (a) $\lambda_f = 0.2$, (b) $\lambda_f = 0.4$, (c) $\lambda_f = 0.6$, (d) $\lambda_f = 0.8$. Rayleigh numbers are $Ra_H = 1.6 \times 10^5$ and 8.0×10^5 for $Ste = 0.02$ and 0.1, respectively.

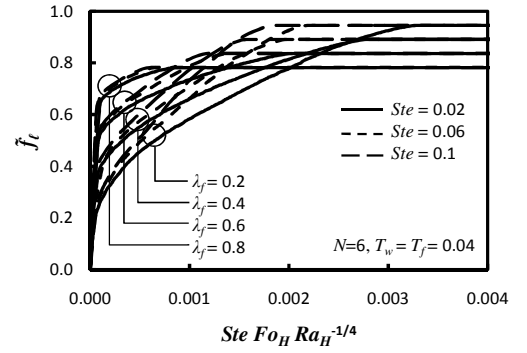

(a)

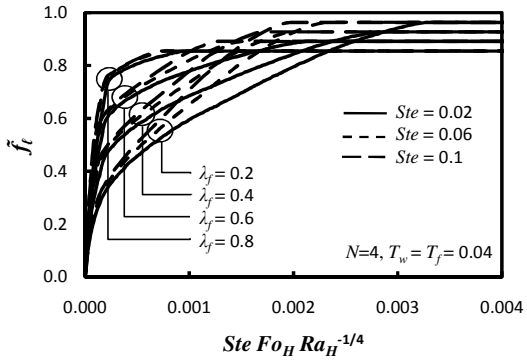

(b)

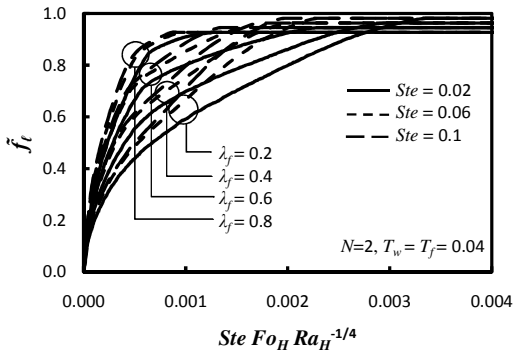

(c)

Fig. 1.7. Modified liquid fraction history, (a) N = 6, (b) N = 4, (c) N = 2. Rayleigh numbers are $Ra_H = 1.6 \times 10^5$, 4.8×10^5 and 8.0×10^5 for Ste = 0.02, 0.06 and 0.1, respectively.

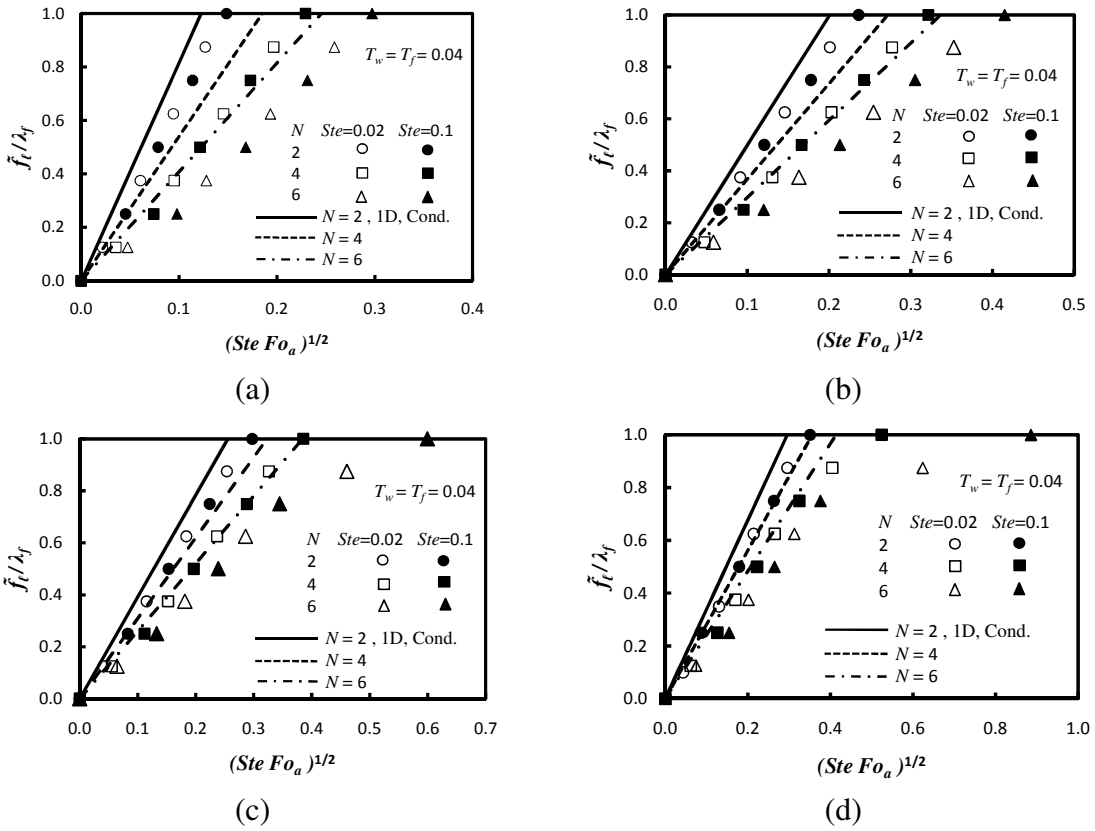

Fig. 1.8. Modified liquid fraction history for rapid melting regime, (a) $\lambda_f = 0.2$, (b) $\lambda_f = 0.4$, (c) $\lambda_f = 0.6$, (d) $\lambda_f = 0.8$. Rayleigh numbers are $Ra_H = 1.6 \times 10^5$ and 8.0×10^5 for $Ste = 0.02$ and 0.1, respectively.

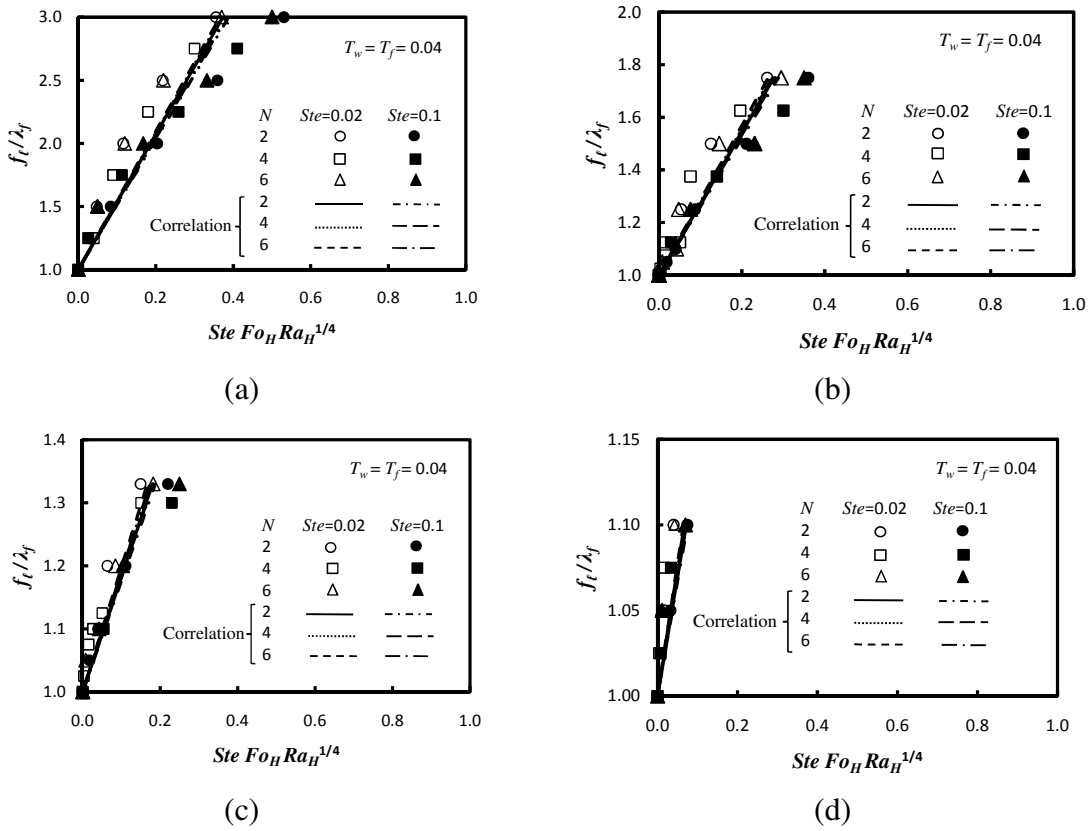

Fig. 1.9. Absolute liquid fraction history for the slow melting regime, (a) λ_f=0.2, (b) λ_f=0.4, (c) λ_f=0.6, (d) λ_f=0.8. Rayleigh numbers are $Ra_H = 1.6 \times 10^5$ and 8.0×10^5 for Ste = 0.02 and 0.1, respectively.

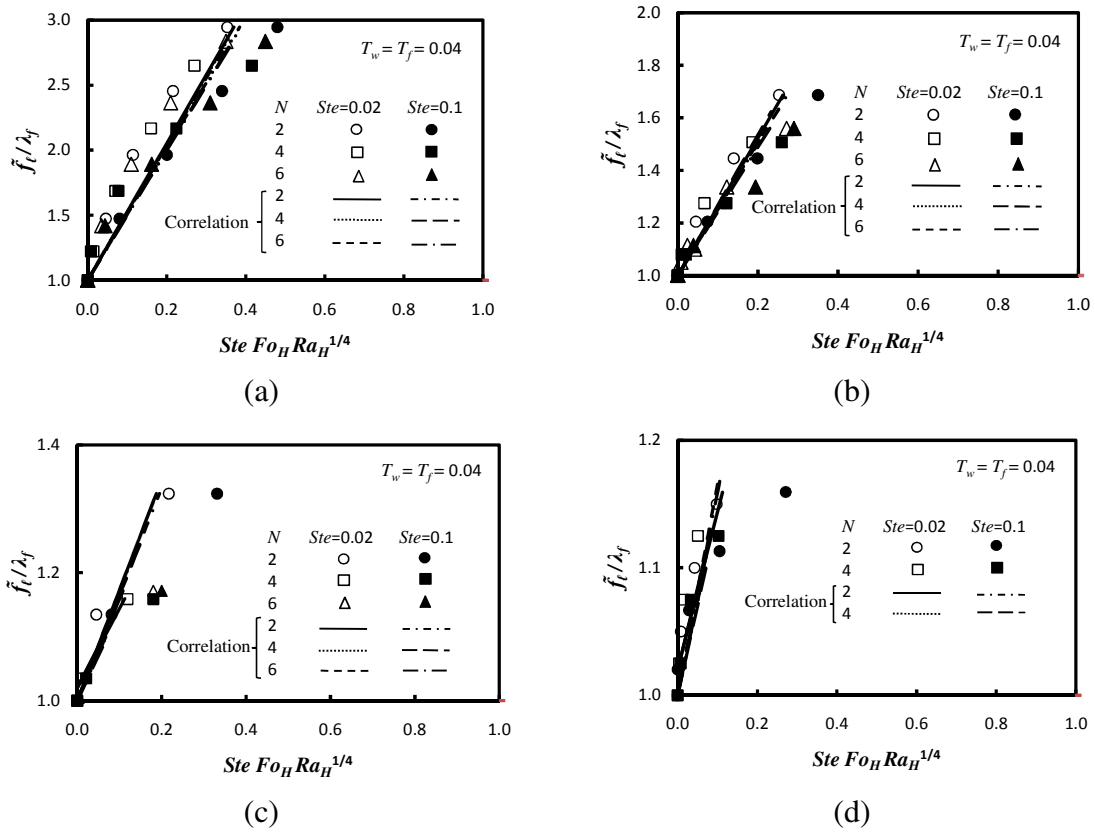

Fig. 1.10. Modified liquid fraction history for slow melting regime, (a) $\lambda_f = 0.2$, (b) $\lambda_f = 0.4$, (c) $\lambda_f = 0.6$, (d) $\lambda_f = 0.8$. Rayleigh numbers are $Ra_H = 1.6 \times 10^5$ and 8.0×10^5 for $Ste = 0.02$ and 0.1, respectively.

References

[1] B. Zalba, J.M. Marin, L.F. Cabeza, H. Mehling, Review on thermal energy storage with phase change: materials, heat transfer analysis and applications, Applied Thermal Engineering 23 (3) (2003) 251-283.

[2] M.M. Farid, A.M. Khudhair, S.A.K. Razack, S. Al-Hallaj, A review on phase change energy storage: materials and applications, Energy Conversion and Management 45 (9 - 10) (2004) 1597-1615.

[3] S.D. Sharma, K. Sagara, Latent heat storage materials and systems: a review, International Journal of Green Energy 2 (1) (2005) 1-56.

[4] F. Agyenim, N. Hewitt, P. Eames, M. Smyth, A review of materials, heat transfer and phase change problem formulation for latent heat thermal energy storage systems (LHTESS), Renewable & Sustainable Energy Reviews 14 (2) (2010) 615-628.

[5] O. Mesalhy, K. Lafdi, A. Elgafy, K. Bowman, Numerical study for enhancing the thermal conductivity of phase change material (PCM) storage using high thermal conductivity porous matrix, Energy Conversion and Management 46 (6) (2005) 847-867.

[6] J. M. Martin, B. Zalba, L. F. Cabeza, H. Mehling, Improvement of a thermal energy storage using plates with paraffin-graphite composite, International Journal of Heat and Mass Transfer 48 (12) (2005) 2561-2570.

[7] S. Jegadheeswaran, S. D. Pohekar, Energy and exergy analysis of particle dispersed latent heat storage system, International Journal of Energy and Environment 1 (3) (2010) 445-458.

[8] A. Sari, C. Alkan, A. Karaipekli, O. Uzun, Microencapsulated n-octacosane as phase change material for thermal energy storage, Solar Energy 83 (10) (2009) 1757–1763.

[9] C. W. Robak, T. L. Bergman, A. Faghri, Enhancement of latent heat energy storage using embedded heat pipes, International Journal of Heat and Mass Transfer 54 (15-16) (2011) 3476-3484, DOI 10.1016/j.ijheatmasstransfer.2011.03.038.

[10] H. Shabgard, T.L. Bergman, N. Sharifi, A. Faghri, High temperature latent heat thermal energy storage using heat pipes, International Journal of Heat and Mass Transfer 53 (15-16) (2010) 2979-2988.

[11] M. Lacroix, M. Benmadda, Numerical simulation of natural convection-dominated melting and solidification from a finned vertical wall, Numerical Heat Transfer Part A-Applications 31 (1) (1997) 71-86.

[12] M. Lacroix, M. Benmadda, Analysis of natural convection melting from a heated wall with vertically oriented fins, International Journal of Numerical Methods for Heat & Fluid Flow 8 (4) (1998) 465-478.

[13] M.J. Huang, P.C. Eames, B. Norton, Thermal regulation of building-integrated photovoltaics using phase change materials, International Journal of Heat and Mass Transfer 47 (12-13) (2004) 2715–2733.

[14] V. Shatikian, G. Ziskind, R. Letan, Numerical investigation of a PCM-based heat sink with internal fins, International Journal of Heat and Mass Transfer 48 (17) (2005) 3689–3706.

[15] R. Akhilesh, A. Narasimhan, C. Balaji, Method to improve geometry for heat transfer enhancement in PCM composite heat sinks, International Journal of Heat and Mass Transfer 48 (13) (2005) 2759–2770.

[16] M. Gharebaghi, I. Sezai, Enhancement of heat transfer in latent heat storage modules with internal fins, Numerical Heat Transfer Part A-Applications 53 (7) (2008) 749–765.

[17] O. Bertrand, B. Binet, H. Combeau, S. Couturier, Y. Delannoy, D. Gobin, M. Lacroix, P. Le Quere, M. Medale, J. Mencinger, H. Sadat, G. Vieria, Melting driven by natural convection – a comparison exercise: first results, International Journal of Thermal Science 38 (1) (1999) 5–26.

[18] Y.-J. Jan, T. W.-H. Sheu, Z.-Y. Hsu, F.-P. Lin, On a mushy cell tracking method for simulating gallium melting, Numerical Heat Transfer Part B-Fundamentals 51 (2007) 351-374.

[19] V. Kumar, F. Durst, and S. Ray, Modeling moving-boundary problems of solidification and melting adopting an arbitrary Lagrangian-Eulerian approach, Numerical Heat Transfer Part B-Fundamentals 49 (4) (2006) 299-331.

[20] N. Hannoun, V. Alexiades, and T.Z. Mai, Resolving the controversy over tin and gallium melting in a rectangular cavity heated from the side, Numerical Heat Transfer Part B-Fundamentals, 44 (3) (2003) 253-276.

[21] I. Wintruff, C. Gunther, and A. G. Class, An interface-tracking control-volume finite-element method for melting and solidification problems - Part I: formulation, Numerical Heat Transfer Part B-Fundamentals, 39 (2) (2001) 101-125.

[22] I. Wintruff, C. Gunther, and A. G. Class, An interface-tracking control-volume finite-element method for melting and solidification problems - Part II: verification and application, Numerical Heat Transfer Part B-Fundamentals 39 (2) (2001) 127-149.

[23] A. Faghri, Y. Zhang, J. Howell, Advanced Heat and Mass Transfer, Global Digital Press, Columbia, 2010.

[24] A. Faghri, Y. Zhang, Transport Phenomena in Multiphase System, Academic Press, Elsevier, New York, 2006.

[25] Y. Cao, A. Faghri, A numerical analysis of phase change problems including natural convection, Journal of Heat Transfer 112 (1990) 812-816.

[26] Y. Cao, A. Faghri, Performance characteristics of a thermal energy storage module: a transient PCM/forced convection conjugate analysis, International Journal of Heat and Mass Transfer 34 (1) (1991) 93-101.

[27] X. Zeng, A. Faghri, A temperature transforming model for binary solid-liquid phase change problems: Part I-mathematical modeling and numerical methodology, Numerical Heat Transfer Part B-Fundamentals, 25 (1994) 467-480.

[28] X. Zeng, A. Faghri, A temperature transforming model for binary solid-liquid phase change problems: Part II-numerical simulation, Numerical Heat Transfer Part B-Fundamentals, 25 (1994) 481-500.

[29] Z. Ma, Y. Zhang, Solid velocity correction schemes for a temperature transforming model for convection phase change, International Journal of Numerical Methods for Heat & Fluid Flow 16 (2) (2006) 204–225.

[30] S.M. Wang, A. Faghri, T. L. Bergman, A comprehensive numerical model for melting with natural convection, International Journal of Heat and Mass Transfer 53 (9-10) (2010) 1986-2000.

[31] S.V. Patankar, Numerical Heat Transfer and Fluid Flow, McGraw-Hill, New York, 1980.

[32] J. H. Ferziger, M. Peric, Computational Methods for Fluid Dynamics, Springer, New York, 1996.

[33] H. L. Stone, Iterative solution of implicit approximations of multidimensional partial differential equations, SIAM Journal on Numerical Analysis 5 (3) (1968) 530-558.

[34] R. H. Henze, J. A. C. Humphrey, Enhanced heat conduction in phase-change thermal energy storage devices, International Journal of Heat and Mass Transfer 24 (1980) 459-474.

[35] M. Okada, Melting from a vertical plate between insulated top and bottom surfaces, in: Y. Mori and W. Yang (Eds.), Proceedings of the Third ASME-JSME Thermal Engineering Joint Conference, Honolulu, HI, 1983, pp. 281-288.

[36] T.L. Bergman, A.S. Lavine, F.P. Incropera, D.P. DeWitt, Fundamentals of Heat and Mass Transfer, 7th ed., Wiley, Hoboken, 2011, p. 983.

Chapter 2. Three-Dimensional PCM Melting in a Vertical Cylindrical Enclosure Including the Effects of Tilting

Experiments have been conducted in order to generate detailed data associated with the outward melting of a PCM induced by a heated rod that is placed concentrically within a cylindrical enclosure. Heat transfer and melting effects in a base-case configuration consisting of a vertically-oriented enclosure are successfully simulated with an established two-dimensional numerical model, partially validating the experimental apparatus and procedure. Experimental measurements indicate that modest tilting of the test cell significantly affects measured local temperatures within the PCM, as well as the temporal evolution of the solid morphology as it melts. The modification is attributed to the establishment of three-dimensional flow within the molten PCM. The experimental data for the tilted enclosure cases might be used to validate three-dimensional models for PCM melting in geometrical configurations relevant to, for example, latent heat thermal energy storage systems.

2.1. Introduction

Heat transfer during melting and solidification has been investigated extensively over the past several decades due to its importance in various applications [1, 2]. As is well-known, free convection can become established in the liquid phase, affecting local heat transfer and phase change rates, particularly during melting. Despite the interest in heat transfer during solid-liquid phase change, few numerical predictions of 3D melting (or solidification) have been reported. Moreover, detailed experimental measurements corresponding to 3D melting and solidification are sparse. Most lacking are experimental data that could be used for model validation in

cylindrical enclosures experiencing 3D effects, a situation of interest in thermal energy storage systems involving, for example, cylindrical heat pipes or thermosyphons [3-5].

An early numerical investigation of 3D solid-liquid phase change was conducted by Costa et al. [6] who considered melting of a pure phase change material (PCM) within an isothermal, horizontal cylindrical enclosure. Robust 3D convection develops in this configuration, especially in the gap between the solid PCM and the underlying warm cylinder wall. The predicted 3D topography of the solid PCM (and melting rates) were compared qualitatively (quantitatively) to experimental measurements [7-9].

Prediction of 3D melting of a metal housed within a rectangular enclosure with a single isothermal warm wall was achieved by Kumar et al. [10] who showed that the insulated enclosure end walls induce 3D flow in the melt. More recently, Wittig and Nikrityuk [11] have presented predictions similar to those of [10], with good agreement with the experimental measurements of the solid-liquid interface locations measured by Gau and Viskanta [12], as well as with the predictions of [10].

Predictions of 3D melting within enclosures of more complex geometry have been reported recently by Wang and Yang [13] as well as Yang and Wang [14]. Specifically, the enclosures consisted of compartmentalized layers of PCM [13] and included the effect of tilting [14]. Experimental verification of the model was sought by comparing predicted temperatures at various wall locations to temperatures measured by Fok et al. [15]. No comparison was made between the predicted and actual solid PCM topographies or solid-liquid interface locations. Similarly, Huang et al. [16] as well as Fan et al. [17] have generated predictions of 3D melting in a rectangular enclosure and reported only fair comparison between predicted and measured local temperatures and overall heat transfer rates.

Recent 3D simulations of the freezing of water including the effects of free convection in the liquid phase have been reported by Belhamadia et al. [18] and were validated by comparing the model predictions to the measured solid-liquid interface locations of Kowalewski and Rebow [19]. Predictions involving the 3D solidification of aluminum [20] have been reported with a comparison to temperatures measured in an industrial setting. Simulations of 3D melting phenomena, without any comparison of predictions to experimental measurements, have been reported by Huang et al. [21] as well as Nithyanandam and Pitchumani [22].

Although benchmark experimental data for 2D inward melting in a vertical cylindrical enclosure have been recently reported [23], there appear to be no other experimental data corresponding to the cylindrical geometry other than for the 3D inward melting associated with the horizontal heated cylindrical [7-9]. Moreover, to the authors' knowledge, there are no data available for outward melting as would occur from a vertical warm cylindrical heat pipe or thermosyphon embedded in the solid PCM, a geometry of significance in thermal energy storage applications [3-5, 22]. As such, the objectives of this study are to (i) generate and report experimental data in the form of detailed PCM temperature measurements for outward melting in a cylindrical geometry, and (ii) document the solid shape evolution during the 3D melting process. Of interest are situations where three-dimensionality of the free convection flow and associated local melting rates is induced by tilting the nominally-vertical enclosure.

2.2. Experimental Design

A schematic of the test cell is shown in Fig. 2.1a and pertinent dimensions are provided in Fig. 2.1b. The PCM is housed in a vertically-orientated enclosure with an inside diameter and height of 45.8 mm and 18.9 mm, respectively. The enclosure is formed by a cylindrical acrylic

tube of wall thickness 4.6 mm, and two 6.4 mm thick top and bottom Teflon plates. The joints between the plates and the cylinder are sealed with compressed synthetic rubber O-rings, and a 10 mm diameter pure copper rod of length 82 mm is secured concentrically in the bottom plate with a brass Swagelok fitting. The bottommost portion of the rod is wrapped in a 38.2 mm long electric resistance heater (Minco 9449) which is powered with a Protek dual DC power supply. The entire test cell is wrapped with a 20 mm thick fiber glass blanket. To provide additional insulation, a second 127 mm ID acrylic cylinder is installed over the test cell, creating a 11.5 mm air gap. The entire apparatus is placed on a metallic plate that can be tilted to angles $0^\circ \leq \theta \leq 20^\circ$ from the vertical. The test cell can also be rotated about an azimuthal angle ϕ. The uncertainty in the tilt and azimuthal angles is ± 1 degree. A paraffin wax, n-octadecane (99% pure $C_{18}H_{38}$, $T_m \approx 28$ºC) is used as the PCM. Relevant properties are listed in Table 2.1.

Temperature data are obtained from 8 Teflon-coated, 254 μm diameter chromel-alumel (K-type) thermocouples that are held in place with a yoke constructed of an acrylic tube within the PCM. The thermocouple beads are all located in a single ϕ plane, and their r and z coordinates, accurate to within ±1mm, are listed in Table 2.2. Prior to installation the thermocouples were calibrated at both the freezing and boiling points of water, and the estimated error in measured temperatures is ± 0.1°C. Thermocouple voltages are collected using a National Instruments data acquisition system, and Labview software is used to process the voltages and record temperatures. Photographs of the PCM are taken using a 10-megapixel Nikon digital camera.

2.3. Experimental Procedure

The experiments begin with solid, nearly isothermal PCM that is made free of voids to the extent possible. Prior to each experiment the PCM was conditioned by melting and heating it under vacuum to remove dissolved gases. Subsequently, the degassed PCM was added to the enclosure in a layer-by-layer manner. Specifically, the liquid PCM was injected through small holes in the top Teflon plate using a syringe, creating an approximately 2 mm thick initial PCM layer. The test cell was then refrigerated to solidify the PCM, after which the injection and freezing process was repeated until the enclosure is filled with solid PCM. The test cell and its contents were allowed to equilibrate to room temperature (≈ 25°C) for approximately 12 h, after which the test cell was secured to the tilting table and insulated. The heater is energized to deliver the specified power at the outset of each experiment. Experimental repeatability was checked by performing all experiments twice.

Several experiments were performed without the embedded thermocouples to facilitate photographing the time evolution of the PCM melting process. Specifically, without the thermocouples in place the liquid PCM could be drained from the test cell at predetermined times allowing the solid PCM to be removed, sectioned, and photographed.

2.4. Numerical Model

To validate the experimental setup and process, a preliminary step was to compare experimental measurements associated with the $\theta = \phi = 0^{o}$ configuration (2D flow and heat transfer) to the predictions of an established, 2D melting model. Moreover, to focus on the effects of tilting and to eliminate the possible influence of turbulent conditions in the molten PCM, the dimensions of the test cell are relatively small. As a result, conjugate effects involving

conduction in the test cell components are significant, and these effects are included in the model. The computational domain therefore consists of the PCM, the copper rod, the acrylic and Teflon walls (including the Swagelok fitting), and the fiber glass insulation. The appropriate forms of the two-dimensional mass, momentum, and energy equations were solved using a finite volume, temperature transforming model [24-29] based upon the following assumptions: all properties are constant, the PCM is a pure and homogeneous substance, the densities of the solid and liquid PCM are equal, the liquid PCM is a Boussinesq Newtonian fluid, the free convection is incompressible and laminar with no viscous dissipation effects, all materials are opaque to thermal radiation, and thermal contact resistances are negligible.

2.4.1. Governing equations

2.4.1.1. Phase change material

Based upon the preceding assumptions, the two-dimensional thermal response of the PCM is governed by the following conservation equations [24, 25].

Continuity:

$$\frac{1}{r}\frac{\partial(\rho r u)}{\partial r}+\frac{\partial(\rho v)}{\partial z}=0 \tag{1}$$

Momentum:

$$\frac{\partial(\rho u)}{\partial t}+\frac{1}{r}\frac{\partial(\rho r u^2)}{\partial r}+\frac{\partial(u v)}{\partial z}=-\frac{\partial p}{\partial r}+\frac{1}{r}\frac{\partial}{\partial r}\left(\mu r\frac{\partial u}{\partial r}\right)+\frac{\partial}{\partial z}\left(\mu\frac{\partial u}{\partial z}\right)-\mu\frac{u}{r^2} \tag{2}$$

$$\frac{\partial(\rho v)}{\partial t}+\frac{1}{r}\frac{\partial(\rho r u v)}{\partial r}+\frac{\partial(v^2)}{\partial z}=-\frac{\partial p}{\partial z}+\frac{\partial}{\partial r}\left(\mu r\frac{\partial v}{\partial r}\right)+\frac{\partial}{\partial z}\left(\mu\frac{\partial v}{\partial z}\right)+\rho g\beta(T-T_m) \tag{3}$$

Energy:

$$\frac{\partial(\rho h)}{\partial t}+\frac{1}{r}\frac{\partial(\rho ruh)}{\partial r}+\frac{\partial(\rho vh)}{\partial z}=\frac{1}{r}\frac{\partial}{\partial r}\left(kr\frac{\partial T}{\partial r}\right)+\frac{\partial}{\partial z}\left(k\frac{\partial T}{\partial z}\right) \tag{4}$$

Note that the velocities are zero in the solid phase. Defining a scaled temperature as $T^* = T - T_m$, and expressing the enthalpy through application of the temperature transforming model [24-29],

$$h = c(T^* + s) \tag{5}$$

where for an arbitrary small temperature difference δT,

$$c=\begin{cases} c_s & T^* < -\delta T \\ \dfrac{c_s + c_\ell}{2}+\dfrac{h_{s\ell}}{2\delta T} & -\delta T \le T^* \le \delta T \\ c_\ell & T^* > \delta T \end{cases} \tag{6}$$

and

$$s=\begin{cases} \delta T & T^* < -\delta T \\ \delta T & -\delta T \le T^* \le \delta T \\ \dfrac{c_s}{c_\ell}\delta T+\dfrac{h_{s\ell}}{c_\ell} & T^* > \delta T \end{cases} \tag{7}$$

With the temperature transforming model, the energy equation can be written as

$$\frac{\partial(\rho cT^*)}{\partial t}+\frac{1}{r}\frac{\partial(\rho rucT^*)}{\partial r}+\frac{\partial(\rho \upsilon cT^*)}{\partial z}=\frac{1}{r}\frac{\partial}{\partial r}\left(kr\frac{\partial T^*}{\partial r}\right)+\frac{\partial}{\partial z}\left(k\frac{\partial T^*}{\partial z}\right)-\left[\frac{\partial(\rho s)}{\partial t}+\frac{1}{r}\frac{\partial(\rho rus)}{\partial r}+\frac{\partial(\rho \upsilon s)}{\partial z}\right] \quad (8)$$

where the properties are evaluated separately for each phase of the PCM,

$$k=\begin{cases} k_s & T^* < -\delta T \\ k_s+(k_\ell-k_s)\dfrac{(T^*+\delta T)}{2\delta T} & -\delta T \le T^* \le \delta T \\ k_\ell & T^* > \delta T \end{cases} \quad (9)$$

2.4.1.2. Other solid materials

Equation (8) can also be applied to all other materials within the computational domain by specifying the appropriate properties and setting $s = u = \upsilon = 0$. When applied to the heater, a source term $\dot{q}_h = P_h/V$ is added to the RHS of Eqs. (4) and (8). The Swagelok fitting is modeled as a cylindrical geometry. No-slip and adiabatic boundary conditions are applied to the right, bottom and top of the computational domain of Fig. 2.1b. Symmetry conditions are applied at $r = 0$. To be consistent with experimental conditions, the initial temperature of the entire domain is assumed to be $T_i = 25$ºC. The thin heating foil is assumed to have the properties of aluminum.

2.4.2. Numerical procedure

Details of the numerical procedure are described in Wang et al. [30] and are summarized as follows. The standard finite volume method of Patankar [31] is used to discretize the governing equations, and the central differencing scheme is applied to the advection and diffusion terms. A fully-implicit scheme is used for the time discretization, employing a standard underrelaxation version of the consistent update technique [32] or SUV-CUT. An explicit update scheme is utilized to evaluate the buoyancy source term in Eq. (3) while a pressure-decoupled

solid velocity correction is used to enforce zero velocity in the solid PCM as well as in the other solid parts of the computational domain. A V-cycle based multigrid solver [33] with the SIP [34] smoother is employed to solve the algebraic equations accurately and efficiently. Preliminary predictions were performed using grids up to 300 × 120. A grid size of 252 × 102 with a time step of t = 0.1 s was found to be sufficient to achieve grid and time independent solutions. A convergence criterion of 10^{-6} was specified for all independent variables. Simulation of each two-dimensional melting case typically required 3 days of CPU time using a 3.33 GHz, 4 GB RAM computer.

2.5. Results and Discussion

2.5.1. Comparison of experimental measurements and model predictions

Experiments involving the vertical test cell (θ = 0º) were conducted using powers of P_h = 1, 2, 3 and 4 W. Additional experiments were performed for inclination angles of θ = 5º and θ = 10º, and a power of 3 W. Azimuthal angles in the range $0 \leq \phi \leq 135$º were considered.

Representative raw temperature data are shown in Fig. 2.2. Here, measured temperatures for the $\theta = \varphi = 0°$ configuration with P_h = 3 W are reported. As expected, the thermal response exhibits symmetry about the heated rod; as will become evident, this symmetry is broken when the test cell is tilted.

Measured excess temperatures ($T_e \equiv T - T_i$) for the $\theta = 0°$ configuration and P_h = 1, 2, 3 and 4 W are reported in Fig. 2.3. To demonstrate experimental repeatability, results are shown for two experiments performed at each heater power. For all cases shown in Fig. 2.3, the

measurements reveal that maximum temperatures exist adjacent to the heater (T_7) while minimum temperatures exist in the air gap (T_8), as expected. Temperatures adjacent to the heater increase nearly linearly with time prior to the onset of PCM melting ($T_e \approx 5°C$), plateau during melting, and subsequently increase as the melting process nears completion, also as expected. Overall, the experimental repeatability is considered to be good at the lower power levels, and excellent at higher values of P_h. Differences in temperatures measured for the two experiments are attributed to uncertainties in the tilt angles, and to gas bubbles that periodically form in the molten PCM. (The bubbles were removed periodically using a syringe and hypodermic needle.) The time at which the PCM melts completely (defined as the time when $T_{e,3} \approx T_{e,6} = 5°C$) is $t_{cm} \approx$ 7980, 4350, 3200, and 2590 s for P_h = 1, 2, 3 and 4 W, respectively. Hence, the overall melting time is approximately inversely proportional to the electrical power.

A comparison between the measured (based on the averaged temperatures of the two experiments) and predicted temperatures for the $\theta = 0°$ cases is reported in Fig. 2.4. The agreement is considered to be satisfactory at the lower power levels, and excellent at P_h = 3 W and 4 W. The time needed to achieve $T_{e,3} = T_{e,6} = 5°C$ is predicted to be t_{cm} = 7980, 4390, 3250, and 2640 s for P_h = 1, 2, 3 and 4 W, respectively. Hence, the measured and predicted complete melting times are in excellent agreement.

Representative details of the PCM response to heating are shown in Fig. 2.5. Figure 2.5a illustrates the predicted temporal evolution of the solid-liquid interface for the P_h = 2 W case (note that the very small amount of PCM directly above the copper rod, shown in Fig. 2.1, is not included in Fig. 2.5). As evident, the shape of the interface is affected by free convection, as well as by conduction in the horizontal Teflon end plates, and in the acrylic walls. Temperature and velocity distributions within the molten PCM are shown for the P_h = 2W case at t = 3000 s in

Figs. 2.5b and 2.5c, respectively. The predicted behavior is as expected. Finally, the predicted evolution of the PCM liquid fraction is shown in Fig. 2.5d, with the results exhibiting the expected dependence of the melting rate on the power delivered to the heater.

The overall good agreement between the model predictions and experimental measurements for the two-dimensional melting cases, and the repeatability of the two-dimensional measurements, suggests that experimental measurements for 3D melting (i.e. the effects of tilting the test cell) could be used to benchmark three-dimensional melting models if the conjugate effects included in the current 2D model are included in a three-dimensional model description.

2.5.2. Effects of tilting

Measured temperatures associated with various ϕ and θ with P_h = 3 W are shown in Figs. 2.6 and 2.7. To orient the reader, the thermocouple locations identified with open symbols in Fig. 2.6a ($\phi = 0°$, $\theta = 5°$) are slightly elevated relative to their counterparts on the opposite side of the copper rod (identified by filled symbols). Because of three-dimensional thermal stratification effects, the thermocouples associated with the open symbols experience overall higher temperatures relative to their filled-symbol counterparts in Fig. 2.6a. Measured temperatures are no longer symmetric about the rod, as evident in Fig. 2.2, and the onset of local melting is affected significantly, especially at mid-height (as evident by comparing the T_1 and T_4 behaviors). Breakage of symmetry about the copper rod becomes more pronounced as the tilt angle is increased to $\theta = 10°$ (Fig. 2.7a).

Conditions associated with $\phi = 90°$ are shown in Fig. 2.6c ($\theta = 5°$) and Fig. 2.7c ($\theta = 10°$). To orient the reader, the thermocouples associated with T_2 and T_5 are now at the same

elevation. However, the thermocouple associated with T_5 is closer to the viewer than the one associated with T_2. As expected, the thermal responses associated with the open- and filled-symbol data points are nearly identical, even though the flow is three-dimensional. A comparison between Figs. 2.4c, 2.6c and 2.7c shows that the sensitivity of the thermal response to the tilt angle θ is small when $\phi = 90°$.

The measured thermal responses associated with intermediate values of ϕ are shown in Figs. 2.6b, 2.6d, 2.7b and 2.7d. In Fig. 2.6b (and Fig. 2.7b), the thermocouple associated with T_5 is above and closer to the viewer relative to the thermocouple associated with T_2 whereas in Fig. 2.6d (and Fig. 2.7d) T_2 is above T_5, and T_5 is closer than T_2. As expected, the thermal responses of the open-symbol temperatures of Fig. 2.6b (Fig. 2.7b) are nearly the same as the responses of the filled-symbol temperatures of Fig. 2.6d (Fig. 2.7d) since the open- and closed-symbol thermocouples have, in essence, switched positions. The thermal responses of the $\phi = 45°$ and 135° cases are substantially different than for the $\phi = 0°$ and 90° cases, again reflecting the three-dimensional nature of the flow and heat transfer within the PCM.

Photographs of the PCM taken at t = 1260, 1560 and 2040 s are shown in Fig. 2.8 for ϕ = 0°, θ = 5° (LHS) and $\phi = 0°$, θ = 10° (RHS) with the power set at P_h = 3W. Three views, front (F), left (L), and right (R) are shown at each time. (The view from the back is not included because it is identical to the view from the front). Note that the molten PCM has made contact with the enclosure wall by t = 1260 s for both the θ = 5º and 10º cases, and the melt pool is concentrated in the uppermost portion of the tilted enclosure as expected. By t = 1560 s, the molten PCM has made contact with the entire upper enclosure wall and a highly three-dimensional solid-liquid interface has evolved. As the melting process proceeds, the solid-liquid

interface propagates toward the bottom of the enclosure in a manner similar to the predictions of Fig. 2.5a.

Photographs of the solid PCM were obtained in several additional experiments performed without the embedded thermocouples. In this set of experiments the molten PCM was drained from the test cell and the remaining solid PCM was carefully extracted. Once removed, the solid PCM was cut vertically with a jeweler's saw, through the $\phi = 0°$ plane. Because the solid PCM is destroyed by this procedure, multiple experiments must be performed to document the temporal response of the PCM to each heating condition. At any rate, the exposed faces of the PCM were coated with a thin layer of carbon black and photographed. The blackened faces of the PCM were subsequently digitally enhanced to improve the clarity of the photographs. Figure 2.9 includes results for the θ = 10°, ϕ = 0°, P_h = 3 W conditions. As evident, the solid-liquid interface is of a complex three-dimensional shape, having evolved in response to (i) the 3D convection and heat transfer within the molten PCM and (ii) 3D conjugate effects that are most evident in the vicinity of the lower Teflon plate.

2.6. Conclusions and Recommendations

An experimental investigation of two- and three-dimensional melting of a phase change material has been conducted. Measured temperatures and observations of the solid-liquid interface show that, for the system considered here, strong 3D effects become apparent even at modest ($\theta \approx 5°$) tilt angles. Because a 2D numerical model has been used to predict the melting response of the non-tilted experiments, with good agreement between model predictions and experimental measurement, a model based on similar, three-dimensional physical descriptions could be validated using the three-dimensional experimental results reported here.

Temperature measurement, visualization of the solid PCM, and visualization and/or measurement of flow conditions within the molten PCM could be performed more easily with use of a larger test cell. Moreover, conjugate effects would become less pronounced in a larger experimental apparatus. However, the natural convection within the molten PCM could involve a transition from laminar to turbulent conditions if a larger test cell were to be used. Large scale experiments would, therefore, potentially provide data to validate three-dimensional melting models for PCM melting with turbulent free convection in the molten phase.

Nomenclature

c	specific heat (kJ/kg·K)
f_ℓ	liquid fraction
g	gravitational acceleration (m/s^2)
h	enthalpy (kJ/kg)
$h_{s\ell}$	latent heat of fusion (kJ/kg)
k	thermal conductivity (W/m·K)
P	pressure (Pa)
p	$P+ \rho_m g z$; reduced pressure (Pa)
P_h	heater power (W)
$\dot{q}_h$	heater volumetric heat generation (W/m^3)
r, z	coordinates (m)
s	source term in temperature transforming model
t	time (s)
t_{cm}	complete melting time (s)
T^*	scaled temperature (°C)
T	temperature (°C)
T_e	excess temperature (T - T_i) (°C)
T_i	initial temperature (°C)
T_m	melting temperature (°C)
u, v	velocity components (m/s)
V	heater volume (m^3)

Greek

β	thermal expansion coefficient (K^{-1})
δT	incremental temperature difference (ºC)
θ	inclination angle (degrees)
μ	viscosity (Pa·s)
ρ	density (kg/m^3)

ϕ azimuthal angle (degrees)

Subscripts

ℓ liquid phase

m melting point

s solid phase

Table 2.1. Thermophysical properties.

Property/Material	Octadecane [35]	Copper [36]	Acrylic [37]	Teflon [37]	Brass [37]	Fiber glass [37]	Aluminum [36]
Melting Point, T_m (ºC)	28	-	-	-	-	-	-
Latent heat of fusion, h_{sl} (kJ/kg)	243.5	-	-	-	-	-	-
Density, ρ (kg/m^3)	770	8933	1150	2200	8400	2500	2702
Specific heat, c (kJ/kg·K)	2.16	0.385	1.47	1.022	0.38	0.835	0.903
Thermal conductivity, k (W/m·K)	0.148	401	0.2	0.35	109	0.04	237
Liquid viscosity, μ (Pa·s)	3.09×10^{-3}	-	-	-	-	-	-
Thermal expansion coefficient, β (K^{-1})	9×10^{-4}	-	-	-	-	-	-

Table 2.2. Thermocouple locations relative to the grid of Fig. 2.1a.

Thermocouple	r (mm)	z (mm)
T_1	10	89.1
T_2	10	94.1
T_3	22.8	84.2
T_4	-10	89.1
T_5	-10	94.1
T_6	-22.8	84.2
T_7	5	39.1
T_8	57	43

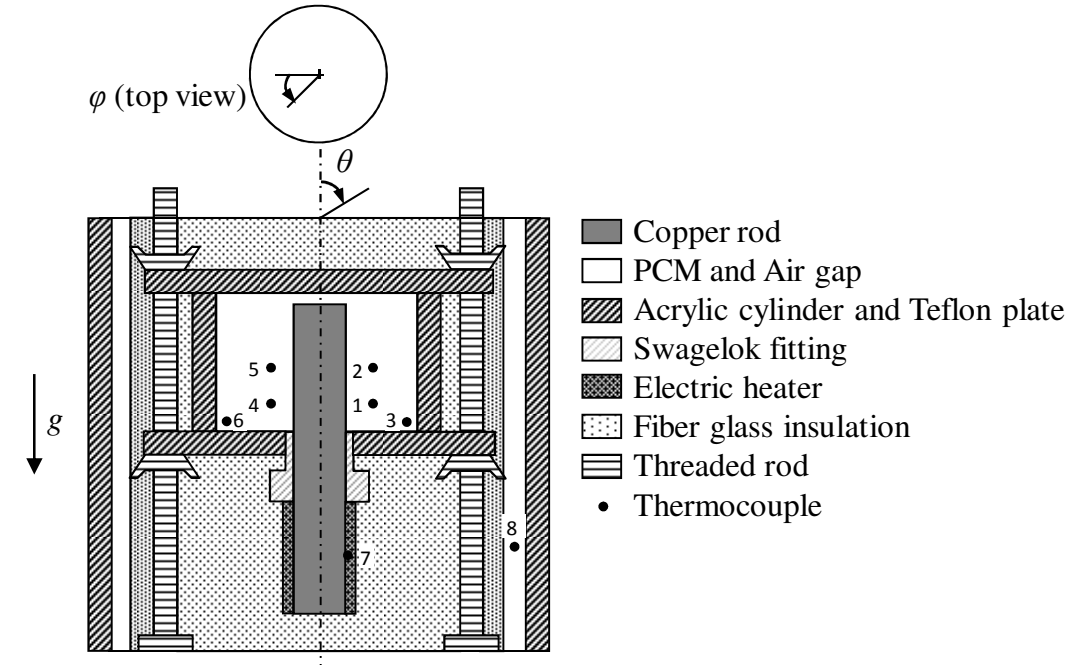

(a)

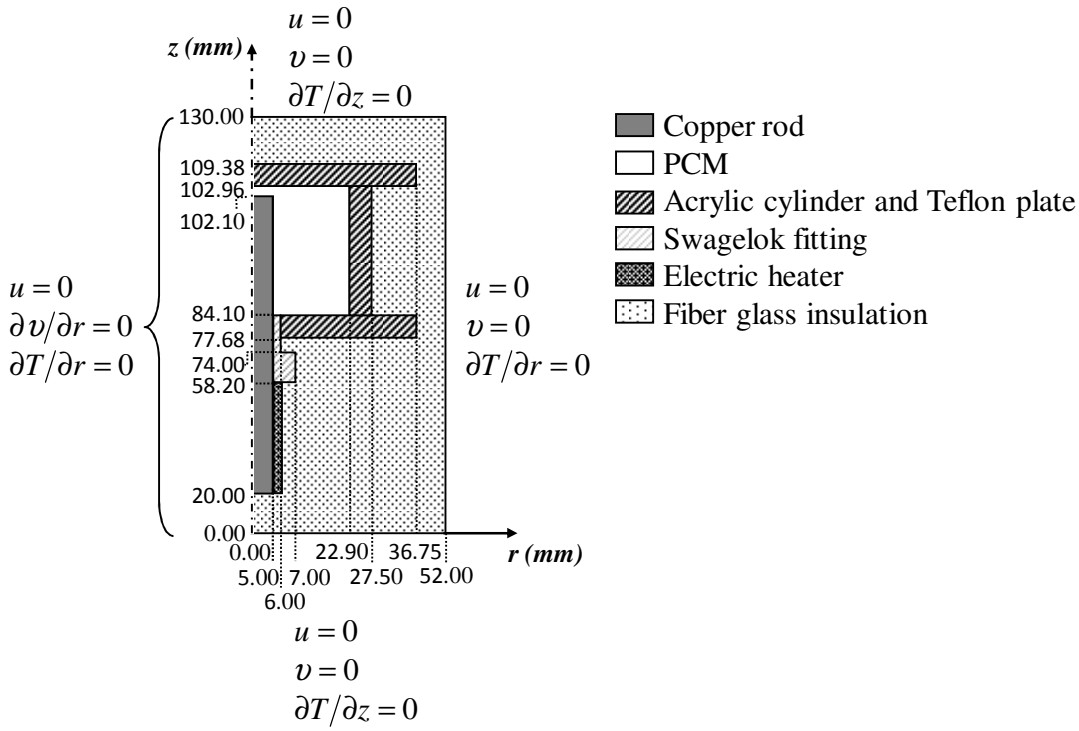

(b)

Fig. 2.1. Experimental apparatus: (a) Schematic, (b) Computational domain and dimensions.

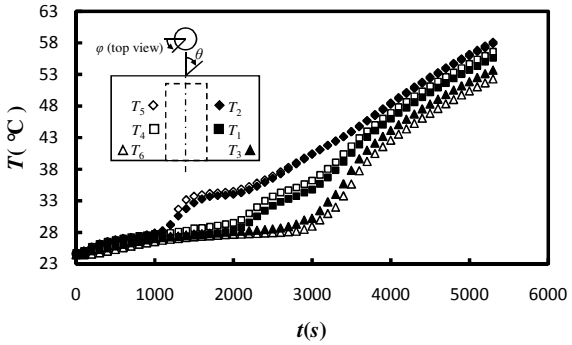

Fig. 2.2. Measured temperatures for $\phi = \theta = 0°$, $P_h = 3$ W.

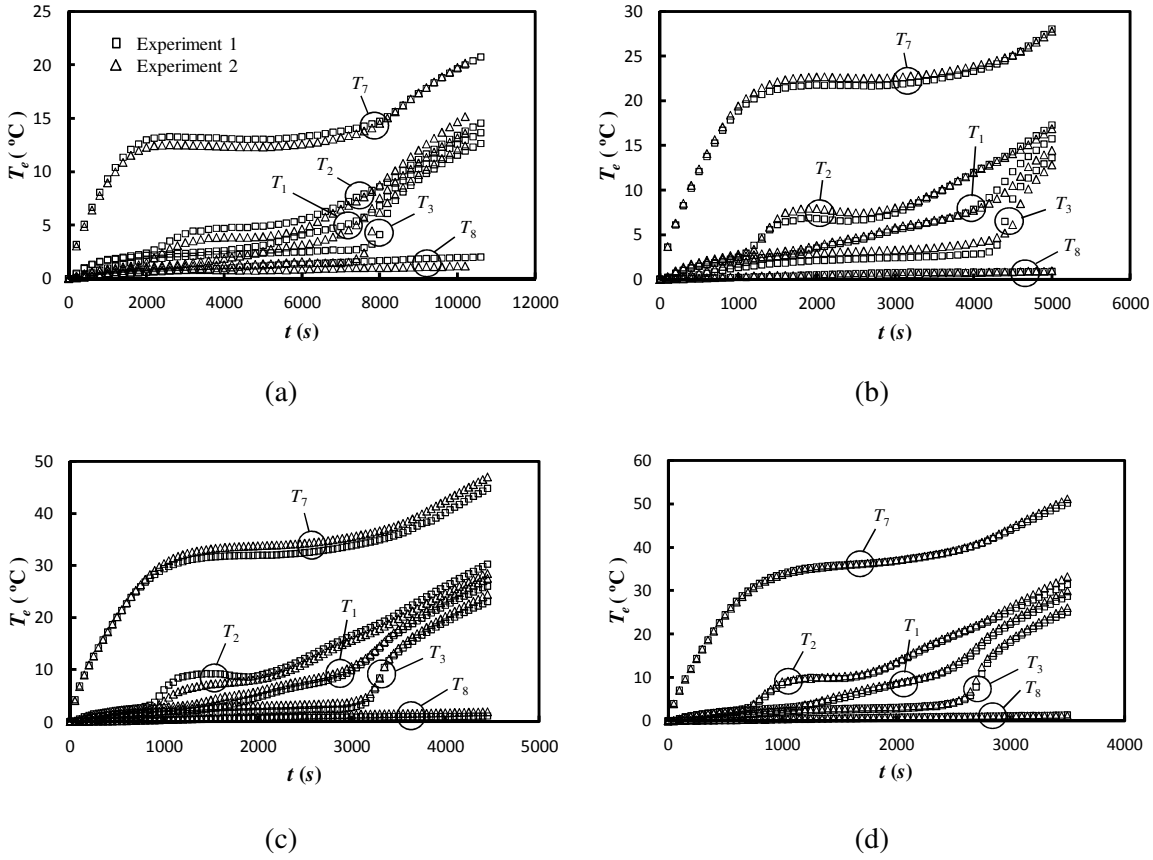

Fig. 2.3. Measured temperatures ($\phi = \theta = 0°$): (a) P_h = 1W, (b) P_h = 2 W, (c) P_h = 3 W, (d) P_h = 4 W.

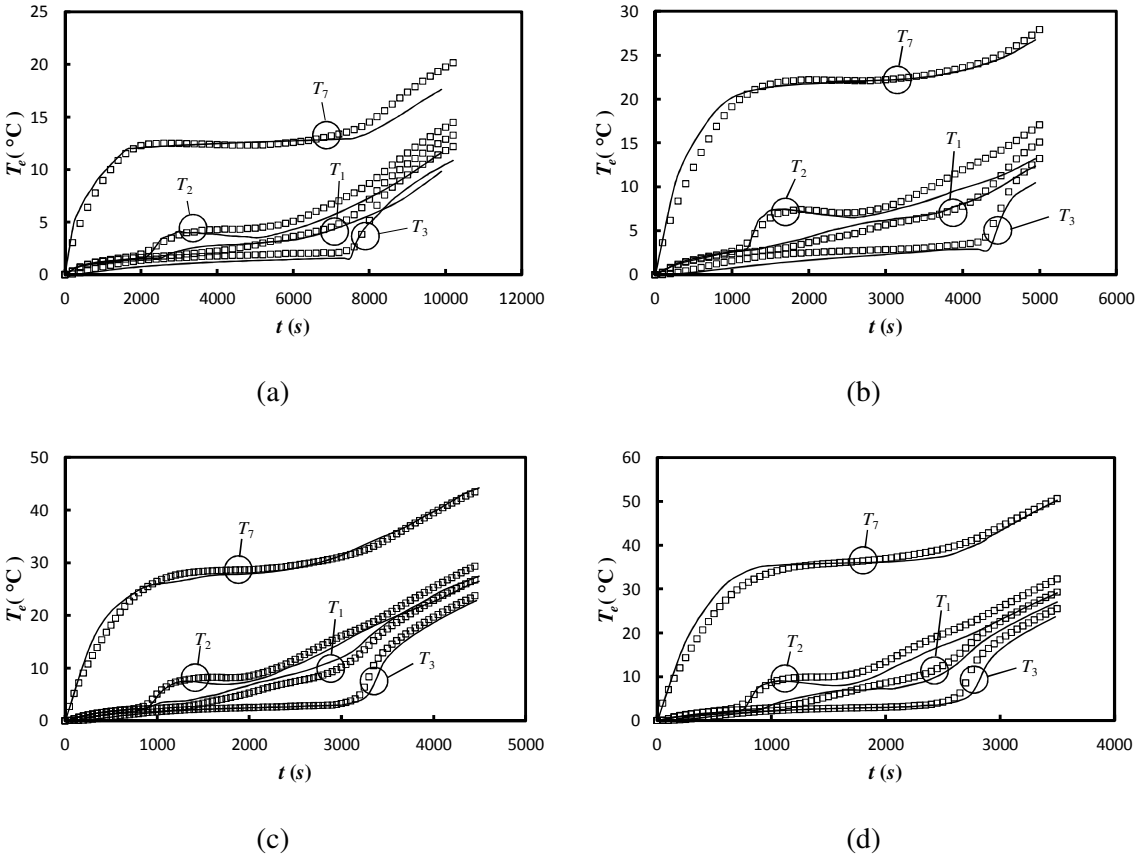

Fig. 2.4. Predicted and measured temperatures ($\phi = \theta = 0°$): (a) P_h = 1W, (b) P_h = 2 W, (c) P_h = 3 W, (d) P_h = 4 W. Measured values are the averages of Experiments 1 and 2.

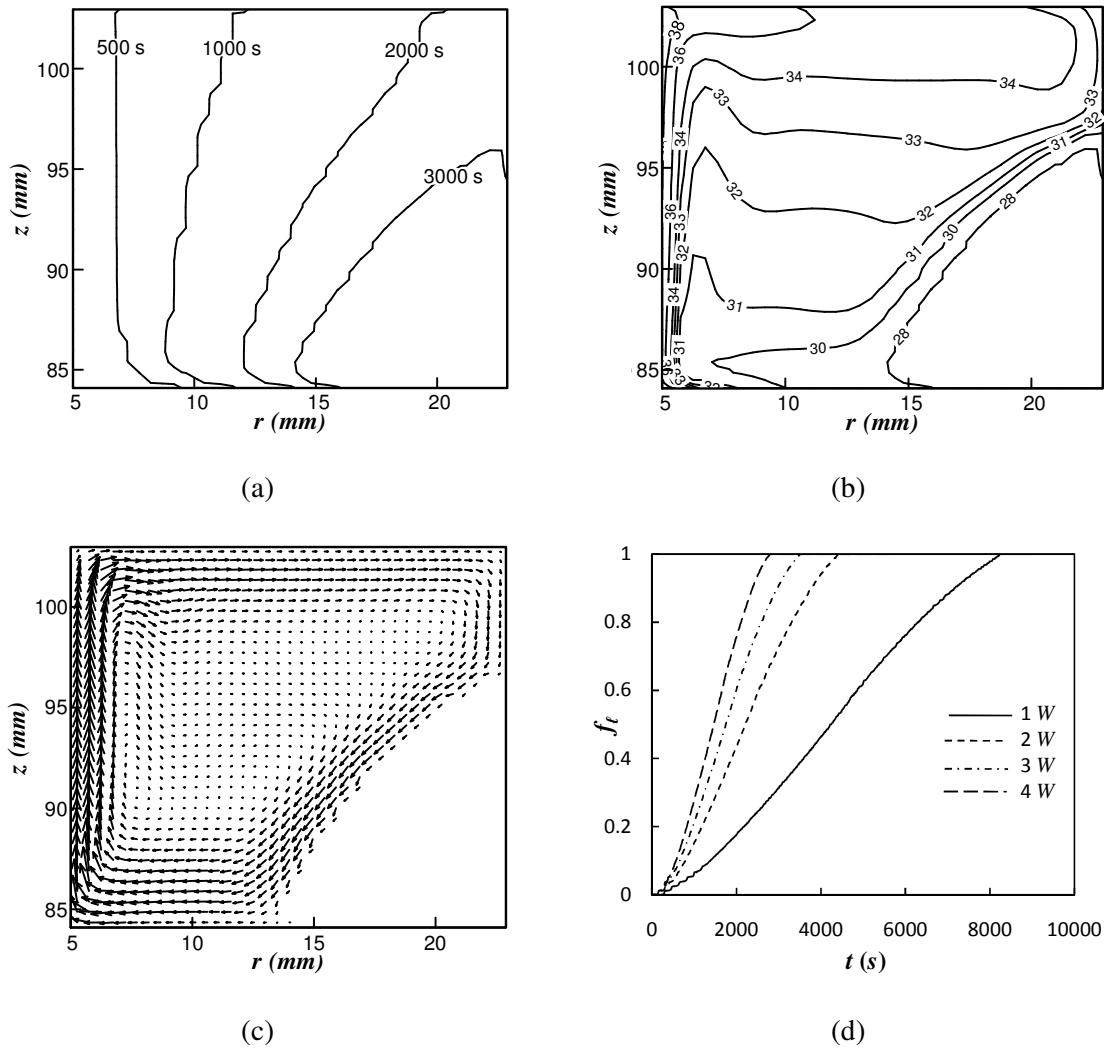

Fig. 2.5. Predicted PCM response ($\phi = \theta = 0°$): (a) Solid-liquid interface locations for P_h = 2 W, (b) Isotherms for P_h = 2 W, t = 3000 s, (c) Velocity vectors for P_h = 2 W, t = 3000 s, (d) Liquid fraction histories for various heating rates.

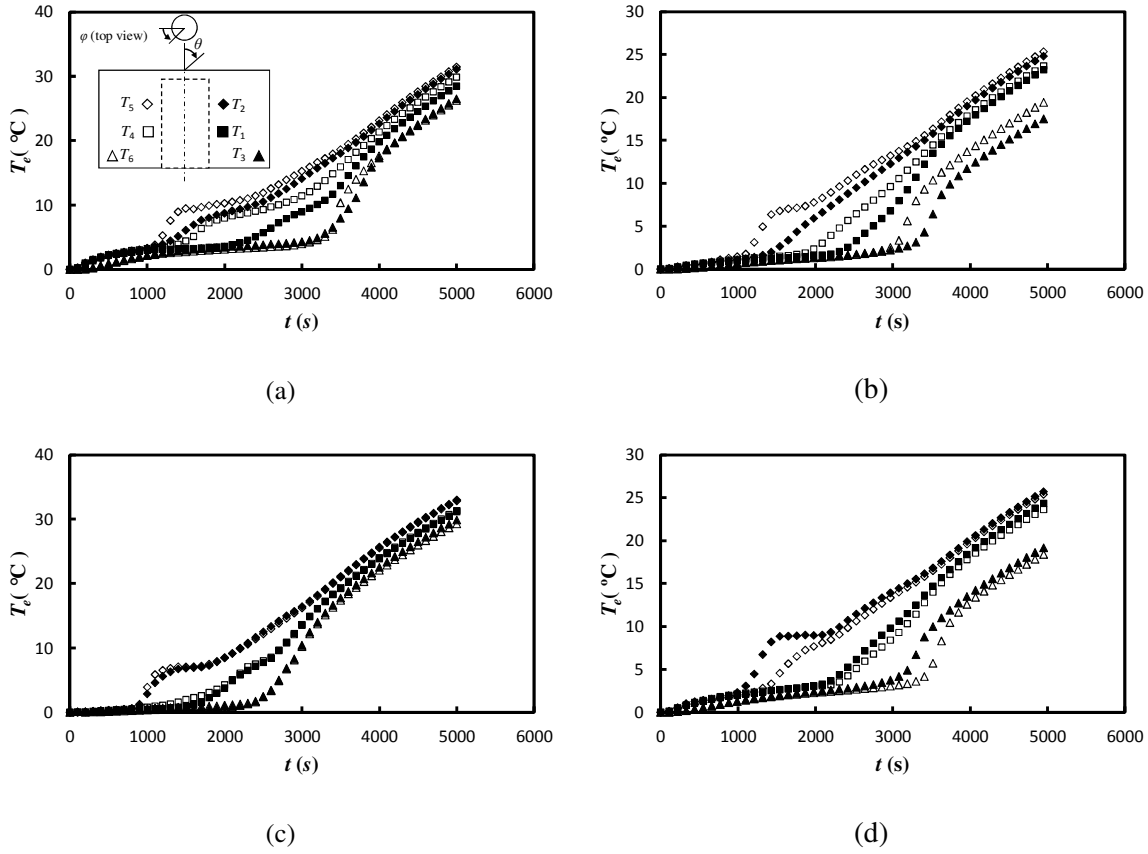

Fig. 2.6. Measured temperatures for $P_h = 3$W, $\theta = 5°$: (a) $\phi = 0°$, (b) $\phi = 45°$, (c) $\phi = 90°$, (d) $\phi = 135°$.

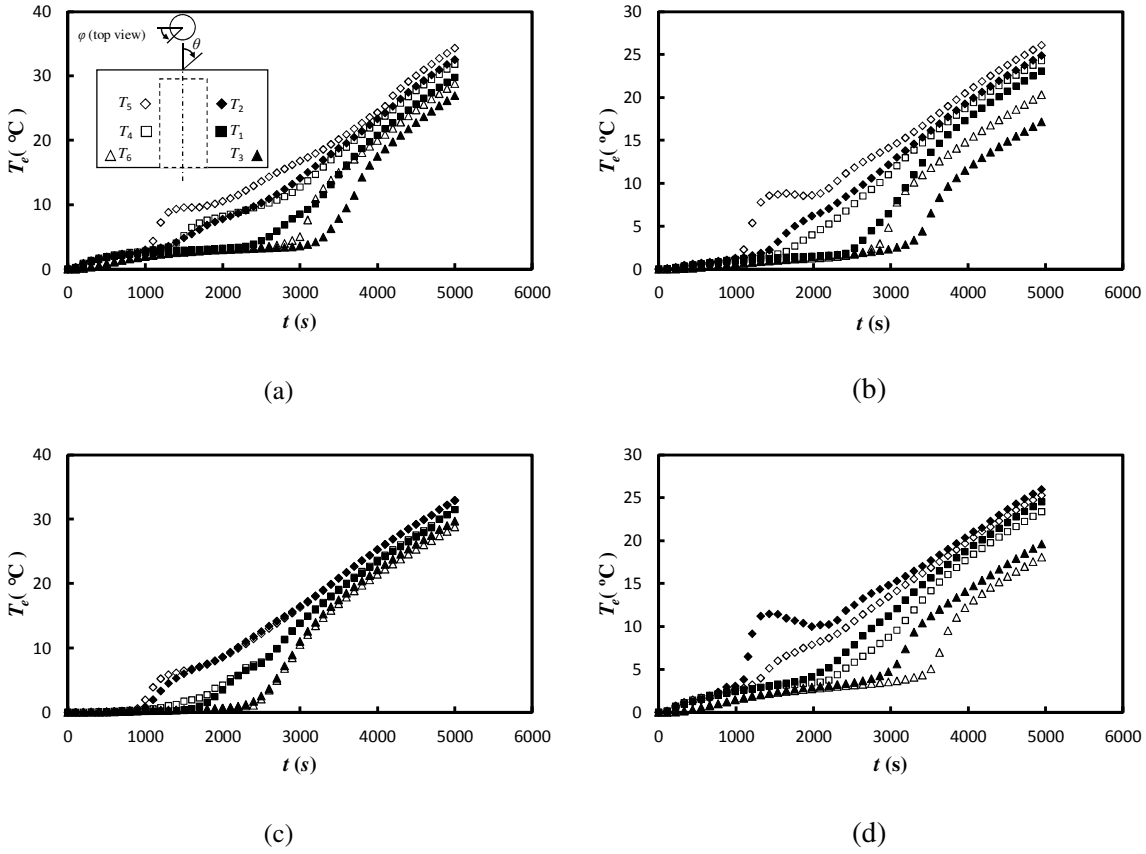

Fig. 2.7. Measured temperatures for $P_h = 3$W, $\theta = 10°$: (a) $\phi = 0°$, (b) $\phi = 45°$, (c) $\phi = 90°$, (d) $\phi = 135°$.

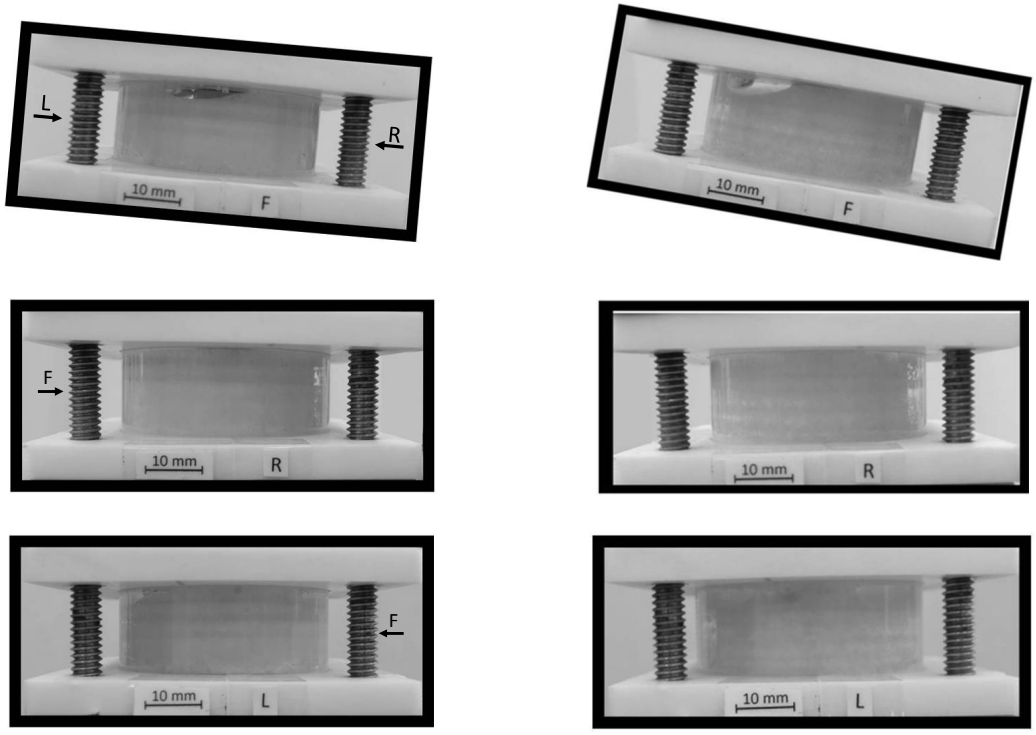

(a)

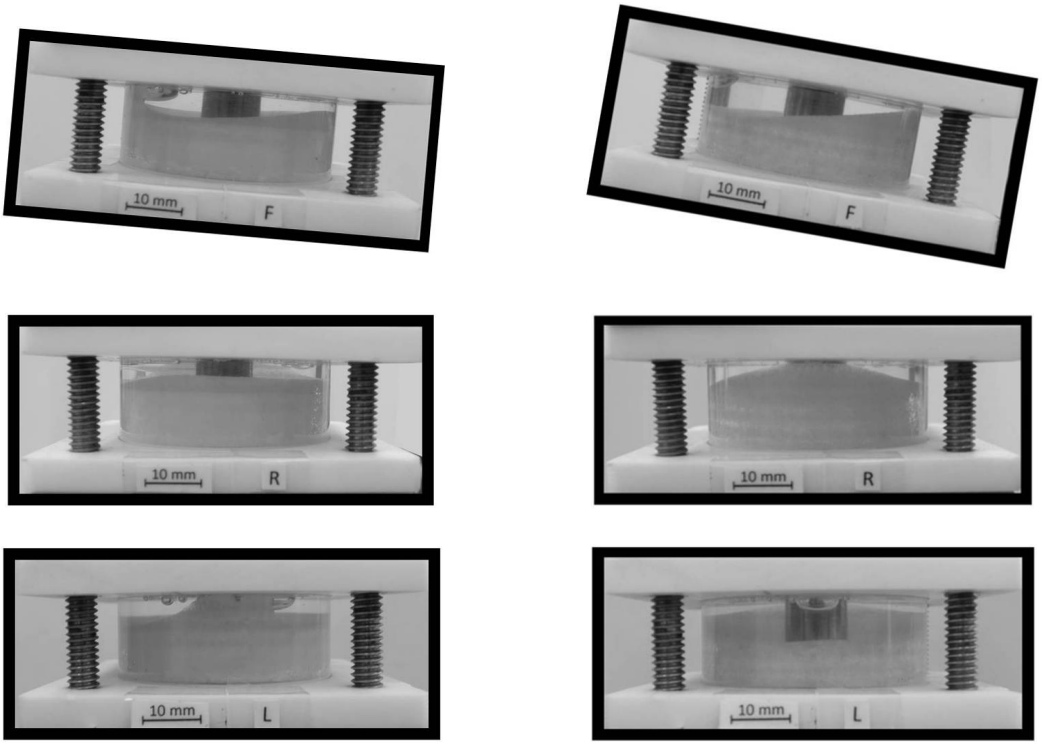

(b)

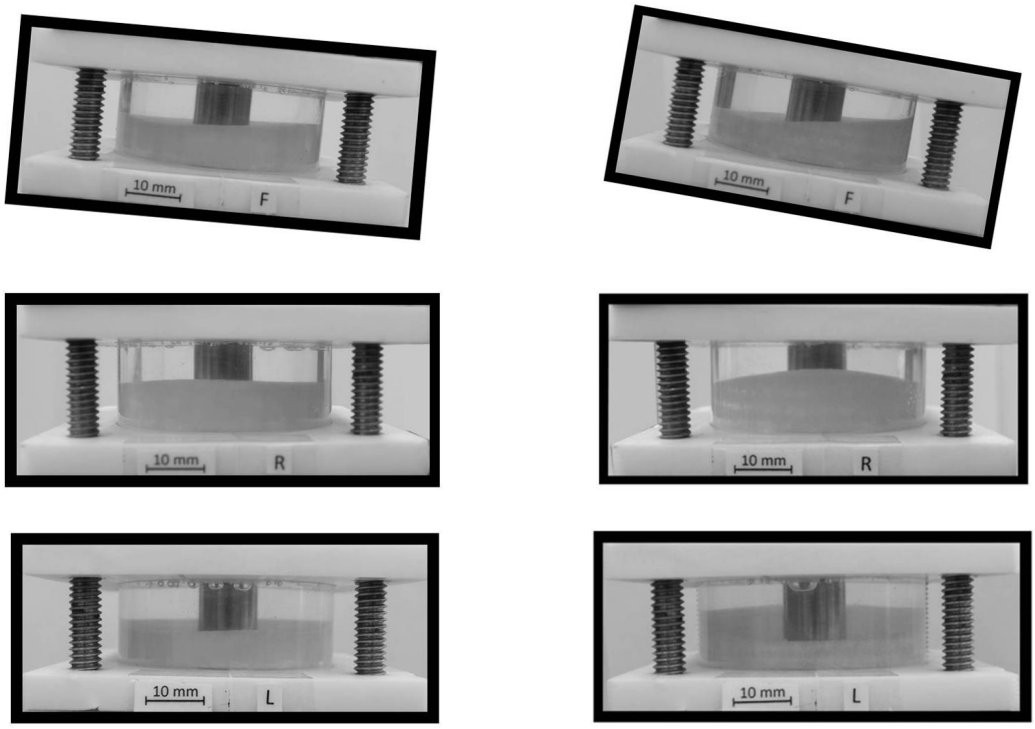

(c)

Fig. 2.8. PCM morphology corresponding to $\phi = 0°$, $\theta = 5°$ (LHS) and $\phi = 0°$, $\theta = 10°$ (RHS) with $P_h = 3$W: (a) $t = 1260$ s, (b) $t = 1560$ s, (c) $t = 2040$ s.

(a)

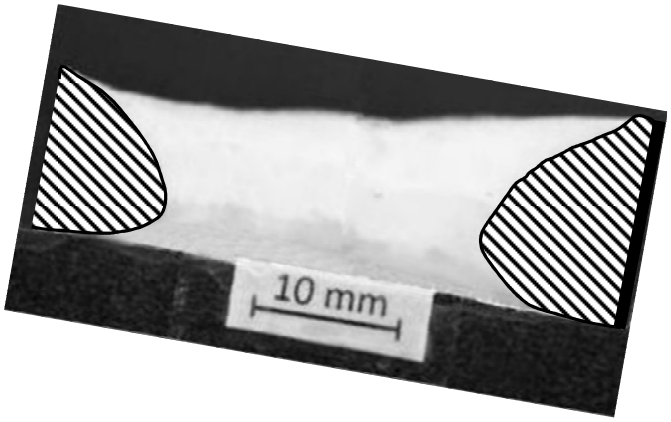

(b)

Fig. 2.9. Cross-section of the solid PCM P_h = 3W, θ = 10°, ϕ = 0°: (a) $t \approx$ 1000 s, (b) $t \approx$ 1700 s.

References

[1] R. Viskanta, Phase-change heat transfer, in G. A. Lane (ed.), Solar Heat Storage: Latent Heat Materials, CRC Press, Boca Raton, Florida, 1983.

[2] R. Viskanta, Natural convection melting and solidification, in S. Kakac, W. Aung, and R. Viskanta (eds.), Natural convection: Fundamentals and applications, Hemisphere, Washington, DC, 1985.

[3] H. Shabgard, T.L. Bergman, N. Sharifi, A. Faghri, High temperature latent heat thermal energy storage using heat pipes, International Journal of Heat and Mass Transfer 53 (15-16) (2010) 2979–2988.

[4] C.W. Robak, T.L. Bergman, A. Faghri, Enhancement of latent heat energy storage using embedded heat pipes, International Journal of Heat and Mass Transfer 54 (15-16) (2011) 3476-3484.

[5] N. Sharifi, S. Wang, T.L. Bergman, A. Faghri, Heat pipe-assisted melting of a phase change material, International Journal of Heat and Mass Transfer 55 (13-14) (2012) 3458-3469.

[6] M. Costa, A. Oliva, C.D. Perez-Segarra, Three-dimensional numerical study of melting inside an isothermal horizontal cylinder, Numerical Heat Transfer Part A - Applications 32 (5) (1997) 531-553.

[7] H. Rieger, U. Projahn, M. Bareiss, H. Beer, Heat transfer during melting inside a horizontal tube, Journal of Heat Transfer 105 (2) (1983) 226-234.

[8] C.J. Ho and R. Viskanta, Heat transfer during inward melting in a horizontal tube, International Journal of Heat and Mass Transfer 27 (5) (1984) 705-716.

[9] E.M. Sparrow, G.T. Geiger, Melting in a horizontal tube with the solid either constrained or free to fall under gravity, International Journal of Heat and Mass Transfer 29 (7) (1986) 1007-1019.

[10] V. Kumar, F. Durst, S. Ray, Modeling moving-boundary problems of solidification and melting adopting an arbitrary Lagrangian-Eulerian approach, Numerical Heat Transfer Part B - Fundamentals 49 (4) (2006) 299-331.

[11] K. Wittig, P.A. Nikrityuk, Three-dimensionality of fluid flow in the benchmark experiment for a pure metal melting on a vertical wall, The 3rd International Conference on Advances in Solidification Processes, IOP Conference Series: Material Science and Engineering 27 (2011) 012054, doi: 10.1088/1757-899X/27/1/012054.

[12] C. Gau, R. Viskanta, melting and solidification of a pure metal on a vertical wall, Journal of Heat Transfer 108 (1) (1986) 174-181.

[13] Y.H. Wang, Y.T. Yang, Three-dimensional transient cooling simulations of a portable electronic device using PCM (phase change materials) in multi-fin heat sink, Energy 36 (8) (2011) 5214-5224.

[14] Y.T. Yang, Y.H. Wang, Numerical simulation of three-dimensional transient cooling application on a portable electronic device using phase change material, International Journal of Thermal Sciences 51 (2012) 155-162.

[15] S.C. Fok, W. Shen, F.L. Tan, Cooling of portable hand-held electronic devices using phase change materials in finned heat sinks, International Journal of Thermal Sciences 49 (1) (2010) 109-117.

[16] M.J. Huang, P.C. Eames, B. Norton, Comparison of predictions made using a new 3D phase change material thermal control model with experimental measurements and predictions made using a validated 2D model, Heat Transfer Engineering 28 (1) (2007) 31-37.

[17] J. Fan, S. Furbo, E. Andersen, Z. Chen, B. Perers, M. Dannemand, Thermal behavior of a heat exchanger module for seasonal heat storage, Energy Procedia 30 (2012) 244-254.

[18] Y. Belhamadia, A.S. Kane, A. Fortin, An enhanced mathematical model for phase change problems with natural convection, International Journal of Numerical Analysis and Modeling Series B 3 (2) (2012) 192-206.

[19] T.A. Kowalewski, M. Rebow, Freezing of water in a differentially heated cubic cavity, International Journal of Computational Fluid Dynamics 11 (3-4) (1999) 193-210.

[20] A. Bermudez, M.V. Otero, Numerical solution of a three-dimensional solidification problem in aluminum casting, Finite Elements in Analysis and Design 40 (13-14) (2004) 1885-1906.

[21] M.J. Huang, P.C. Eames, B. Norton, Comparison of a small-scale 3D PCM thermal control module with a validated 2D PCM thermal control module, Solar Energy Materials and Solar Cells 90 (13) (2006) 1961-1972.

[22] K. Nithyanandam, R. Pitchumani, Computational studies on a latent thermal energy storage system with integral heat pipes for concentrating solar power, Applied Energy 103 (2013) 400-415.

[23] B. Jones, D. Sun, S. Crishnan, S.V. Garimella, Experimental and numerical investigation of melting in a cylinder, International Journal of Heat and Mass Transfer 49 (15-16) (2006) 2724-2738.

[24] A. Faghri, Y. Zhang, Transport Phenomena in Multiphase System, Academic Press, Elsevier, New York, 2006.

[25] A. Faghri, Y. Zhang, Advanced Heat and Mass Transfer, Global Digital Press, Columbia, Missouri, 2010.

[26] Y. Cao, A. Faghri, A Numerical Analysis of Phase Change Problems Including Natural Convection, Journal of Heat Transfer 112 (3) (1990) 812-816.

[27] Y. Cao, A. Faghri, Performance characteristics of a thermal energy storage module: a transient PCM/forced convection conjugate analysis, International Journal of Heat and Mass Transfer 34 (1) (1991) 93-101.

[28] X. Zeng, A. Faghri, A temperature transforming model for binary solid-liquid phase change problems: Part I-Mathematical modeling and numerical methodology, Numerical Heat Transfer Part B-Fundamentals 25 (4) (1994) 467-480.

[29] X. Zeng, A. Faghri, A temperature transforming model for binary solid-liquid phase change problems: Part II-numerical simulation, Numerical Heat Transfer Part B-Fundamentals 25 (4) (1994) 481-500.

[30] S. Wang, A. Faghri, T. L. Bergman, A comprehensive numerical model for melting with natural convection, International Journal of Heat and Mass Transfer 53 (9-10) (2010) 1986-2000.

[31] S.V. Patankar, Numerical Heat Transfer and Fluid Flow, McGraw-Hill, New York, 1980.

[32] W.W. Jin, W.Q. Tao, Y.L. He, Z.Y. LI, Analysis of inconsistency of SIMPLE-like algorithms and an entirely consistent update technique-the CUT algorithm, Numerical Heat Transfer Part B-Fundamentals 53 (4) (2008) 289–312.

[33] J. H. Ferziger, M. Peric, Computational Methods for Fluid Dynamics, Springer, New York, 1996.

[34] H. L. Stone, Iterative solution of implicit approximation of multidimensional partial differential equations, SIAM Journal on Numerical Analysis 5 (3) (1968) 530-558.

[35] M. Lacroix, M. Benmadda, Numerical simulation of natural convection-dominated melting and solidification from a finned vertical wall, Numerical Heat Transfer Part A-Applications 31 (1) (1997) 71-86.

[36] T.L. Bergman, A.S. Lavine, F.P. Incropera, and David P. DeWitt, Fundamentals of Heat and Mass Transfer, seventh ed., Wiley, Hoboken, 2011.

[37] The engineering toolbox, website: http://www.engineeringtoolbox.com/

Chapter 3. Heat Pipe-Assisted Melting of a Phase Change Material

Heat pipe-assisted melting of a phase change material (PCM) housed within a vertical cylindrical enclosure is simulated and is compared to melting induced by heating from an isothermal surface, or with a solid rod or a hollow tube. A parametric study reveals that the heat pipe-assisted melting rates are significantly higher than those associated with the rod or tube, and approach the maximum attainable rates associated with the isothermal surface. Melting rates are enhanced as either the condenser length or the diameter of the heat pipe is increased. The heat pipe is particularly effective in augmenting melting in configurations involving PCM heating from above.

3.1. Introduction

Latent heat thermal energy storage (LHTES) is capable of high energy storage density and reduced storage volume compared to sensible TES systems (Lan and Yang [1]; Liu et al. [2]). However, as is well known, most inexpensive PCMs are characterized by low thermal conductivity for both the solid and liquid phases, limiting the rates of solidification and melting. The large thermal resistance posed by the PCM has limited the use of LHTES in emerging applications such as large scale power generation in conjunction with concentrating solar technologies, and novel LHTES systems have been receiving increased research attention (e.g., He and Zhang [3]; Cui et al. [4]; Tamme et al. [5]; Michels and Pitz-Paal [6]; Cui et al. [7]).

One approach to compensate for the low thermal conductivity of PCMs is to use heat pipes or thermosyphons that are embedded in a PCM to increase heat transfer rates between a hot

(cold) external fluid and the PCM solid-liquid interface during melting (solidification) (Shabgard et al. [8]; Robak et al. [9]; Shabgard et al. [10]; Faghri [11,12]). Since heat pipes utilize vaporization and condensation of a heat pipe working fluid, they can operate with very low thermal resistance, with overall PCM phase change rates determined by a rather complicated conjugate heat transfer process involving the heat pipe (or thermosyphon) and the PCM. Moreover, compared to solid fins of similar dimensions heat pipes have a low thermal capacitance, further improving PCM melting or solidification rates.

A number of different models of varying complexity have been proposed to simulate heat pipe behavior (Faghri [13]). They range from analytical models (e.g., Aghvami and Faghri [14]; Shabgard and Faghri [15]) to detailed 3D numerical models (e.g., Kaya and Goldak [16]). A representative model of intermediate complexity is the HPTAM, a transient 2D model developed by Tournier and El-Genk [17-20], which is capable of determining the liquid-vapor interfacial dynamics and liquid pooling of the heat pipe working fluid. However, the HPTAM utilizes an assumption that the working fluid vapor is always saturated, which may not be satisfied in reality. In models developed by Cao and Faghri [21] as well as Rice and Faghri [22], the vapor is assumed to be saturated only at the wick surface while the transport equations are solved in the vapor region.

The process of PCM melting including the effects of natural convection in the liquid phase has been extensively investigated using numerical simulation. Representative studies of PCM melting in rectangular enclosures are Ho and Viskanta [23], Webb and Viskanta [24], Bergman and Webb [25], Bertrand et al. [26], Gobin and Le Quere [27], Mencinger [28], Hannoun et al. [29], Cao and Faghri [30], and Wang et al. [31,32]. Simulation of melting in cylindrical

enclosures has also received considerable attention. The early work of Sparrow et al. [33] considered melting that is induced from a vertical isothermal cylindrical surface placed concentrically in a cylindrical enclosure housing a PCM. The model involved use of a coordinate transformation to describe the evolving shape of the melt region, and an implicit finite difference approach was employed to simulate natural convection in the melt. Representative of later work, Ismail and Melo [34] developed a finite volume model with a vorticity and stream function formulation to describe the free convection in the molten phase, while Jones et al. [35] combined a finite volume approach with an apparent heat capacity formulation to account for the absorption of latent energy.

Previous studies of heat pipe-PCM systems were mainly based on lumped capacitance analyses and network modeling (e.g., Liu et al. [36]; Nithyanandam and Pitchumani [37]; Shabgard et al. [8]). To the authors' knowledge, there is no full numerical simulation of the complex physical phenomena present in heat pipe-PCM systems.

The primary objective of the present study is to investigate the melting of a PCM that is housed in a cylindrical enclosure, heated by a concentrically-positioned vertical heat pipe using numerical simulation and no empirical correlations. The thermal performance of the heat pipe-PCM system is compared to PCM melting induced by an isothermal surface, or a hot concentric rod or tube. A finite volume-based model is used to simulate the transient response of the conjugate system composed of the heat pipe working fluid, the solid heat pipe wall (or rod or tube), and the surrounding melt region of the PCM.

3.2. Physical Model and Mathematical Formulation

The computational domain and geometric dimensions associated with the heat pipe-PCM system are shown in Fig. 3.1. The vertically-oriented heat pipe is subdivided into three radial regions: the working fluid vapor, the porous wick that is imbibed with the liquid working fluid, and the solid wall. The PCM is contained in the vertical cylindrical annulus of length L_c, which surrounds the condenser section of the heat pipe which is also of length L_c. The adiabatic transport section of the heat pipe (of length L_a) and the heat pipe's evaporator section (of length L_e) form the lower portion of the system. The isothermal surface, rod and tube each have the same exterior dimensions as the heat pipe. The tube has a wall thickness of 1 mm and is evacuated. Heating from below (HFB) and from above (HFA) are both considered, and the direction of heating is specified by switching the orientation of the gravitational acceleration vector.

Several assumptions are employed in the model. All properties are constant except the heat pipe working fluid density. The enclosure walls, as well as the top and bottom circular surfaces of the heat pipe (or rod or tube), are considered to be adiabatic. The solid PCM is pure, the molten PCM is of the same density as the solid, and the melt is a Boussinesq fluid. Natural convection in the molten PCM is two-dimensional, incompressible and laminar. All materials are opaque to thermal radiation, and thermal radiation within the hollow tube and heat pipe is neglected. The vapor phase of the heat pipe working fluid is an ideal gas experiencing two-dimensional laminar compressible flow, and the heat pipe wick is fully saturated. The vapor of the working fluid at the wick surface is saturated, and the liquid flow in the porous wick is neglected (Cao and Faghri [21]). The porous wick is assumed to be capable of providing

adequate capillary pressure to drive the liquid flow through the wick for the operating conditions presented here. The effect of frozen start up of the heat pipe is not considered.

As is evident, numerous physical boundaries separate the various materials, material phases, and components within the conjugate system. Thermal contact resistances are neglected, and the system is described with a single computational domain. The computational domain of Fig. 3.1 is, therefore, subject to the following boundary and initial conditions. Radial gradients of temperature T, pressure p, and velocity component u_z , in addition to velocity component u_r, are zero at $r = 0$. (The inner surface of the hollow tube is also adiabatic). A constant and uniform temperature, T_e, is applied along the vertical exterior of the heat pipe evaporator section. The remaining external boundaries are adiabatic and impermeable, and no-slip conditions are specified. The entire domain is initially at the melting temperature of the PCM. The heat pipe working fluid undergoes a relatively rapid but complex startup as heating ensues.

3.2.1. Descriptive equations for the heat pipe

Based on the preceding assumptions, the vapor flow in the heat pipe is governed by the continuity equation

$$\frac{\partial \rho}{\partial t}+\frac{1}{r}\frac{\partial}{\partial r}\left(\rho r u_r\right)+\frac{\partial}{\partial z}\left(\rho u_z\right)=0 \tag{1}$$

and the r- and z- momentum equations

$$\begin{aligned}\frac{\partial}{\partial t}\left(\rho u_r\right)+\frac{1}{r}\frac{\partial}{\partial r}\left(\rho r u_r^2\right)+\frac{\partial}{\partial z}\left(\rho u_r u_z\right)=&-\frac{\partial p}{\partial r}+\frac{1}{r}\frac{\partial}{\partial r}\left(\mu r\frac{\partial u_r}{\partial r}\right)+\frac{\partial}{\partial z}\left(\mu\frac{\partial u_r}{\partial z}\right)-\frac{\mu u_r}{r^2}+\frac{1}{3}\mu\frac{\partial}{\partial r}\left(\frac{1}{r}\frac{\partial}{\partial r}\left(r u_r\right)+\frac{\partial u_z}{\partial z}\right)\\&+\frac{\partial \mu}{\partial r}\left(\frac{\partial u_r}{\partial r}-\frac{2}{3}\left(\frac{1}{r}\frac{\partial}{\partial r}\left(r u_r\right)+\frac{\partial u_z}{\partial z}\right)\right)+\frac{\partial \mu}{\partial z}\frac{\partial u_z}{\partial z}\end{aligned} \tag{2}$$

$$\frac{\partial}{\partial t}(\rho u_z)+\frac{1}{r}\frac{\partial}{\partial r}(\rho r u_r u_z)+\frac{\partial}{\partial z}(\rho u_z^2)=-\rho g-\frac{\partial p}{\partial z}+\frac{1}{r}\frac{\partial}{\partial r}\left(\mu r\frac{\partial u_z}{\partial r}\right)+\frac{\partial}{\partial z}\left(\mu\frac{\partial u_z}{\partial z}\right)+\frac{1}{3}\mu\frac{\partial}{\partial z}\left(\frac{1}{r}\frac{\partial}{\partial r}(ru_r)+\frac{\partial u_z}{\partial z}\right) \quad (3)$$
$$+\frac{\partial\mu}{\partial z}\left(\frac{\partial u_z}{\partial z}-\frac{2}{3}\left(\frac{1}{r}\frac{\partial}{\partial r}(ru_r)+\frac{\partial u_z}{\partial z}\right)\right)+\frac{\partial\mu}{\partial r}\frac{\partial u_r}{\partial z}$$

The energy equation for the vapor phase of the heat pipe working fluid is

$$\frac{\partial}{\partial t}(\rho h)+\frac{1}{r}\frac{\partial}{\partial r}(\rho r u_r h)+\frac{\partial}{\partial z}(\rho u_z h)=\frac{Dp}{Dt}+\frac{1}{r}\frac{\partial}{\partial r}\left(kr\frac{\partial T}{\partial r}\right)+\frac{\partial}{\partial z}\left(k\frac{\partial T}{\partial z}\right)+\mu\Phi \quad (4)$$

where the viscous dissipation term is

$$\Phi=2\left[\left(\frac{\partial u_r}{\partial r}\right)^2+\left(\frac{u_r}{r}\right)^2+\left(\frac{\partial u_z}{\partial z}\right)^2\right]+\left(\frac{\partial u_r}{\partial z}+\frac{\partial u_z}{\partial r}\right)^2-\frac{2}{3}\left[\frac{1}{r}\frac{\partial}{\partial r}(ru_r)+\frac{\partial u_z}{\partial z}\right]^2 \quad (5)$$

Using the ideal gas equation of state

$$\rho=\frac{p}{RT} \quad (6)$$

and the enthalpy-internal energy relation

$$h=e+\frac{p}{\rho}=c_v T+\frac{p}{\rho} \quad (7)$$

the energy equation can be rewritten as

$$\frac{\partial}{\partial t}(\rho c_v T)+\frac{1}{r}\frac{\partial}{\partial r}(\rho r u_r c_v T)+\frac{\partial}{\partial z}(\rho u_z c_v T)=\frac{1}{r}\frac{\partial}{\partial r}\left(kr\frac{\partial T}{\partial r}\right)+\frac{\partial}{\partial z}\left(k\frac{\partial T}{\partial z}\right)-p\left(\frac{1}{r}\frac{\partial}{\partial r}(ru_r)+\frac{\partial u_z}{\partial z}\right)+\mu\Phi \quad (8)$$

Following Cao and Faghri [21], the porous wick of the heat pipe is assumed to be saturated with liquid, but the liquid velocity is neglected. Therefore, the heat conduction equation for the wick is

$$(\rho c_p)_{eff} \frac{\partial T}{\partial t} = k_{eff}\left[\frac{1}{r}\frac{\partial}{\partial r}\left(r\frac{\partial T}{\partial r}\right)+\frac{\partial^2 T}{\partial z^2}\right] \tag{9}$$

where

$$(\rho c_p)_{eff} = \omega(\rho c_p)_f + (1-\omega)(\rho c_p)_{ws} \tag{10}$$

$$k_{eff} = \frac{k_f[(k_f + k_{ws}) - (1-\omega)(k_f - k_{ws})]}{[(k_f + k_{ws}) + (1-\omega)(k_f - k_{ws})]} \tag{11}$$

according to Faghri [13], where ω is the porosity of the wick.

The temperature distribution in the solid wall of the heat pipe is governed by

$$(\rho c_p)_w \frac{\partial T}{\partial t} = k_w\left[\frac{1}{r}\frac{\partial}{\partial r}\left(r\frac{\partial T}{\partial r}\right)+\frac{\partial^2 T}{\partial z^2}\right] \tag{12}$$

Equation (12) can also be applied to the rod and tube.

3.2.2. Descriptive equations for the PCM

The thermal response of the PCM is governed by the following continuity, momentum and energy equations (Faghri and Zhang [38]; Faghri et al. [39])

$$\frac{\partial u_r}{\partial r} + \frac{u_r}{r} + \frac{\partial u_z}{\partial z} = 0 \tag{13}$$

$$\frac{\partial u_r}{\partial t} + u_r\frac{\partial u_r}{\partial r} + u_z\frac{\partial u_r}{\partial z} = -\frac{1}{\rho}\frac{\partial p}{\partial r} + \nu\left(\frac{\partial^2 u_r}{\partial r^2} + \frac{1}{r}\frac{\partial u_r}{\partial r} - \frac{u_r}{r^2} + \frac{\partial^2 u_r}{\partial z^2}\right) \tag{14}$$

$$\frac{\partial u_z}{\partial t}+u_r\frac{\partial u_z}{\partial r}+u_z\frac{\partial u_z}{\partial z}=-\frac{1}{\rho}\frac{\partial p}{\partial z}+\nu\left(\frac{\partial^2 u_z}{\partial r^2}+\frac{1}{r}\frac{\partial u_z}{\partial r}+\frac{\partial^2 u_z}{\partial z^2}\right)+g\left[\beta(T-T_m)-1\right] \quad (15)$$

$$\frac{\partial h}{\partial t}+u_r\frac{\partial h}{\partial r}+u_z\frac{\partial h}{\partial z}=\frac{1}{\rho}\left[\frac{1}{r}\frac{\partial}{\partial r}\left(kr\frac{\partial T}{\partial r}\right)+\frac{\partial}{\partial z}\left(k\frac{\partial T}{\partial z}\right)\right] \quad (16)$$

One may define a scaled temperature as $T^*=T-T_m$ and express the enthalpy by the temperature transforming model (Cao and Faghri [30]), resulting in

$$h=c(T^*+s) \quad (17)$$

where

$$c=\begin{cases}c_s & T^*<-\delta T\\ \dfrac{c_s+c_\ell}{2}+\dfrac{h_{s\ell}}{2\delta T} & -\delta T\le T^*\le\delta T\\ c_\ell & T^*>\delta T\end{cases} \quad (18)$$

$$s=\begin{cases}\delta T & T^*<-\delta T\\ \delta T & -\delta T\le T^*\le\delta T\\ \dfrac{c_s}{c_\ell}\delta T+\dfrac{h_{s\ell}}{c_\ell} & T^*>\delta T\end{cases} \quad (19)$$

Hence, the energy equation can be written as

$$\frac{\partial(cT^*)}{\partial t}+u_r\frac{\partial(cT^*)}{\partial r}+u_z\frac{\partial(cT^*)}{\partial z}= \frac{1}{\rho}\left[\frac{1}{r}\frac{\partial}{\partial r}\left(kr\frac{\partial T^*}{\partial r}\right)+\frac{\partial}{\partial z}\left(k\frac{\partial T^*}{\partial z}\right)-\frac{\partial(\rho cs)}{\partial t}-u_r\frac{\partial(\rho cs)}{\partial r}-u_z\frac{\partial(\rho cs)}{\partial z}\right] \quad (20)$$

where

$$k = \begin{cases} k_s & T^* < -\delta T \\ k_s + (k_\ell - k_s)\dfrac{T^* + \delta T}{2\delta T} & -\delta T \le T^* \le \delta T \\ k_\ell & T^* > \delta T \end{cases} \tag{21}$$

3.3. Numerical procedure

The detailed numerical methodology used here is described in Wang et al. [31] and is summarized as follows. The standard finite volume method of Patankar [40] is used to discretize the descriptive equations, and the central differencing scheme is applied to the advection and diffusion terms. A fully-implicit scheme is used for the time discretization, employing a standard underrelaxation version of the consistent update technique (Jin et al. [41]) or SUV-CUT. An explicit update scheme is utilized to evaluate the buoyancy source term in the momentum equation. A pressure-decoupled solid velocity correction is used to enforce zero velocity in the solid PCM as well as in the heat pipe wall and wick. A V-cycle based multigrid solver (Ferziger and Peric [42]) with the SIP (Stone [43]) smoother is employed to solve the algebraic equations accurately and efficiently.

In order to apply the SUV-CUT algorithm to the compressible flow in the vapor region of the heat pipe, the formulation of the algorithm was modified as follows.

In the staggered grid configuration, the discretized momentum equation for the velocity component at the east face of the control volume, u_e, yields

$$u_e = \tilde{u}_e + \frac{\alpha_u A_e}{a_e}(p_P - p_E) \tag{22}$$

$$\tilde{u}_e = (1-\alpha_u)u_e^0 + \frac{\alpha_u}{\alpha_e}\left(\sum a_{nb}u_{nb}^0 + b\right) \tag{23}$$

where $\tilde{u}_e$ is the explicit velocity, and α_u is the underrelaxation factor for u_e. Using the ideal gas equation of state, Eq. (1) can be integrated as

$$(\rho uA)_e - (\rho uA)_w + (\rho vA)_n - (\rho vA)_s + \left(\frac{p_P}{T_P} - \frac{p_P^{t_0}}{T_P^{t_0}}\right)\frac{V}{R\Delta t} = 0 \tag{24}$$

Substituting velocities in the form of Eq. (22) into Eq. (24), an implicit equation for pressure is obtained as

$$a_P p_P = a_E p_E + a_W p_W + a_N p_N + a_S p_S + b_p \tag{25}$$

where

$$a_P = a_E + a_W + a_N + a_S + \frac{V}{T_P R\Delta t} \tag{26}$$

$$a_E = \frac{\alpha_u \rho A_e^2}{a_e}, a_W = \frac{\alpha_u \rho A_w^2}{a_w}, a_N = \frac{\alpha_v \rho A_n^2}{a_n}, a_S = \frac{\alpha_v \rho A_s^2}{a_s} \tag{27}$$

$$b_p = -\left[(\rho\tilde{u}A)_e - (\rho\tilde{u}A)_w + (\rho\tilde{v}A)_n - (\rho\tilde{v}A)_s\right] + \frac{p_P^{t_0}V}{T_P^{t_0}R\Delta t} \tag{28}$$

In the above formulation, superscript 0 denotes quantities at the previous iterative level, while superscript t_0 denotes quantities at the previous time step.

At the vapor-wick interface, the vapor is assumed to be saturated, i.e., its temperature and pressure are dependent upon each other. There are two approaches to apply this saturation

condition during the coupling between the energy equation and the flow equations. In the first approach, the vapor temperature is specified as the saturation temperature corresponding to the vapor pressure, while the interface velocity is determined by the energy balance and used to drive the vapor flow and calculate the pressure field. This is the approach both Cao and Faghri [21] and Rice and Faghri [22] employed. A shortcoming associated with this approach is that, for essentially incompressible vapor flow, the pressure cannot be uniquely determined, causing problem with convergence. In order to "let the operating pressure of the system float," Rice and Faghri [22] employed given pressure condition to replace the zero velocity condition "at the end of the vapor core closest to the condenser." In this case, the zero velocity at the condenser end is only approximately satisfied, while the solution procedure is significantly complicated. Cao and Faghri [21] did not encounter this problem, because they applied outflow condition at the vapor-wick interface of the condenser section, which is only valid for upwind difference scheme, and the vapor saturation condition is only satisfied at the interface of the evaporator and adiabatic sections.

In this study, an alternative approach to enforce the saturation condition at the vapor-wick interface is used, i.e., the saturation pressure is specified corresponding to the interfacial vapor temperature via the Clausius-Clapeyron equation

$$p_{v,i} = p_{sat}(T_{v,i}) = p_{ref} \exp\left[\frac{h_{fg}}{R}\left(\frac{1}{T_{ref}} - \frac{1}{T_{v,i}}\right)\right] \tag{29}$$

Meanwhile, the interfacial velocity is determined by the mass balance of the vapor control volumes adjacent to the interface where the pressure is specified rather than temperature, and the latent heats corresponding to the interfacial velocities are applied as source terms in the energy

equations of the vapor control volumes. This approach allows the vapor pressure to be uniquely determined for both incompressible and compressible vapor flows, and the interface temperature distribution naturally controls the saturated pressure drop to drive the flow. Therefore, all the governing equations are strictly satisfied, while the saturation condition and latent heat exchange are enforced along the entire vapor-wick interface.

The melting sub-model has been verified by Wang et al. [31,32] and Sharifi et al. [44]. Simulation of a stainless steel, sodium-filled heat pipe, which has been modeled previously by Cao and Faghri [21] and Rice and Faghri [22], is conducted here to validate the heat pipe portion of the overall model. The evaporator wall of the heat pipe considered in the references is heated with 623 W to a steady state ($t < 0$ s), then the heat input is suddenly increased (at $t = 0$ s) to 770 W. The condenser section of the heat pipe is subjected to the convective cooling conditions reported in [21]. Figure 3.2 shows the predicted vapor temperature evolution using a 40×36 grid and a time step of 0.5 s. The predictions of the current model are in good quantitative agreement with those of (i) Cao and Faghri [21] which were, in turn, validated with the experimental results of Ivanovskii et al. [45] and Bowman [46], as well as (ii) Rice and Faghri [22] which were validated with the experimental results of Faghri and Buchko [47]. Preliminary simulations using a convergence criterion of 10^{-5} for all variables were performed using grid sizes of 100×80, 80×70, and 40×35 as well as time steps of 0.1 and 0.2 s for the $L_c = 70$ mm, $D_{hp} = 14$ mm case. The predictions were found to be essentially independent of the time step. A grid of 80×70 resulted in instantaneous PCM liquid fractions within 1% of those predicted using the finest grid, while the 40×35 grid resulted in differences of 15% relative to the finest grid. Hence, the

predictions reported here, using a 80×70 grid and a time step of 0.1 s, are considered to be grid size and time step independent.

3.4. Results and discussion

Heat pipes of diameters $D_{hp} = 2r_{hp} = 9$ mm and 14 mm are considered here, each with wall and wick thicknesses of 1 mm. The screened wick has a porosity of $\omega = 0.9$ while the heat pipe evaporator and adiabatic transport sections are $L_e = 25$ mm and $L_a = 5$ mm, respectively. PCM dimensions of $r_i = r_{hp}$, $r_o = 35$ mm and $L_c = 23$ mm, 35 mm and 70 mm are specified, corresponding to *short, medium* and *tall* modules, respectively.

Specification of the heat pipe working fluid is linked to the properties of the specific PCM of interest, since the saturation temperature of the working fluid must be matched to the melting temperature of the PCM. In this study, the PCM is sodium nitrate ($NaNO_3$, $T_m = 580$ K), and the heat pipe working fluid is potassium (K, with p_{sat} at $T_{sat} = T_m = 580$ K). The properties of the heat pipe wick and wall, as well as the rod and tube, correspond to 304 stainless steel, since this metal is chemically compatible with both K and $NaNO_3$. (Faghri [13]; Dussinger and Anderson [48]; Goods and Bradshaw [49]; Bradshaw and Siegel [50]; Attia et al. [51]; and Kenisarin [52]) The relevant thermophysical properties are provided in Table 3.1.

Each simulation begins with the PCM in the solid phase and all temperatures at $T_m = 580$ K. The external vertical surface of the heat pipe evaporator length (or rod or tube) is then raised to $T_e = 591.1$ K, which corresponds to a Stefan number of 0.1 for the PCM.

Figure 3.3 shows temperature distributions within the tall, $L_e = 70$ mm module equipped with the $D_{hp} = 14$ mm heat pipe (top), rod (middle), and tube (bottom) at various times associated

with similar melt fractions for the three cases. A melt fraction of $f_\ell \approx 0.67$ is achieved at t = 3, 7 and 9 h for the heat pipe, rod and tube, respectively. Since the thermal resistance posed by the heat pipe is small (as is its thermal capacitance) relatively uniform temperatures exist along the length of its condensing section, inducing the highest melting rates. Temperature distributions within the working fluid of the heat pipe bear similarity to those reported elsewhere (Harley and Faghri [53]; Cao and Faghri [21]) and are influenced by vapor velocities as high as ≈100 m/s. As expected, melting along the heat pipe is nearly uniform at early times (t = 0.5 h), since heat transfer within the molten PCM is conduction-dominated. As the melt region expands and natural convection becomes established, melting rates become more pronounced near the top of the enclosure, as warm molten PCM is brought into proximity with the PCM solid-liquid interface by way of the overall clockwise circulation in the melt.

In contrast to the heat pipe case, melting rates associated with the tube (Fig. 3.3c, which might be considered to be an *unfilled* heat pipe) are very low. The large thermal resistance posed by the thin tube wall leads to sharp reductions in temperatures along the tube length, reducing both temperatures and fluid velocities in the melt relative to the heat pipe case and confining melting to the lower portions of the PCM at early times. The onset of melting at the upper PCM boundary is delayed to $t \approx 4$ h, and melting rates in the upper region are low overall. Use of the solid rod (Fig. 3.3b) induces intermediate melting rates, with melt region topographies bearing similarity to those of the tube at early times (t = 0.5 h) when warm temperatures have not yet propagated extensively to the upper sections of the rod, and to those of the heat pipe at later times (t = 7 h) during which the rod is more uniformly-warm. The predictions are in qualitative

agreement with experimental measurements of heat pipe- and rod-assisted PCM melting (Robak et al. [9]).

Since warm rod and tube temperatures exist in the lower portions of the tall module at the times shown in Fig. 3.3, it might be expected that the thermal performance of the three configurations becomes similar if a shorter enclosure were to be considered. Temperature distributions within the short (L_e = 23 mm) module equipped with the D_{hp} = 14 mm heat pipe (top), rod (middle), and tube (bottom) are included in Fig. 3.4. As expected, the melt region topography is similar for the three configurations, and melting rates corresponding to the heat pipe, rod and tube exhibit less disparity, relative to those of the tall module of Fig. 3.3.

Representative locations of the PCM solid-liquid interface are shown in Fig. 3.5 for the tall, medium and short modules (top to bottom) equipped with either the large (LHS) or small (RHS) diameter heat pipes, rods or tubes. Also included are predictions associated with an isothermal cylindrical surface of diameter D_{hp}. Interface locations are shown for early (t_1) and late (t_2) times, as indicated in the figure legends.

Melting rates associated with the tall module (Fig. 3.5a) are highest for the isothermal surface, with complete melting occurring at $t < t_2$ for either the large (D_{hp} = 14 mm) or small (D_{hp} = 9 mm) diameter surface. This corresponds to the maximum possible melting rate associated with the T_e = 591.1 K boundary condition. The lowest melting rates are induced by the tube, while melting rates associated with the heat pipe exceed those of the rod. Melting is slower for the D_{hp} = 9 mm cases relative to the D_{hp} = 14 mm cases, as expected. The medium (Fig. 3.5b) and short (Fig. 3.5c) modules exhibit similar trends, with the highest-to-lowest melting rates

associated with the isothermal surface, heat pipe, rod, and tube, respectively. In each case, melting from the isothermal surface is completed at $t < t_2$.

For each HFB scenario considered here, the highest melting rates are induced by the isothermal surface, followed by the heat pipe, the solid rod, and the hollow tube. The corresponding liquid fraction histories are summarized in Fig. 3.6 (Fig. 3.7) for D_{hp} = 14 mm (D_{hp} = 9 mm) for the tall, medium and short modules. The relative performance of each configuration may be quantified in terms of a melting effectiveness,

$$\varepsilon = \frac{f_\ell(t)}{f_{\ell,bc}(t)} \tag{30}$$

where $f_{\ell,bc}(t)$ is the instantaneous liquid fraction associated with a base case. Since the isothermal surface condition provides the limiting case behavior, it could be used as the base case so that $0 < \varepsilon < 1$. However, because the isothermal surface completely melts the PCM more rapidly than the other cases, its specification as the base case would result in the effectiveness being defined only during the initial stages of the melting processes associated with the heat pipe, rod or tube. As such, melting associated with the rod is specified here to represent the base case, and the time histories of the effectiveness for the isothermal condition, the heat pipe, and the tube are reported in Figs. 3.6 and 3.7. For D_{hp} = 14 mm (Fig. 3.6), the effectiveness of the heat pipe is greater than unity and increases as the module becomes taller. In contrast, the effectiveness of the hollow tube is less than unity, but increases as the module height is reduced. Both trends are expected, based upon the discussion of Figs. 3.3 and 3.4. Because the hollow tube is of the identical dimensions and is constructed of the same wall material as the heat pipe,

it can be viewed as a partially inoperative heat pipe, perhaps due to the presence of a non-condensing gas (Faghri [13]).

Trends similar to those noted in Fig. 3.6 are evident in Fig. 3.7. For the D_{hp} = 9 mm cases, however, the effectiveness of the isothermal surface condition is, in general, higher than for D_{hp} = 14 mm since the thermal resistance posed by the more slender rod (base case) is larger. The heat pipe and tube effectiveness values are similar to those reported in Fig. 3.6.

As evident in all the HFB results, including those involving isothermal cylindrical surfaces, natural convection in the molten PCM plays an important role in driving the melting process. Although melting rates associated with the isothermal inner surfaces are independent of the vertical orientation of the module, melting rates for heat pipes, rods or tubes may be sensitive to the module orientation, and this sensitivity may be most significant for the tube since warm temperatures are confined to lower (upper) regions of the tube and PCM for HFB (HFA).

Figure 3.8 includes HFA results for the tall module and larger diameter inner surface for the heat pipe, rod and tube. Because of its ability to promote nearly uniform warm temperatures along its entire length, the heat pipe induces HFA melting rates (Fig. 3.8a) that are only slightly reduced relative to HFB (Fig. 3.3a). In remarkable contrast, HFA melting rates for the rod (Fig. 3.8b) and tube (Fig. 3.8c) are reduced dramatically relative to those for HFB (Figs. 3.3b and 3.3c) because warm temperatures are confined to the upper regions of the PCM by very weak natural convection circulations, advecting thermal energy in the molten PCM in the upward direction in the vicinity the tube or rod, offsetting the downward-propagating conduction in the tube or rod. The liquid fraction and effectiveness histories associated with the predictions of Fig.

3.8 are shown in Fig. 3.9, again indicating the high effectiveness of the heat pipe, and poor performance of the rod and tube.

3.5. Conclusions and recommendations

A numerical model has been developed to quantitatively determine the augmentation of PCM melting associated with use of embedded, vertically-oriented heat pipes, solid rods, or hollow tubes. Both heating from below (HFB), and heating from above (HFA) configurations have been considered for various inner surface (heat pipe) diameters, and enclosure heights. An effectiveness has been defined and used to quantify the performance of the heat pipe and tube relative to the solid rod.

Melting rates are governed by transient and coupled heat transfer effects including (i) conduction in the heat pipe walls, rod and tube, (ii) vaporization, condensation and compressible flow of the heat pipe working fluid, and (iii) natural convection in the PCM melt that is of evolving topography. In all cases considered here, the heat pipe provides the largest PCM melting enhancement, relative to either the rod or tube. Melting rates are enhanced as either the condenser length or the diameter of the heat pipe is increased. The heat pipe performs consistently well for both HFB and HFA, whereas the performance of the rod and tube is especially poor for HFA.

Taking into account the superior performance of heat pipes, they may be a preferred option to enhance heat transfer rates in latent heat thermal energy storage systems. Moreover, since less solid material is needed to construct a heat pipe compared to a solid rod of the same dimensions, heat pipes may also be attractive from an economic perspective. However, the poor performance of the hollow tube, which is of the same material and dimensions as the heat pipe,

underscores the need to develop heat pipes capable of providing reliable, long-term operation so that their performance does not deteriorate over time to eventually mimic that of the hollow tube. Finally, latent heat thermal energy storage involves sequential melting and solidification of the PCM. Heat pipe-induced PCM solidification has yet to be modeled on a detailed basis, although experiments have shown that heat pipes can offer substantial improvement in thermal performance relative to extended solid surfaces (rods) of similar dimension (Robak et al. [9]).

Nomenclature

a	coefficient in the discretized equation
A	area (m^2)
b	source term in the discretized equation
c	specific heat (J/kg·K)
c_p	specific heat at constant pressure (J/kg·K)
c_v	specific heat at constant volume (J/kg·K)
D	diameter (m)
e	internal energy (J/kg)
f_ℓ	volumetric liquid fraction
g	gravitational acceleration (m/s^2)
h	enthalpy (J/kg)
h_{fg}	latent heat of evaporation (kJ/kg)
$h_{s\ell}$	latent heat of fusion (kJ/kg)
k	thermal conductivity (W/m·K)
L	length (m)
p	pressure (Pa)
r,z	coordinate directions (m)
R	gas constant (J/kg·K)
s	source term in temperature transforming model
t	time (s)
T	temperature (K)
T_m	melting temperature (K)
u	velocity component (m/s)
V	volume (m^3)
Greek	
α	underrelaxation factor
β	thermal expansion coefficient (K^{-1})
δT	half width of temperature range (K)

ε	effectiveness
Φ	viscous dissipation (J/kg·m^2)
μ	dynamic viscosity (Pa·s)
ν	kinematic viscosity (m^2/s)
ρ	density (kg/m^3)
ω	porosity

Subscripts

a	adiabatic
bc	base case
c	condenser
e	evaporator
e,w,n,s	neighboring velocity grid points
eff	effective
E, *W*, *N*, *S*	neighboring temperature and pressure grid points
f	liquid phase of heat pipe working fluid
hp	heat pipe
i	wick-vapor interface, inner
ℓ	liquid phase of PCM
nb	neighboring grid points
o	outer
p	pressure
P	center grid in staggered grid
r,z	coordinate directions
ref	reference
s	solid phase of PCM
sat	saturation
u,v	velocity components
v	vapor phase of heat pipe working fluid
w	heat pipe wall
ws	solid material of wick structure

Table 3.1. Thermophysical properties at T_m = 580 K.

	PCM	Heat pipe working fluid	Heat pipe, rod or tube
Material	Sodium nitrate [1]	Potassium [13]	304 Stainless steel [54]
Density, ρ (kg/m^3)	2000	766.9	7900
Thermal conductivity, k (W/m·K)	0.57	43.85 (liquid) 0.0106 (vapor)	19.8
Specific heat, c_p (J/kg·K)	1730	771 (liquid) 81.94 (vapor)	557
Viscosity, μ (Pa·s)	3.02×10^{-3}	2.38×10^{-4} (liquid) 98.65×10^{-7} (vapor)	
Latent heat, h_{sl} or h_{fg} (kJ/kg)	182	2143	
Melting point, T_m (K)	580		
Vapor pressure, p_{sat} (Pa)		92.58	
Thermal expansion coefficient, β (K^{-1})	6.6×10^{-4}		

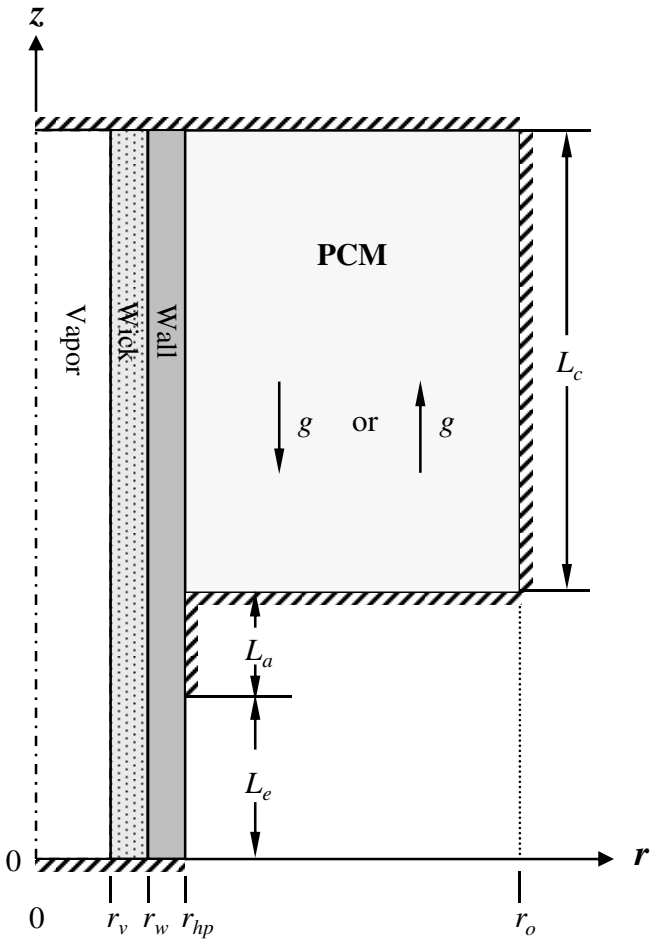

Fig. 3.1. Physical model and computational domain for the heat pipe and PCM.

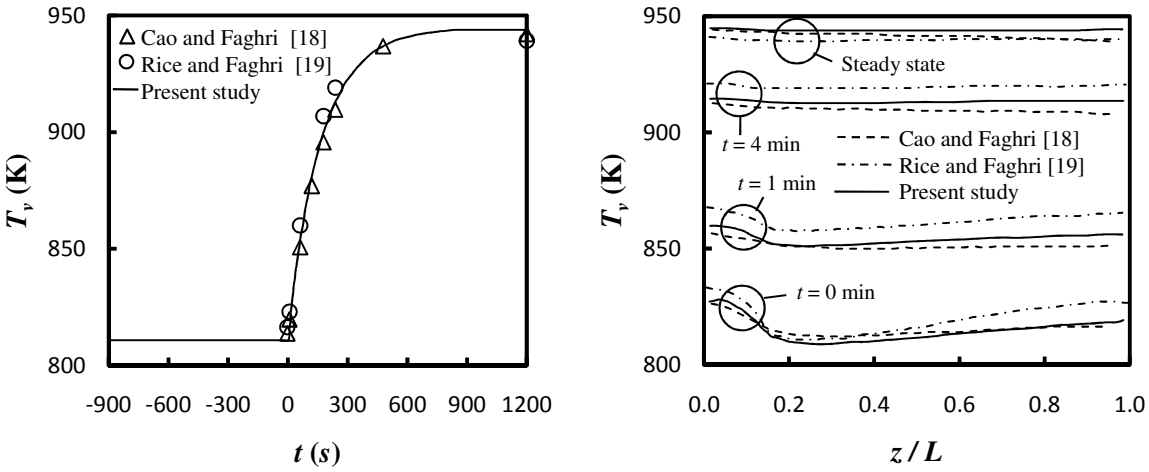

Fig. 3.2. Predicted centerline sodium vapor temperature. (a) At $z = (L_e + L_a + L_c)/2$, (b) Axial distributions at various times.

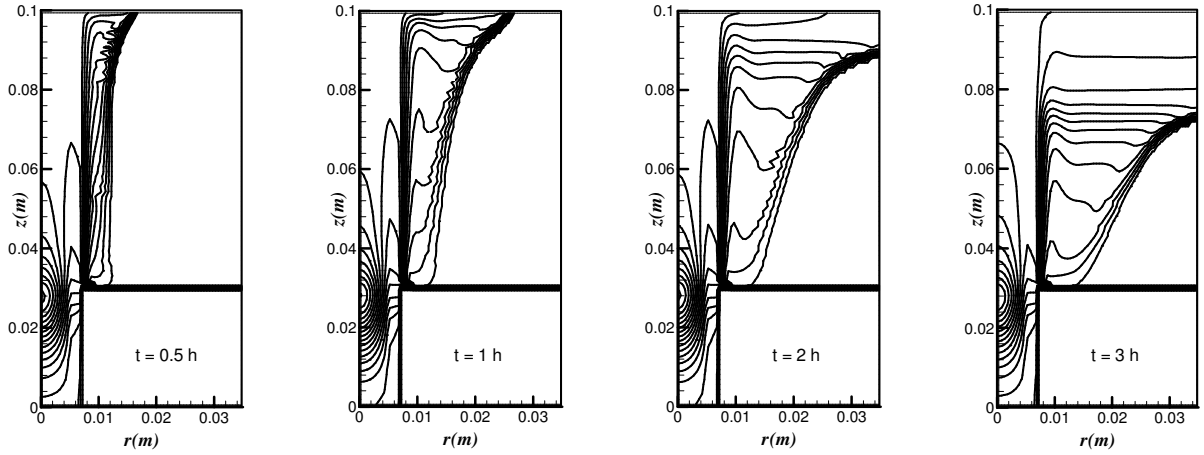

(a) Heat pipe

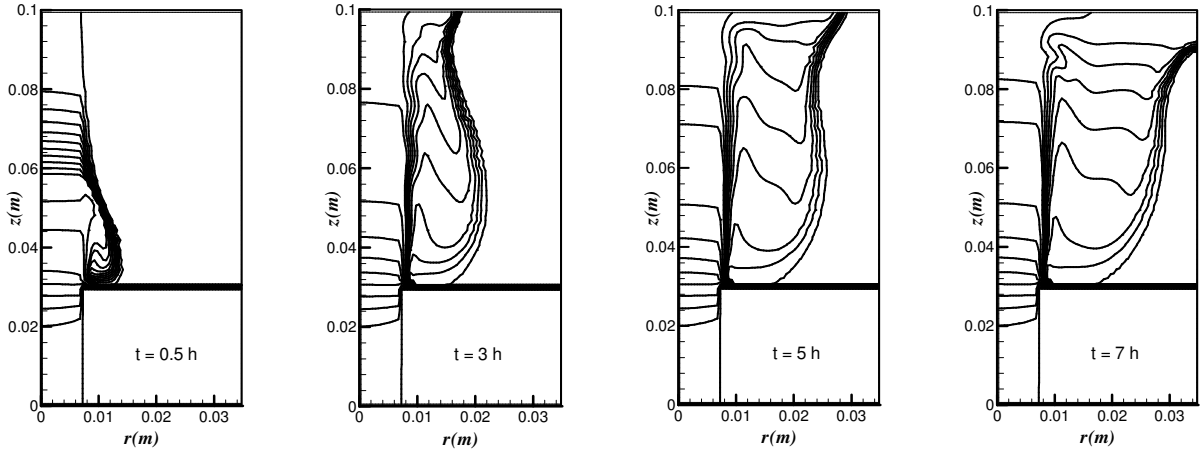

(b) Rod

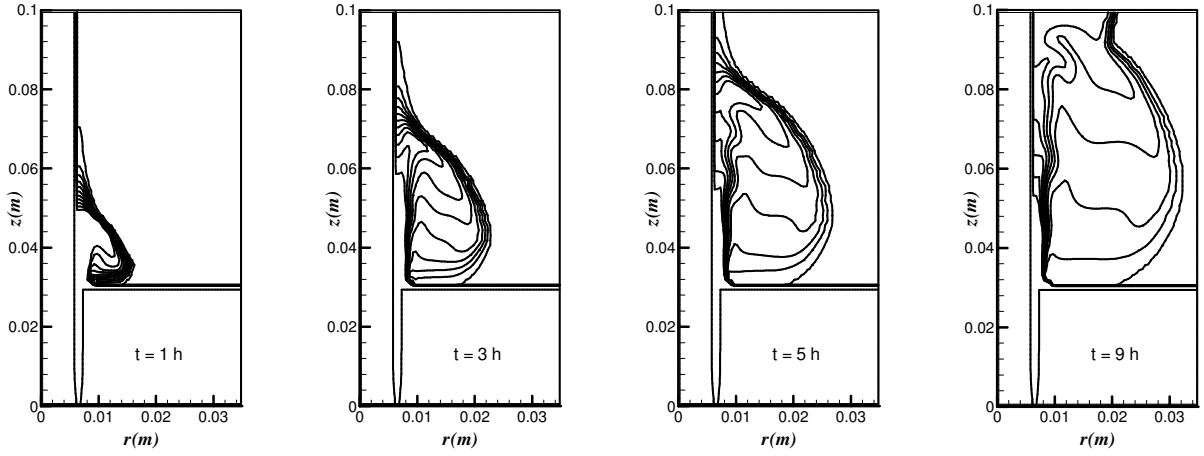

(c) Tube

Fig. 3.3. Temperature distributions for the tall module (L_c = 70 mm, HFB). (a) Heat pipe, (b) Rod, (c) Tube. Isotherms are shown at intervals of 0.2 K (1 K) over the range 580 K $\leq T \leq$ 582 K (582 K < $T \leq$ 591 K) for the rod and tube cases. Isotherms are shown at intervals of 0.5 K for 580 K $\leq T \leq$ 591 K for the heat pipe case.

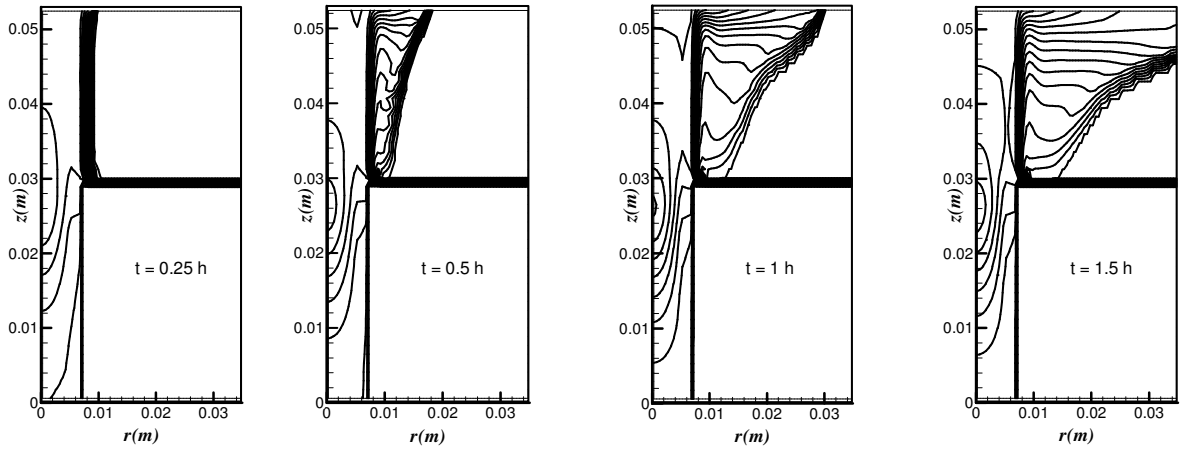

(a) Heat pipe

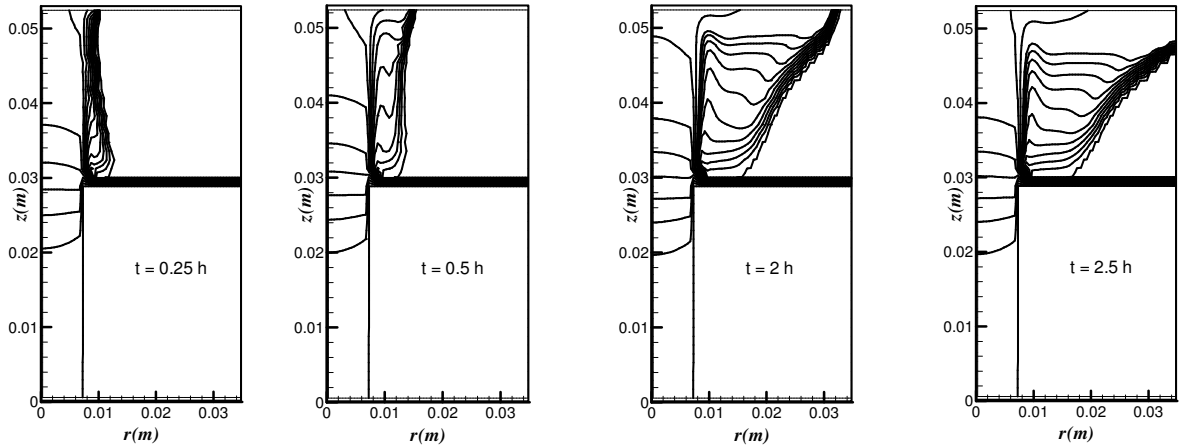

(b) Rod

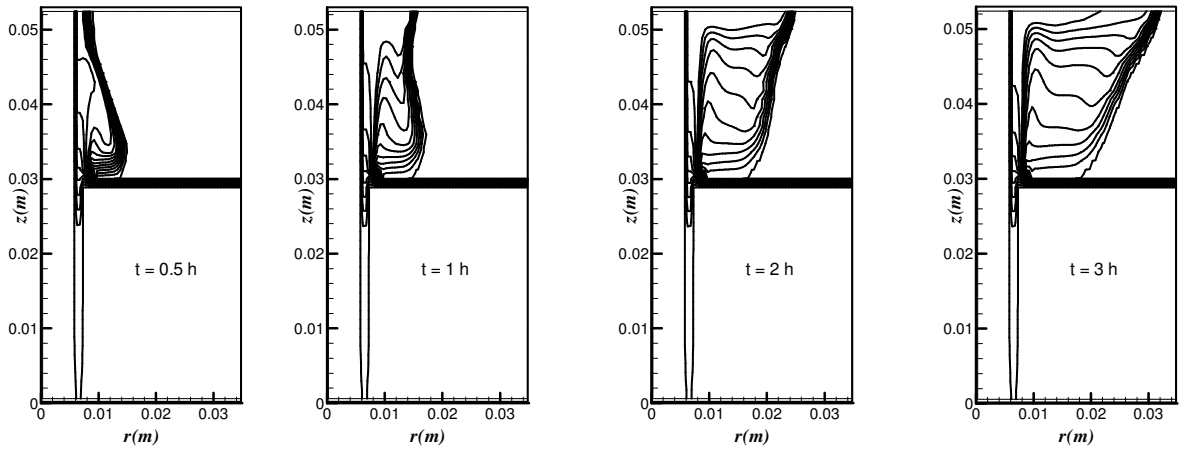

(c) Tube

Fig. 3.4. Temperature distributions for the short module (L_c = 23 mm, HFB). (a) Heat pipe, (b) Rod, (c) Tube. Isotherms are shown at the same intervals as in Fig. 3.3.

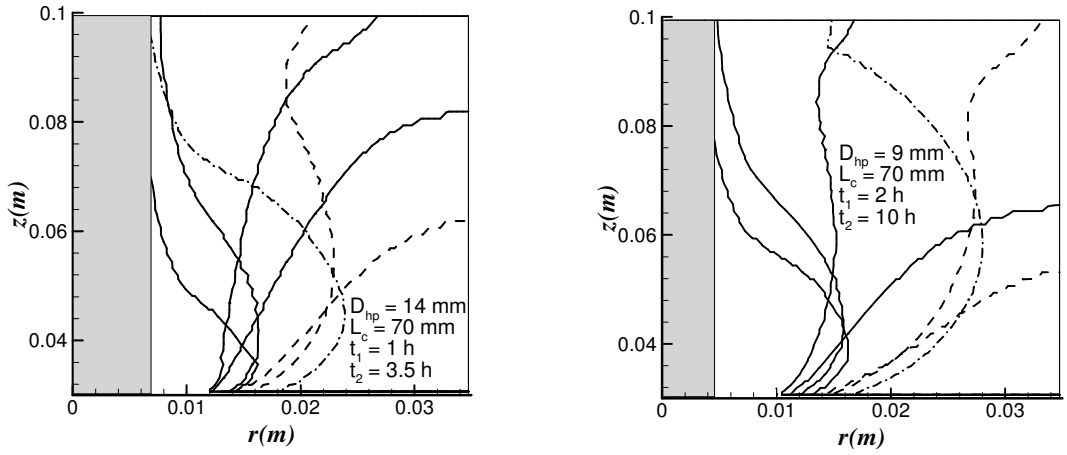

(a)

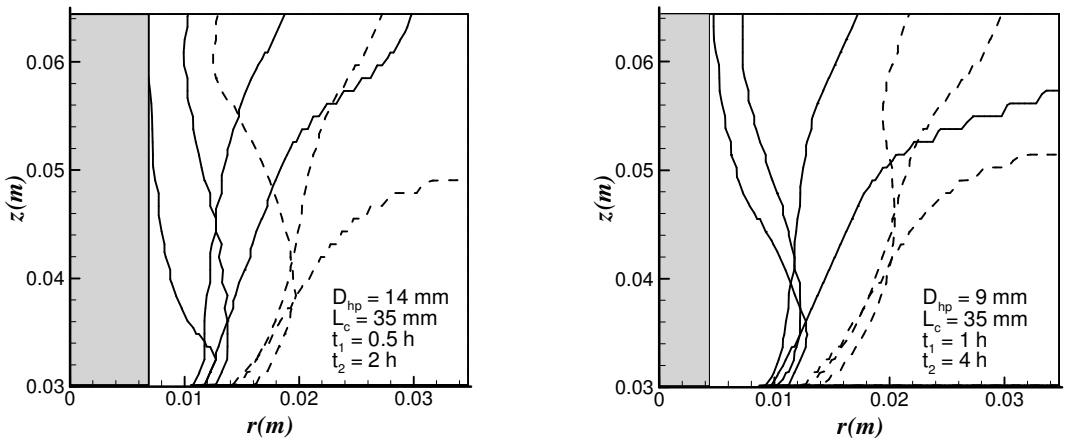

(b)

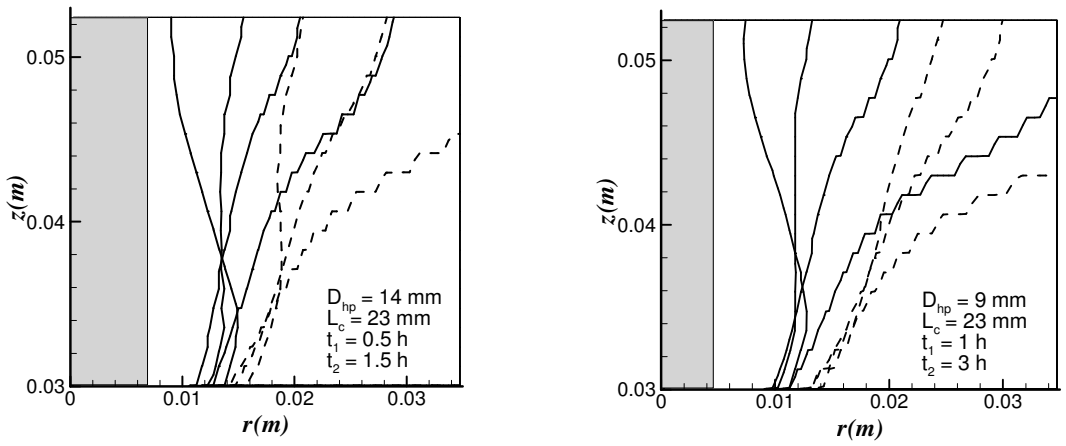

(c)

Fig. 3.5. Solid-liquid interfaces associated with the isothermal surface, heat pipe, rod and tube for HFB at early (t_1, solid lines) and late (t_2, dashed lines) times. Predictions correspond to (a) tall (b) medium and (c) short modules equipped with large diameter (left) and small diameter (right) heating surfaces.

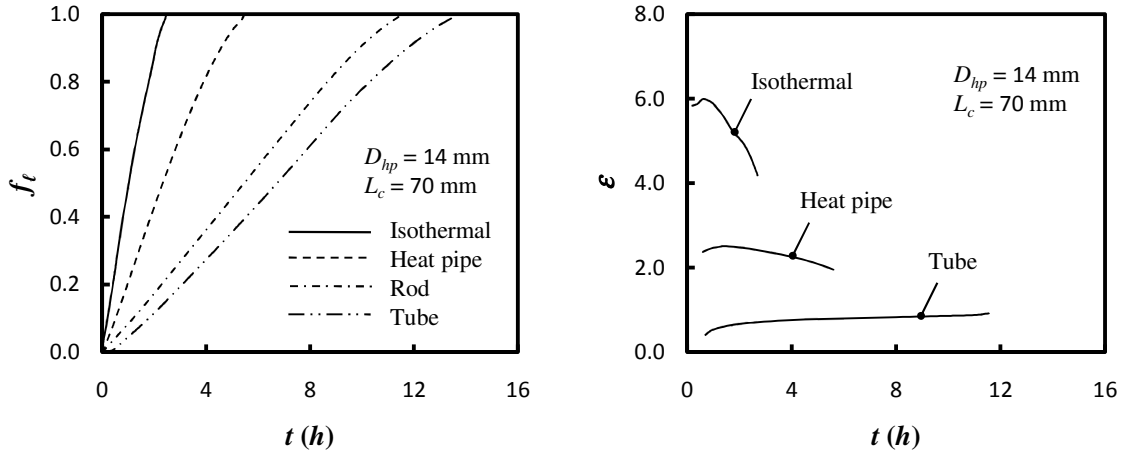

(a)

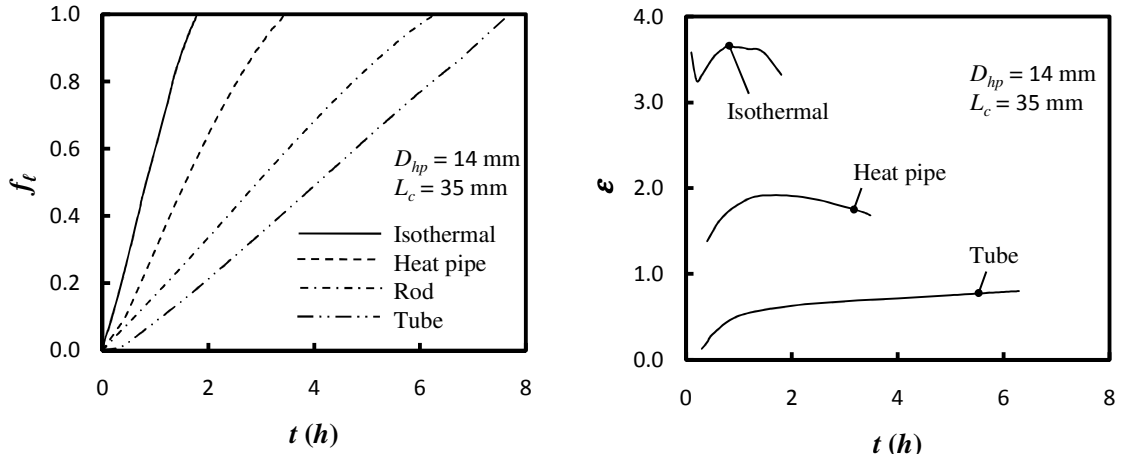

(b)

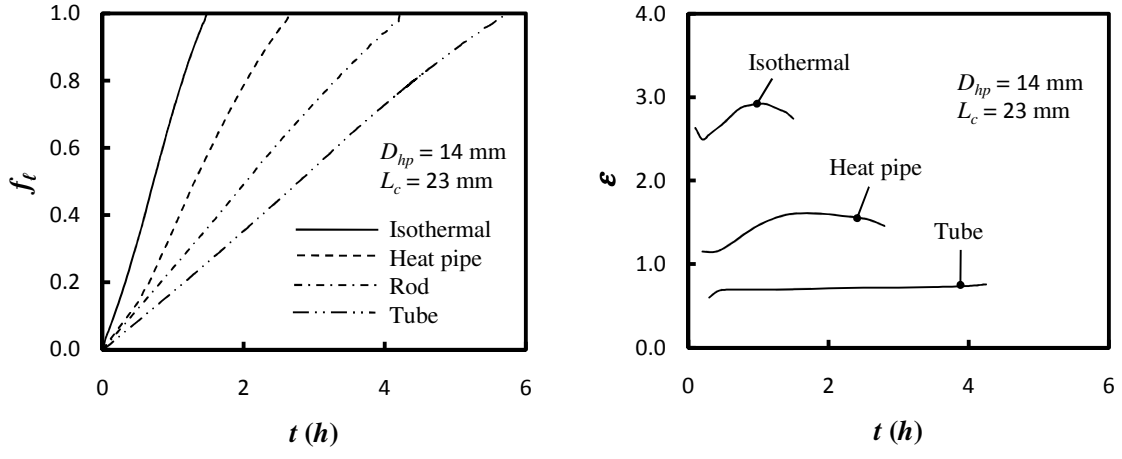

(c)

Fig. 3.6. Liquid fraction histories (left) and effectiveness histories (right), (D_{hp} = 14 mm, HFB). (a) Tall module, (b) Medium module, (c) Short module.

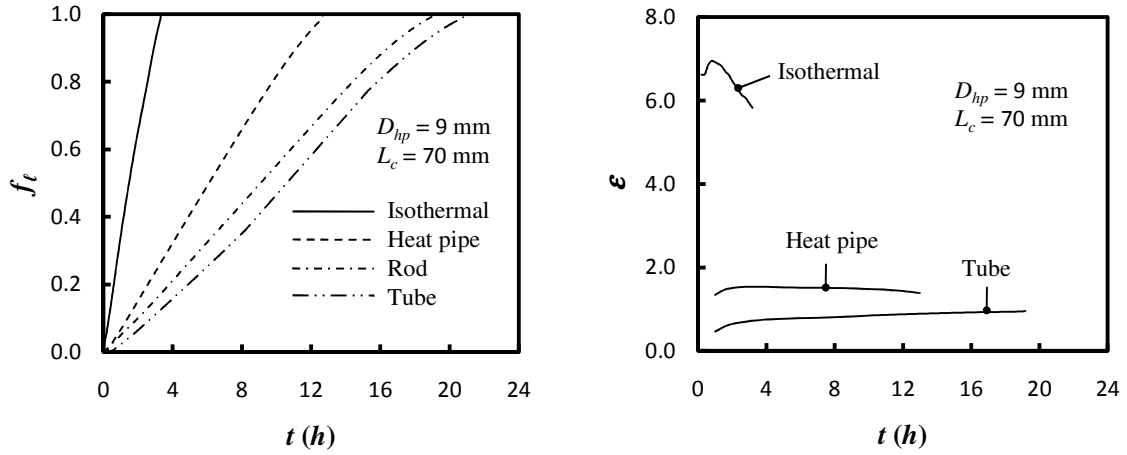

(a)

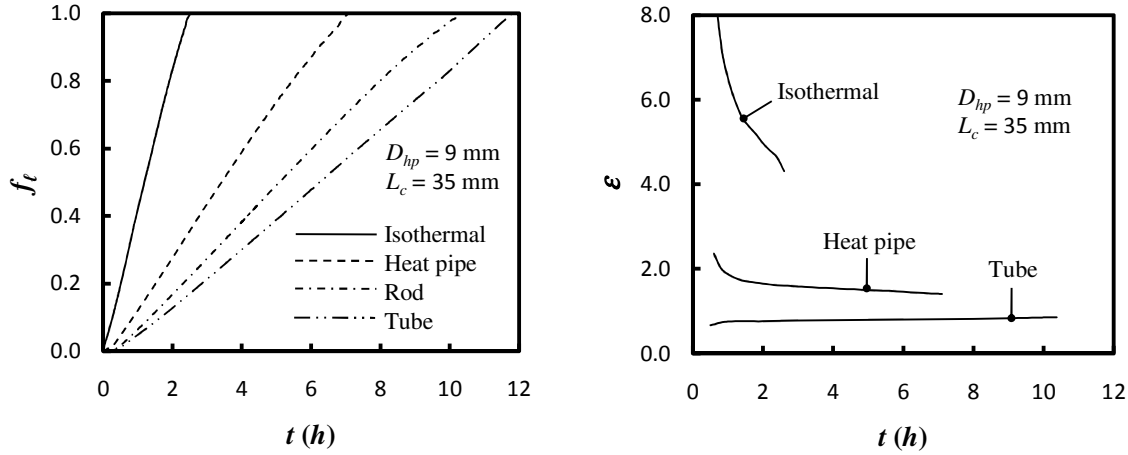

(b)

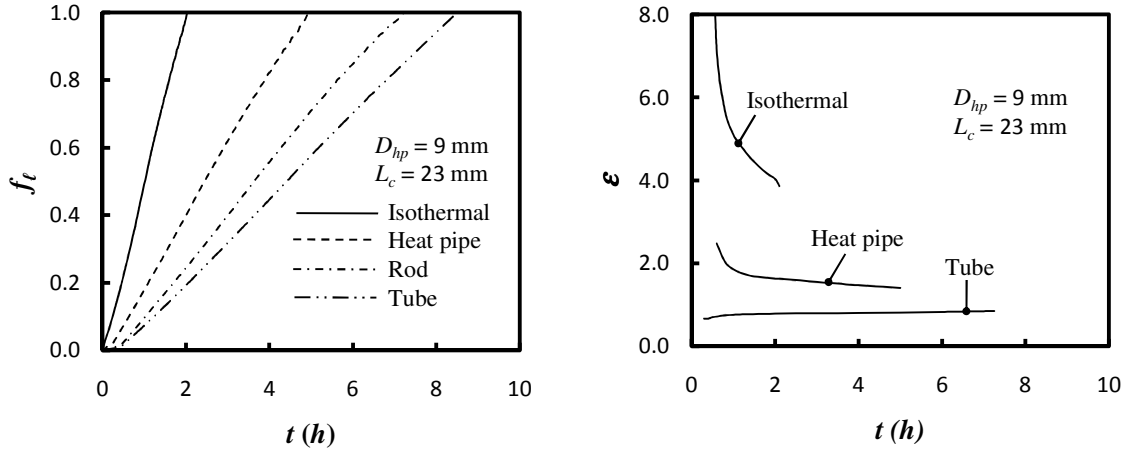

(c)

Fig. 3.7. Liquid fraction histories (left) and effectiveness histories (right), (D_{hp} = 9 mm, HFB). (a) Tall module, (b) Medium module, (c) Short module.

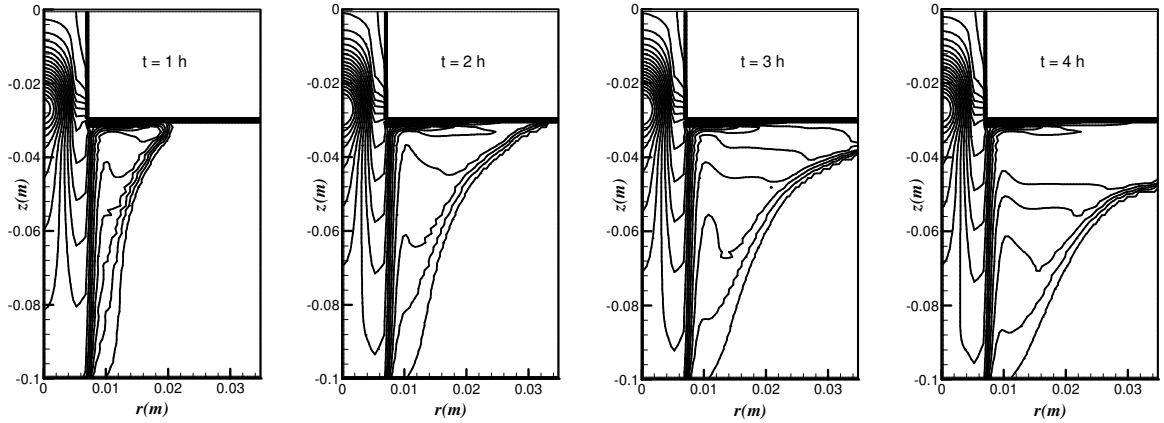

(a) Heat pipe

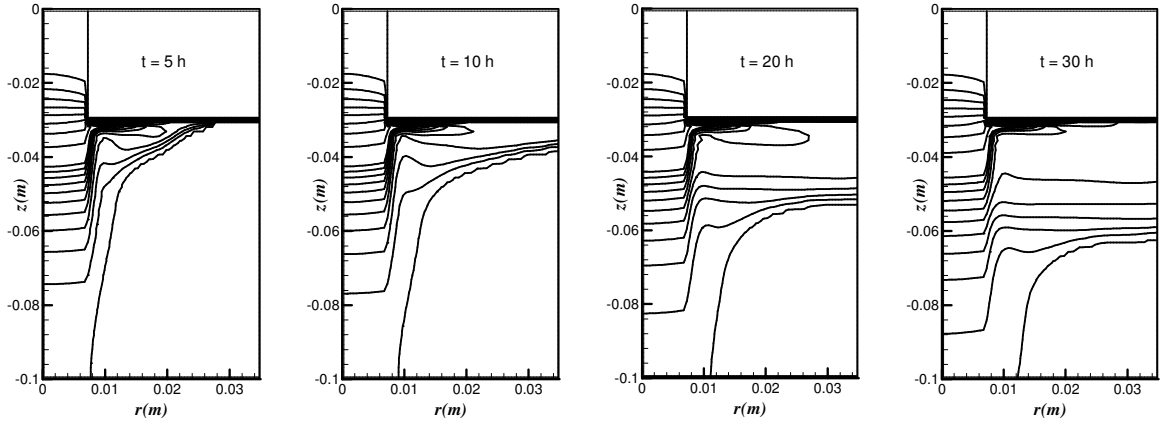

(b) Rod

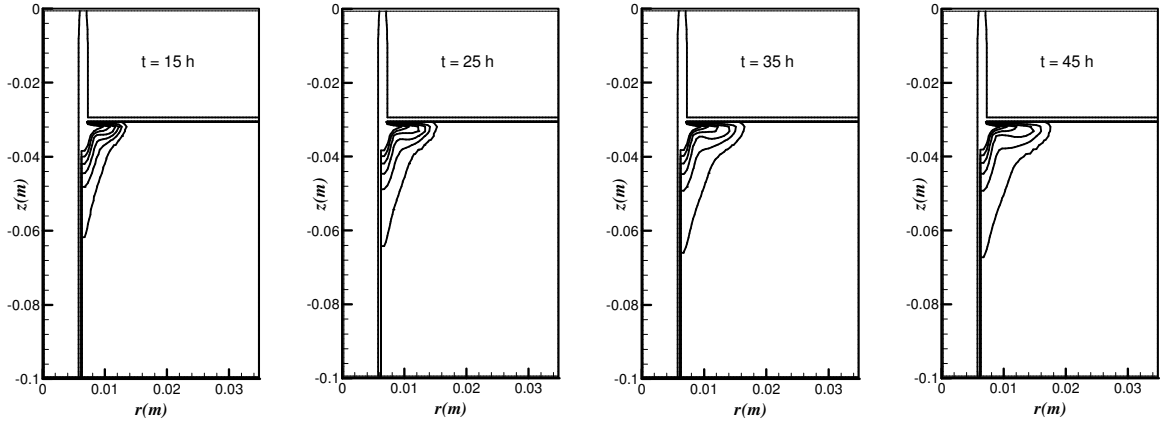

(c) Tube

Fig. 3.8. Temperature distributions for the tall module (L_c = 70 mm, HFA). (a) Heat pipe, (b) Rod, (c) Tube. Isotherms are shown at the same intervals as in Fig. 3.3 for the heat pipe and rod. Isotherms are shown at intervals of 0.2 K for 580 K $\leq T \leq$ 581 K along with one isotherm at 591 K for the tube.

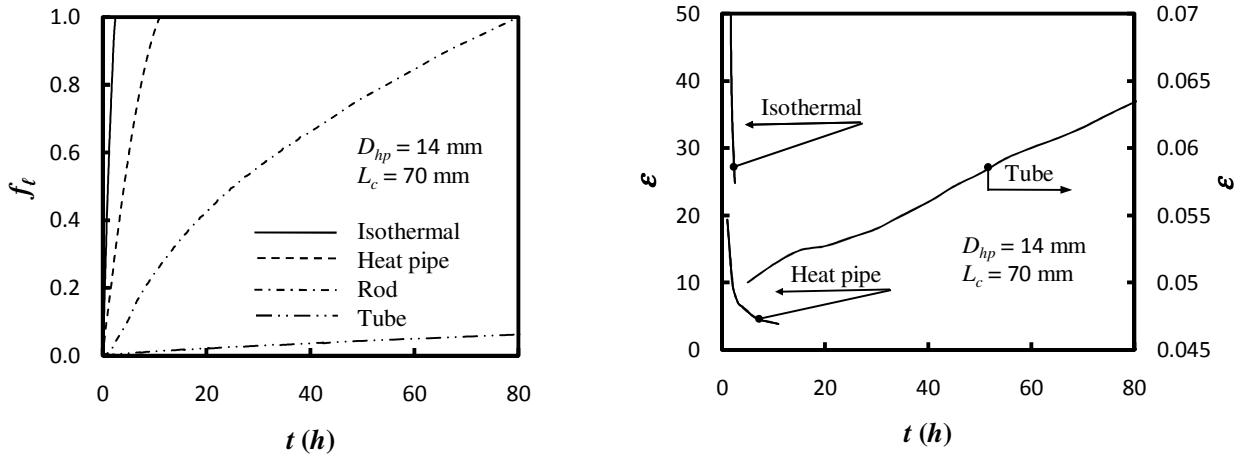

(a) (b)

Fig. 3.9. Liquid fraction histories (left) and effectiveness histories (right), (D_{hp} = 14 mm, L_c = 70 mm, HFA).

References

[1] C.W. Lan, D.T. Yang, Dynamic simulation of the vertical zone-melting crystal growth, International Journal of Heat and Mass Transfer 41 (24) (1998) 4351-4373.

[2] Z. Liu, Z. Wang, C. Ma, An experimental study on heat transfer characteristics of heat pipe heat exchanger with latent heat storage, Part I: Charging only and discharging only modes, Energy Conversion and Management 47 (7-8) (2006) 944-966.

[3] Q. He, W.N. Zhang, A study on latent heat storage exchangers with the high temperature phase-change material, International Journal of Energy Research 25 (4) (2001) 331–41.

[4] H. Cui, Y. Xiugan, X. Hou, Thermal performance analysis for a heat receiver using multiple phase change materials, Applied Thermal Engineering 23 (18) (2003) 2353–2361.

[5] R. Tamme, D. Laing, W.D. Steinmann, Advanced thermal energy storage technology for parabolic trough, Journal of Solar Energy Engineering 126 (2) (2004) 794–800.

[6] H. Michels, R. Pitz-Paal, Cascaded latent heat storage for parabolic trough solar power plants, Solar Energy 81 (6) (2007) 829–837.

[7] H. Cui, X. Yuming, G. Yanshu, W. Zhenhui, C. Haochen, Y. Xiugan, Numerical simulation and experimental investigation on unit heat exchange tube for solar heat receiver, Solar Energy 82 (12) (2008) 1229–1234.

[8] H. Shabgard, T.L. Bergman, N. Sharifi, A. Faghri, High temperature latent heat thermal energy storage using heat pipes, International Journal of Heat and Mass Transfer 53 (15-16) (2010) 2979–2988.

[9] C.W. Robak, T.L. Bergman, A. Faghri, Enhancement of latent heat energy storage using embedded heat pipes, International Journal of Heat and Mass Transfer 54 (15-16) (2011) 3476-3484.

[10] H. Shabgard, C.W. Robak, T.L. Bergman, A. Faghri, Heat transfer and exergy analysis of cascaded latent heat storage with gravity-assisted heat pipes for concentrating solar power applications, Solar Energy 86 (3) 2012 816-830.

[11] A. Faghri, Thermal energy storage heat exchanger, US Patent No. 4976308, 1990.

[12] A. Faghri, Micro heat pipe energy storage system, US Patent No. 5000252, 1991.

[13] A. Faghri, Heat Pipe Science and Technology, Taylor & Francis, Washington, D. C., 1995.

[14] M. Aghvami, A. Faghri, Analysis of flat heat pipes with various heating and cooling configurations, Applied Thermal Engineering 31 (14-15) (2011) 2645-2655.

[15] H. Shabgard, A. Faghri, Performance characteristics of cylindrical heat pipes with multiple heat sources, Applied Thermal Engineering 31(16) (2011) 3410-3419.

[16] T. Kaya, J. Goldak, Three-dimensional numerical analysis of heat and mass transfer in heat pipes, International Journal of Heat and Mass Transfer 43 (8) (2007) 775-785.

[17] J.M. Tournier, M.S. El-Genk, A heat pipe transient analysis model, International Journal of Heat and Mass Transfer 37 (5) (1994a) 753-762.

[18] J.M. Tournier, M.S. El-Genk, Segregated solution technique for simulating the transient operation of heat pipes, Numerical Heat Transfer Part B - Fundamentals 25 (3) (1994b) 331-355.

[19] J.M. Tournier, M.S. El-Genk, Transient analysis of the start-up of a water heat pipe from a frozen state, Numerical Heat Transfer Part A - Applications 28 (4) (1995) 461-486.

[20] J.M. Tournier, M.S. El-Genk, Current capabilities of "HPTAM" for modeling high-temperature heat pipes startup from a frozen state, American Institute of Physics Conference Proceedings 608 (2002) 139-147.

[21] Y. Cao, A. Faghri, Transient two-dimensional compressible analysis for high-temperature heat pipes with pulsed heat input, Numerical Heat Transfer Part A - Applications 18 (4) (1990a) 483-502.

[22] J. Rice, A. Faghri, Analysis of screen wick heat pipes, including capillary dry - out limitations, Journal of Thermophysics and Heat Transfer 21 (3) (2007) 475-486.

[23] C.J. Ho, R. Viskanta, Heat transfer during melting from an isothermal vertical wall, Journal of Heat Transfer 12 (106) (1984) 12-19.

[24] B.W. Webb, R. Viskanta, Natural-convection-dominated melting heat transfer in an inclined rectangular enclosure, International Journal of Heat and Mass Transfer 22 (2) (1986) 183-192.

[25] T.L. Bergman, B.W. Webb, Simulation of pure metal melting with buoyancy and surface tension forces in the liquid phase, International Journal of Heat and Mass Transfer 33 (1) (1990) 139-150.

[26] O. Bertrand, B. Binet, H. Combeau, S. Couturier, Y. Delannoy, D. Gobin, M. Lacroix, P. Le Quere, M. Medale, J. Mencinger, H. Sadat, G. Vieira, Melting driven by natural

convection A comparison exercise: first results, International Journal of Thermal Science 38 (1) (1999) 5-26.

[27] D. Gobin, P. Le Quere, Melting from an isothermal vertical wall: synthesis of a numerical comparison excise, Computer Assisted Mechanics and Engineering Sciences 7 (2000) 289-306.

[28] J. Mencinger, Numerical simulation of melting in two-dimensional cavity using adaptive grid, Journal of Computational Physics 198 (1) (2004) 243-264.

[29] N. Hannoun, V. Alexiades, T.Z. Mai, A reference solution for phase change with convection, International Journal for Numerical Methods in Fluids 48 (11) (2005) 1283-1308.

[30] Y. Cao, A. Faghri, A numerical analysis of phase change problem including natural convection, ASME Journal of Heat Transfer 112 (1990b) 812-815.

[31] S. Wang, A. Faghri, T.L. Bergman, A comprehensive numerical model for melting with natural convection, International Journal of Heat and Mass Transfer 53 (9-10) (2010a) 1986-2000.

[32] S. Wang, A. Faghri, T.L. Bergman, Numerical modeling of alternate melting and solidification, Numerical Heat and Transfer Part B - Fundamentals 58 (6) (2010b) 393-418.

[33] E.M. Sparrow, S.V. Patankar, S. Ramadhyani, Analysis of melting in the presence of natural convection in the melt region, Journal of Heat Transfer 99 (4) (1977) 521-526.

[34] K.A.R. Ismail, C.A. Melo, Convection-based model for a PCM vertical storage unit, International Journal of Energy Research 22 (14) (1998) 1249-1265.

[35] B.J. Jones, D. Sun, S. Krishnan, S.V. Garimella, Experimental and numerical study of melting in a cylinder, International Journal of Heat and Mass Transfer 49 (15-16) (2006) 2724-2738.

[36] Z. Liu, Z. Wang, C. Ma, An experimental study on the heat transfer characteristics of a heat pipe heat exchanger with latent heat storage. Part II: Simultaneous charging/discharging modes, Energy Conversion and Management 47 (7–8) (2006) 967-991.

[37] K. Nithyanandam, R. Pitchumani, Analysis and optimization of a latent thermal energy storage system with embedded heat pipes, International Journal of Heat and Mass Transfer 54 (21–22) 2011 4596-4610.

[38] A. Faghri, Y. Zhang, Transport Phenomena in Multiphase Systems, Academic Press, Elsevier, New York, 2006.

[39] A. Faghri, Y. Zhang, J. Howell, Advanced Heat and Mass Transfer, Global Digital Press, Columbia, Missouri, 2010.

[40] S.V. Patankar, Numerical Heat Transfer and Fluid Flow, McGraw-Hill, New York, 1980.

[41] W.W. Jin, W.Q. Tao, Y.L. He , Z.Y. Li, Analysis of inconsistency of SIMPLE-like algorithms and an entirely consistent update technique-the CUT algorithm, Numerical Heat Transfer Part B - Fundamentals 53(4) (2008) 289-312.

[42] J.H. Ferziger, M. Peric, Computational Methods for Fluid Dynamics, Springer, New York, 1996.

[43] H.L. Stone, Iterative solution of implicit approximation of multidimensional partial differential equations, SIAM Journal on Numerical Analysis 5 (3) (1968) 530-558.

[44] N. Sharifi, T.L. Bergman, A. Faghri, Enhancement of PCM melting in enclosures with horizontally-finned internal surfaces, International Journal of Heat and Mass Transfer 54 (19-20) (2011) 4182-4192.

[45] M.N. Ivanovskii, V.P. Sorokin, I.V. Yagodkin, The physical principles of heat pipes, Oxford University Press, New York, 1982.

[46] W.J. Bowman, Simulated heat pipe vapor dynamics, Ph D thesis, Air Force Institute of Technology, 1987.

[47] A. Faghri, M. Buchko, Experimental and numerical analysis of low-temperature heat pipes with multiple heat sources, ASME Journal of Heat Transfer 113 (3) (1991) 728-734.

[48] P.M. Dussinger, W.G. Anderson, Design and Testing of Titanium/Cesium and Titanium/Potassium Heat Pipes, Proceedings of the Third International Energy Conversion Engineering Conference, San Francisco, California, 2005.

[49] H.S. Goods, R.W. Bradshaw, Corrosion of stainless steels and carbon steel by molten mixtures of commercial nitrate salts, Journal of Materials Engineering and Performance 13 (1) (2004) 78-87.

[50] R.W. Bradshaw, N.P. Siegel, Molten nitrate salt development for thermal energy storage in parabolic trough solar power systems, Proceedings of ES2008 Energy Sustainability, Jacksonville, Florida USA, 2008.

[51] A.A. Attia, A.H. Ali, A.N.A. Masri, A.M. Baraka, Corrosion behavior of stainless steel alloys in molten (Na,K)NO_3 eutectic mixture, Material Science and Engineering Technology 30 (9) (1999) 559-565.

[52] M. Kenisarin, High-temperature phase change materials for thermal energy storage, Renewable and Sustainable Energy Reviews 14 (3) (2010) 955-970.

[53] C. Harley, A. Faghri, Complete transient two-dimensional analysis of two-phase closed thermosyphons including the falling condensate film, Journal of Heat Transfer 116 (2) (1994) 418-426.

[54] T.L. Bergman, A.S. Lavine, F.P. Incropera, D.P. Dewitt, Fundamentals of Heat and Mass Transfer, seventh ed., Wiley, Hoboken, 2011.

Chapter 4. Simulation of heat pipe-assisted latent heat thermal energy storage with simultaneous charging and discharging

Melting and solidification of a phase change material (PCM) held within a vertical cylindrical enclosure that is integrated with a heat pipe (HP) is simulated as a single module. The HP is heated from the bottom to melt (charge) the PCM that is positioned in the middle of the HP length, and is cooled from the top to solidify (discharge) the PCM. Three modes of operation are considered in this study (i) charging-only, (ii) simultaneous charging and discharging, and (iii) discharging-only. All modes of operation are handled with a single HP within a PCM (single HP-PCM) of which the top and bottom sections are inactivated during charging-only and discharging-only modes, respectively. A parametric study of the influence of the PCM enclosure height and input/output heat transfer rates shows that, for the same mass of PCM, a longer enclosure exhibits a lower HP bottom average wall temperature and relatively more PCM melting during simultaneous charging and discharging. Increasing either the input, output, or both heat transfer rates has a significant effect on the temperature of the HP bottom and top sections, but only a minor impact on the temperature of the HP middle section.

4.1. Introduction

Concentrating solar power (CSP) plants harvest solar energy in the form of heat that can be stored in thermal energy storage devices and is ultimately used to produce electricity. The need for energy storage is due to the intermittent availability of solar irradiation and to provide a balance between the supplied loads and the demand (load leveling) during the evening hours when peak utility loads may be present.

Energy can be stored either as sensible heat or latent heat; latent storage is preferred due to its high volumetric energy density and potentially lower cost [1-5]. The temperature of the phase change material (PCM) remains nearly constant during melting (charging) and solidification (discharging) which is desirable. However, the low thermal conductivity of most PCMs limits their use in solar thermal energy generation. To alleviate this challenge, different approaches have been proposed such as dispersing high thermal conductivity particles within the PCM [6,7], using high thermal conductivity porous matrices embedded within the PCM [8,9], micro-encapsulating the PCM [10,11], and incorporating of extended surfaces and / or heat pipes (HPs) [12-19]. HPs are passive devices which utilize liquid-gas phase change to efficiently transfer heat over a long distance with a small cross-sectional area [19]. HPs can be manufactured into a variety of configurations and operational temperature ranges depending on the specific system. When HPs are embedded in the PCM, they can increase the effective thermal conductivity of the PCM significantly. Faghri holds two patents [20, 21] for the incorporation of HPs into PCMs for latent heat thermal energy storage (LHTES) systems. The high volumetric energy density and nearly isothermal behavior of the latent storage is particularly advantageous to dish–Stirling systems due to the isothermal heat input requirement of Stirling engines [22].

Recent investigations have considered various aspects of integrated HP-PCM systems. Liu et al. [23] experimentally investigated a HP-heat exchanger consisting of a circumferentially-finned copper-acetone thermosyphon with stearic acid (T_m = 52.1 ºC) as the PCM. Heating (charging) and cooling (discharging) was induced by water flowing in two separate channels at the bottom and top of the PCM. The effects of the water inlet temperature and mass flow rate were studied. In continuation, Liu et al. [24] used the same experimental setup to investigate simultaneous charging and discharging. Heat was transferred from the hot water stream in the

bottom channel through the HPs to the cold water stream in the top channel. Depending on the operational conditions, the PCM either absorbed or released thermal energy. A criterion based on a thermal resistance analysis was developed to predict whether the PCM absorbs or releases heat.

Robak et al. [25] experimentally investigated separate charging and discharging of n-octadecane housed in a cylindrical enclosure with five embedded HPs. The system was heated and cooled from below with a heat transfer fluid (HTF). The relative performance of the HPs was compared to a fin-assisted case and a non-HP, non-fin case. The results showed that the HP-assisted configuration increased melting and solidification rates compared to the non-fin, and fin-assisted cases.

A thermal network model was developed by Shabgard et al. [26] to simulate separate charging (melting) and discharging (solidification) of a LHTES system for CSP applications. Multiple HPs were installed between the HTF and PCM in two configurations; one with the PCM contained within a tube over which the HTF flowed, and a second with the PCM surrounding a tube that carries HTF. A heat pipe effectiveness, defined as the ratio of heat transfer in the system with HPs to that of a system without HPs, was used to quantify the improvement in heat transfer due to the HPs. In a related work, Shabgard et al. [27] performed a heat transfer and exergy analysis of a large scale, cascaded LHTES system using thermosyphons for CSP. The transient response of the LHTES during either charging and discharging was predicted. The optimum arrangement of HPs in two HP-assisted LHTES configurations was identified by Nithyanandam and Pitchumani [28]. The configurations were (i) a PCM housed inside tubes exposed to a cross flow of HTF, and (ii) a PCM surrounding the HTF tubes.

The two-dimensional transient response of a conjugate HP-PCM system including the effects of natural convection was numerically simulated by Sharifi et al. [29]. A vertically-

oriented HP was concentrically embedded in a PCM held in a cylindrical enclosure. The melting process of the HP-PCM arrangement was compared with melting induced by an isothermal surface, a solid rod, and a hollow tube, all of the same height and outer diameter as the HP. It was shown that the HP significantly enhanced the melting rate compared to that of rods or tubes. It was found that the effectiveness, defined as the volumetric liquid fraction of the HP-PCM relative to the volumetric liquid fraction of the Rod-PCM, of the HP-PCM was doubled compared to the Rod-PCM. It was also shown that the HP-PCM is particularly effective, compared to the Rod-PCM, in increasing the melting rate in a system heated from above.

Recently, it has been suggested that the application of LHTES to dish-Stirling CSP systems may be desirable due to the match between the near isothermal input requirements of Stirling engines and the near isothermal nature of phase change processes [22]. Specifically, Sandia National Laboratories has proposed a LHTES design for dish-Stirling systems that involves multiple dual HP-PCM modules. A dual HP-PCM module is comprised of two HPs, one of which is associated with charging the PCM (encompassing only the hot source and PCM) and the other with discharging the PCM (only the PCM and cold source). The full-scale system, as proposed in [22], consists of multiple dual HP-PCM modules which contain two distinct sets of HPs, where one set is for charging the PCM and the other for discharging the PCM. This configuration leads to a complicated three-dimensional behavior involving distinct as well as simultaneous charging and discharging. A simplified two-dimensional configuration was analyzed by Shabgard et al. [30] to approximate the three-dimensional configuration of [22], based on a physically-reasonable geometric argument. The investigators studied three modes of operation for a typical daily cycle: (i) charging-only, (ii) simultaneous charging and discharging, and (iii) discharging-only. Systems with various geometrical configurations were investigated.

Few HP-PCM studies account for simultaneous charging and discharging, a situation relevant to the Sandia dish-Stirling engine concept. Therefore the objective of this study is to simulate the melting and solidification processes of a PCM induced by a HTF to a single HP for three different modes of operations: Mode I (charging-only), Mode II (concurrent charging and discharging) and Mode III (discharging-only). This work considers an alternative configuration relative to the configuration presented in [30] which may be a more economical and simpler design.

4.2. Physical model and formulations

In this study HP is concentrically positioned in a vertical cylindrical enclosure filled with PCM. The PCM enclosure is situated about the middle section of the HP. The bottom and top sections of the HP are exposed to a specified power or temperature for the different modes of operation. As will become evident, a parametric study is performed to determine the influence of the PCM enclosure height and input/output power.

Figure 4.1 shows the computational domain for the vertically-oriented HP-PCM system. The HP is subdivided into three radial regions: (i) the working fluid vapor, (ii) the porous wick (that is assumed to be saturated with the liquid working fluid), and (iii) the solid wall. The PCM is contained in the cylindrical annulus of length L_M, which surrounds the middle section of the HP. The adiabatic transport sections of the HP are each of length L_a. The HP's bottom and top sections are of length L_B and L_T, respectively.

Three fundamental modes of operation are considered in the modeling enumerated as: Mode I, in which the HP is heated at its bottom section while the HP top section is adiabatic, Mode II, in which the bottom (top) section of the HP is heated (cooled), and Mode III, in which the

bottom section of the HP is adiabatic and the top section of the HP is cooled. Mode I involves charging (melting) -only, Mode II is characterized by simultaneous charging and discharging, while Mode III involves discharging (solidifying) -only. It is noted that the middle section of the HP operates as a condenser in Mode I, a condenser and/or evaporator during Mode II, and an evaporator in Mode III.

Several assumptions are made. All properties are constant except the vapor density of the HP working fluid. The PCM enclosure walls, as well as the top and bottom end caps of the HP, are adiabatic. However, a more practical scenario accounting for heat loss to the ambient is also considered by specifying convection heat losses at the PCM enclosure walls. The pure molten PCM is of the same density as the solid, and the melt is a Boussinesq fluid. Natural convection in the molten PCM is two-dimensional, and laminar. All materials are opaque to thermal radiation, and thermal radiation within the HP is neglected. The vapor phase of the HP working fluid is an ideal gas experiencing two-dimensional laminar compressible flow, and the HP wick is fully saturated with liquid. The HP working fluid at the wick-vapor interface is saturated, and the liquid flow in the wick is neglected [31]. The wick is assumed to be capable of providing adequate capillary pressure to drive the liquid flow through the wick for the operating conditions and different modes presented here.

As is evident, numerous physical boundaries separate the various materials, phases, and components within the conjugate system. Thermal contact resistances are neglected and the system is described with a single computational domain. The computational domain of Fig. 4.1 is therefore subject to the following boundary and initial conditions. Radial gradients of temperature T, pressure p, and velocity component u_z , in addition to the velocity component u_r, are zero at $r = 0$. The heat input (output) to the HP is uniformly applied. Hence, during Mode I q_B

is positive while q_T is zero, during Mode II q_B is positive while q_T is negative, and during Mode III q_B is zero while q_T is negative. The remaining external boundaries are adiabatic and impermeable, and no-slip conditions are specified. The entire domain is initially at the melting temperature of the PCM, which is initially solid.

4.2.1. Phase change material

The thermal response of the PCM is described by the following continuity, momentum and energy equations [32,33]:

$$\frac{\partial u_r}{\partial r}+\frac{u_r}{r}+\frac{\partial u_z}{\partial z}=0 \tag{1}$$

$$\frac{\partial u_r}{\partial t}+u_r\frac{\partial u_r}{\partial r}+u_z\frac{\partial u_r}{\partial z}=-\frac{1}{\rho}\frac{\partial p}{\partial r}+\nu\left(\frac{\partial^2 u_r}{\partial r^2}+\frac{1}{r}\frac{\partial u_r}{\partial r}-\frac{u_r}{r^2}+\frac{\partial^2 u_r}{\partial z^2}\right) \tag{2}$$

$$\frac{\partial u_z}{\partial t}+u_r\frac{\partial u_z}{\partial r}+u_z\frac{\partial u_z}{\partial z}=-\frac{1}{\rho}\frac{\partial p}{\partial z}+\nu\left(\frac{\partial^2 u_z}{\partial r^2}+\frac{1}{r}\frac{\partial u_z}{\partial r}+\frac{\partial^2 u_z}{\partial z^2}\right)+g\left[\beta(T-T_m)-1\right] \tag{3}$$

$$\frac{\partial h}{\partial t}+u_r\frac{\partial h}{\partial r}+u_z\frac{\partial h}{\partial z}=\frac{1}{\rho}\left[\frac{1}{r}\frac{\partial}{\partial r}\left(kr\frac{\partial T}{\partial r}\right)+\frac{\partial}{\partial z}\left(k\frac{\partial T}{\partial z}\right)\right] \tag{4}$$

One may define a scaled temperature as $T^*=T-T_m$ and express the enthalpy by the temperature transforming model [34], resulting in:

$$h=c(T^*+s) \tag{5}$$

where

$$c=\begin{cases} c_s & T^*<-\delta T \\ \dfrac{c_s+c_\ell}{2}+\dfrac{h_{s\ell}}{2\delta T} & -\delta T\le T^*\le\delta T \\ c_\ell & T^*>\delta T \end{cases} \tag{6}$$

$$s=\begin{cases}\delta T & T^{*}<-\delta T \\ \delta T & -\delta T\le T^{*}\le \delta T \\ \dfrac{c_s}{c_\ell}\delta T+\dfrac{h_{s\ell}}{c_\ell} & T^{*}>\delta T\end{cases} \tag{7}$$

Hence, the energy equation can be written as:

$$\frac{\partial(\rho cT^{*})}{\partial t}+u_r\frac{\partial(\rho cT^{*})}{\partial r}+u_z\frac{\partial(\rho cT^{*})}{\partial z}= \frac{1}{r}\frac{\partial}{\partial r}\left(kr\frac{\partial T^{*}}{\partial r}\right)+\frac{\partial}{\partial z}\left(k\frac{\partial T^{*}}{\partial z}\right)-\frac{\partial(\rho cs)}{\partial t}-u_r\frac{\partial(\rho cs)}{\partial r}-u_z\frac{\partial(\rho cs)}{\partial z} \tag{8}$$

where

$$k=\begin{cases}k_s & T^{*}<-\delta T \\ k_s+(k_\ell-k_s)\dfrac{T^{*}+\delta T}{2\delta T} & -\delta T\le T^{*}\le \delta T \\ k_\ell & T^{*}>\delta T\end{cases} \tag{9}$$

4.2.2. Heat pipe

Based on the preceding assumptions, the vapor flow in the HP is described by the continuity equation [19]:

$$\frac{\partial\rho}{\partial t}+\frac{1}{r}\frac{\partial}{\partial r}(\rho ru_r)+\frac{\partial}{\partial z}(\rho u_z)=0 \tag{10}$$

and the *r*- and *z*- momentum equations:

$$\frac{\partial}{\partial t}(\rho u_r)+\frac{1}{r}\frac{\partial}{\partial r}(\rho ru_r^{2})+\frac{\partial}{\partial z}(\rho u_r u_z)=-\frac{\partial p}{\partial r}+\frac{1}{r}\frac{\partial}{\partial r}\left(\mu r\frac{\partial u_r}{\partial r}\right)+\frac{\partial}{\partial z}\left(\mu\frac{\partial u_r}{\partial z}\right)-\frac{\mu u_r}{r^2}+\frac{1}{3}\mu\frac{\partial}{\partial r}\left(\frac{1}{r}\frac{\partial}{\partial r}(ru_r)+\frac{\partial u_z}{\partial z}\right) +\frac{\partial\mu}{\partial r}\left(\frac{\partial u_r}{\partial r}-\frac{2}{3}\left(\frac{1}{r}\frac{\partial}{\partial r}(ru_r)+\frac{\partial u_z}{\partial z}\right)\right)+\frac{\partial\mu}{\partial z}\frac{\partial u_z}{\partial z} \tag{11}$$

$$\frac{\partial}{\partial t}(\rho u_z)+\frac{1}{r}\frac{\partial}{\partial r}(\rho r u_r u_z)+\frac{\partial}{\partial z}(\rho u_z^2)=-\rho g-\frac{\partial p}{\partial z}+\frac{1}{r}\frac{\partial}{\partial r}\left(\mu r\frac{\partial u_z}{\partial r}\right)+\frac{\partial}{\partial z}\left(\mu\frac{\partial u_z}{\partial z}\right)+\frac{1}{3}\mu\frac{\partial}{\partial z}\left(\frac{1}{r}\frac{\partial}{\partial r}(ru_r)+\frac{\partial u_z}{\partial z}\right) \quad (12)$$
$$+\frac{\partial\mu}{\partial z}\left(\frac{\partial u_z}{\partial z}-\frac{2}{3}\left(\frac{1}{r}\frac{\partial}{\partial r}(ru_r)+\frac{\partial u_z}{\partial z}\right)\right)+\frac{\partial\mu}{\partial r}\frac{\partial u_r}{\partial z}$$

The energy equation for the vapor phase of the HP working fluid is:

$$\frac{\partial}{\partial t}(\rho h)+\frac{1}{r}\frac{\partial}{\partial r}(\rho r u_r h)+\frac{\partial}{\partial z}(\rho u_z h)=\frac{Dp}{Dt}+\frac{1}{r}\frac{\partial}{\partial r}\left(kr\frac{\partial T}{\partial r}\right)+\frac{\partial}{\partial z}\left(k\frac{\partial T}{\partial z}\right)+\mu\Phi \quad (13)$$

where the viscous dissipation term is:

$$\Phi=2\left[\left(\frac{\partial u_r}{\partial r}\right)^2+\left(\frac{u_r}{r}\right)^2+\left(\frac{\partial u_z}{\partial z}\right)^2\right]+\left(\frac{\partial u_r}{\partial z}+\frac{\partial u_z}{\partial r}\right)^2-\frac{2}{3}\left[\frac{1}{r}\frac{\partial}{\partial r}(ru_r)+\frac{\partial u_z}{\partial z}\right]^2 \quad (14)$$

Using the ideal gas equation of state and the enthalpy-internal energy relation, the energy equation can be rewritten as:

$$\frac{\partial}{\partial t}(\rho c_v T)+\frac{1}{r}\frac{\partial}{\partial r}(\rho r u_r c_v T)+\frac{\partial}{\partial z}(\rho u_z c_v T)=\frac{1}{r}\frac{\partial}{\partial r}\left(kr\frac{\partial T}{\partial r}\right)+\frac{\partial}{\partial z}\left(k\frac{\partial T}{\partial z}\right)-p\left(\frac{1}{r}\frac{\partial}{\partial r}(ru_r)+\frac{\partial u_z}{\partial z}\right)+\mu\Phi \quad (15)$$

It is assumed that the HP wick is saturated with liquid of negligible velocity, as modeled by Cao and Faghri [31]. Therefore, the heat conduction equation for the wick is:

$$(\rho c_p)_{eff}\frac{\partial T}{\partial t}=k_{eff}\left[\frac{1}{r}\frac{\partial}{\partial r}\left(r\frac{\partial T}{\partial r}\right)+\frac{\partial^2 T}{\partial z^2}\right] \quad (16)$$

The temperature distribution in the solid wall of the HP is governed by:

$$(\rho c_p)_w\frac{\partial T}{\partial t}=k_w\left[\frac{1}{r}\frac{\partial}{\partial r}\left(r\frac{\partial T}{\partial r}\right)+\frac{\partial^2 T}{\partial z^2}\right] \quad (17)$$

The same approach as [29] is used to enforce the saturation condition at the vapor-wick interface for the HP, i.e., the saturation pressure is specified corresponding to the interfacial vapor temperature via the Clausius-Clapeyron equation as described below:

$$P_{v,i} = P_{sat}(T_{v,i}) = P_{ref} \exp\left[\frac{h_{fg}}{R}\left(\frac{1}{T_{ref}} - \frac{1}{T_{v,i}}\right)\right] \quad (18)$$

The interfacial velocity is determined by the mass balance of the vapor control volumes adjacent to the interface where the pressure is specified. Also, the latent heats (interfacial mass flow rate times the HP working fluid latent heat of vaporization) corresponding to the interfacial velocities are applied as source terms in the energy equations for the vapor control volumes adjacent to the interface.

4.3. Numerical procedure

The numerical methodology used here is described in detail elsewhere [29,35] and is summarized as follows. The finite volume approach is used to discretize the governing equations and the central differencing scheme is applied to the advection and diffusion terms [36]. For the time discretization, a fully-implicit scheme, employing a standard underrelaxation version of the consistent update technique [37] or SUV-CUT is used. An explicit update scheme is utilized to evaluate the buoyancy source term in the momentum equation. A pressure-decoupled solid velocity correction is used to ensure zero velocity in the solid PCM, HP wall and wick. The algebraic equations are solved using a multigrid solver [38] with the SIP [39] smoother. Preliminary simulations were performed using grid sizes up to 120 × 120 ($z \times r$). A 100 × 100 grid with a time step of t = 0.1s was found to be sufficient to achieve grid size and time step independent solutions. A convergence criterion (maximum difference between two successive iterations and matrix residuals) of 10^{-5} was specified for all independent variables.

4.4. Results and discussion

The heat pipe considered in this study has a diameter of $D_{hp} = 2r_{hp} = 8$ mm with wall and wick thicknesses of 1 mm each. The wick is a felt metal with a porosity of $\omega = 0.9$. There are two adiabatic transport sections as shown in Fig. 4.1, each of length $L_a = 5$ mm. The HP bottom and top sections are $L_B = L_T = 25$ mm. The HP middle section (or PCM enclosure length) is specified to be $L_M = 20$ mm, 30 mm or 40 mm, therefore the overall HP length changes accordingly. The PCM enclosure inner radius is equal to the HP outer radius ($r_i = r_{hp}$) and to consider a fixed volume of PCM, the enclosure outer radius is $r_{e,o} = 25$ mm, 20.5 mm and 18 mm for $L_M = 20$ mm, 30 mm and 40 mm, respectively. The HP working fluid is sodium and the PCM is a metal (Cu-0.3Si, wt.%). It is noted that stainless steel, which was used as the HP wall and wick, is chemically compatible with the HP working fluid [19] and is also assumed to be compatible with the PCM used in this work. Relevant thermophysical properties are provided in Table 4.1.

4.4.1. Heat transfer behavior

As noted previously, each simulation begins with the PCM in the solid phase and all temperatures at $T_m = 1076$ K. To illustrate the heat transfer behavior of the system, the external vertical surface of the HP in the bottom section is exposed to a constant and uniform heat transfer rate of q_B, while in the top section is exposed to either constant and uniform heat transfer rate ($q_T = - q_B$) or constant and uniform temperature $T_T = 1071$ K ($T_T = T_M - 5$ K). Depending on the operation scheme of the Stirling engine, a constant power output or a constant temperature at the hot interface (HP top section) may be desired. To predict the behavior of the system for each of these operation scenarios, both boundary conditions are considered. Three powers of $q_B = 10$

W, 15 W and 20 W are considered. As mentioned in section 2, three modes of operation are considered here. Mode I ($q_B > 0$, $q_T = 0$) starts at $t = 0$ and ends when the PCM liquid fraction reaches $f_\ell = 0.5$, at which time Mode II ($q_B > 0$, $q_T < 0$) begins. The duration of Mode II is specified to be 1 h. Mode III ($q_B = 0$, $q_T < 0$) starts at the conclusion of Mode II and ends when the PCM is completely solid.

Figure 4.2 shows the isotherms for different modes of operation and values of L_M. The HP top section boundary condition is $q_T = -q_B$ during both Mode II and Mode III. Isotherms are shown at intervals of 0.02 K (1 K) over the range 1076 K $\leq T \leq$ 1076.3 K (1076.5 K $\leq T \leq$ 1094.5 K) for Mode I, and at intervals of 1 K, 0.1 K, 0.02 K and 1 K over the range of 1055 K $\leq T \leq$ 1075 K, 1075 K $\leq T \leq$ 1076 K, 1076 K $\leq T \leq$ 1076.3 K and 1076.5 K $\leq T \leq$ 1094.5 K, respectively for Mode II. Isotherms are shown at intervals of 1 K (0.1 K) over the range 1055 K $\leq T \leq$ 1075 K (1075 K $\leq T \leq$ 1076 K) for Mode III. The isotherms are presented at times corresponding to $f_\ell = 0.5$ (0.4) for Mode II (Mode I and Mode III).

Temperature distributions within the HP in Mode I (Mode III) show that the top (bottom) section of the HP is deactivated while the entire length of the HP is active in Mode II. The temperature distributions of the HP working fluid are influenced by the vapor velocity which can be as high as ≈100 m/s. No sonic limitations were found for the HP considered in this study.

During Mode I a weak clockwise natural convection circulation develops in the melt as it expands. There is a secondary counter-clockwise circulation of the molten PCM adjacent to the HP wall during Mode II. In any case, the temperature distribution in the PCM is only weakly affected by natural convection due to the high thermal conductivity of the PCM. The melting rate is nearly constant (the HP mass varies as L_M changes since the HP overall length changes) for different L_M values since the input/output powers and the PCM mass are the same for all

configurations. Figure 4.3 includes predicted melting with and without natural convection occurred for a typical case. As can be seen, the PCM liquid fraction is not influenced significantly by natural convection.

The time evolution of the solid – liquid interfaces is shown in Fig. 4.4. During Mode I, there is only one solid region while at early times during Mode II, a second solid region develops in the top left of the PCM adjacent to the HP. As time passes, these two solid regions merge with liquid remaining in the middle and bottom portions of the enclosure. As Mode III progresses, the solid-liquid interface advances from the HP outward.

Typical axial distributions of the exterior temperature of the HP are reported in Fig. 4.5 for L_M = 30 mm and q_B = 15 W. For q_T = 0 or -15 W, conditions are shown in Fig. 4.5a at the end of Mode I (t = 3870 s), at the end of Mode II (t = 7470 s), and at an intermediate time during Mode III when f_ℓ = 0.4. At the conclusion of the charging process (t = 3870 s), the maximum temperature exists at z = 0 m, as expected. The temperature adjacent to the PCM is near the PCM melting temperature because of the high thermal conductivity of the phase change material, while the temperature distribution along the non-active (top) section of the HP exhibits slight undulations, reflecting modest localized (and offsetting) condensation and evaporation within the HP. The entire HP length is active during simultaneous charging and discharging (Mode II); with minimum (maximum) HP wall temperatures existing at the top (bottom) of the HP, as expected. During discharge (Mode III), the temperature undulations switch positions to the bottom section of the HP, again reflecting the modest local condensation and evaporation within the HP. Predictions associated with T_T = 1071 K (or q_T = 0) are presented in Fig. 4.5b. Similar axial HP temperatures were noted for all the cases considered here.

Figure 4.6 shows the PCM liquid fraction histories for different input powers with constant L_M = 30 mm. The HP top section is exposed to q_T (q_T = -q_B; Fig. 4.6a) and T_T = 1071 K (Fig. 4.6b). In Mode I, the liquid fraction linearly increases until f_ℓ = 0.5. The time period for Mode II is specified as 1 h as previously mentioned. The total operation time (summation of time duration of each mode) increases as input power decreases. However, this effect is more profound for the case when the HP top boundary condition is q_T (q_T = -q_B) rather than T_T = 1071 K. It is clear that in Fig. 4.6b, the melting process is slightly more dominant than the solidification process during Mode II since the liquid fraction increases with time for q_B = 15W and 20W. However, for q_B = 10W, the melting rate is approximately equal to the solidification rate as seen by the nearly constant liquid fraction throughout Mode II. In reality, providing perfectly adiabatic conditions for the HP bottom section (L_B, evaporator for Mode I) during Mode III may not be practical and some heat loss from the HP bottom section may exist. To study this effect during Mode III, a case with T_B = 1075 K (1 K less than the PCM melting point) was considered. This corresponds to a heat loss of approximately 1W from the HP bottom section. The result in terms of liquid fraction is presented in Fig. 4.6b with the dash-dot-dot line. The liquid fraction trend is similar to the case q_B = 0 during Mode III except the total operation time (or the time corresponding to Mode III) is reduced by approximately 3% compared to the case q_B = 0.

The influence of L_M and q_B on the HP output power is shown in Fig. 4.7. For each case, the temperature of T_T is applied to the outer wall of the HP top section during Mode II and III. The output power, q_T,decreases (increases) as the input power, q_B, decreases during Mode II (Mode III) for each L_M. The output power decreases as L_M increases. During Mode II, as L_M increases, relatively more heat is transferred to the PCM rather than directly to the top section since the heat transfer area between the HP and the PCM increases. This leads to a reduction in the HP

middle section average wall temperature which results in a lower output heat transfer rate during Mode III. Overall, the duration of each q_T is larger for higher q_B.

4.4.2. Time-varying heat input

Rather than a constant input heat transfer rate, a variable input heat transfer rate may also play an important role from a practical point of view, especially in solar applications. The input solar heat transfer rate is calculated based upon hourly direct normal irradiance (DNI) data provided by NREL (National Renewable Energy Laboratory). To calculate the instantaneous input heat transfer rate to the PCM in an LHTES system, DNI data for Albuquerque, New Mexico during the month of June 2010 was employed [30]. A dish diameter of 11m and a combined dish optical efficiency and receiver efficiency of 0.93 were specified for the full-scale system. The resulting hourly DNI values are shown in Fig. 4.8a. Since the present analysis is limited to the laminar natural convection regime within the melt, the PCM enclosure was scaled down to prevent the establishment of turbulent flow. This practice also helps to reduce the number of computational cells in the simulations and consequently CPU time. The input heat transfer rate for the scaled down system was determined by multiplying the input heat transfer rate of the full-scale system by a scaling factor based on PCM volume. The instantaneous input heat transfer rate for the small-scale system is shown in Fig. 4.8b as q_{B1}. A second order polynomial ($\approx -0.043\times t^2+0.72\times t$) is curve fit to the actual data for q_{B1} in order to utilize a more computationally simple input heat transfer data for use in the modeling.

In the simulation to follow, the heat loss from the PCM enclosure to the environment is also considered. A convective boundary condition is applied to the PCM enclosure (bottom, top, and lateral surfaces). The ambient temperature is specified to be 300 K and an overall heat transfer

coefficient of 0.8 W/m^2·K is assumed to account for both external convection and insulation. The HP top thermal boundary condition was assumed to be T_T = 1074 K, in which the output heat transfer rate is approximately 70% of the input heat transfer rate [22]. The corresponding PCM liquid fraction is presented in Fig. 4.9 for all three modes. Mode I begins at t = 0 h until f_ℓ = 0.5. Mode II occurs from f_ℓ = 0.5 until q_{B1} = 0 W. Mode III (q_{B1} = 0, q_T < 0) starts at the conclusion of Mode II and ends when the PCM is completely solid. During Mode III, Fig. 4.9 shows that the PCM storage serves approximately 7 h of energy delivery in the absence of an input heat transfer rate. Therefore, when the system PCM volume is increased to the full-scale value, the time duration for energy delivery is expected to be approximately 7 h. This time duration is an acceptable value for a typical solar LHTES system [22].

4.5. Conclusions

A numerical model has been developed to simulate conjugate heat transfer involving a vertically-oriented single HP integrated with a PCM. Three modes of operation including (i) charging-only, (ii) simultaneous charging and discharging and (iii) discharging-only were considered.

Melting and solidification rates are governed by conjugate heat transfer effects including conduction in the HP wick and wall, vaporization and condensation of the compressible HP working fluid, and conduction (natural convection) in the solid (molten) PCM which has an evolving topography. Parametric studies show that for the same mass of PCM, a larger enclosure aspect ratio (height to diameter of the PCM enclosure) exhibits a lower average HP bottom wall temperature and promotes more melting during simultaneous charging and discharging due to a

combination of a greater heat transfer area and less conduction distance in the PCM for the smaller diameter of the PCM.

The single HP-PCM module configuration can be utilized for LHTES systems involving either sequential or simultaneous melting and solidification. Single set HP-PCM systems (consisting of multiple single HP-PCM modules) can potentially be more economical and simpler in design compared to alternative configurations such as dual set HP-PCM systems [30]. In order for the system to economically achieve its highest performance, the ratio of the volume occupied by the HPs within the PCM to the total volume of the storage system (PCM as well as HP volume) must be optimized in future work.

Nomenclature

c	specific heat (J/kg·K)
c_p	specific heat at constant pressure (J/kg·K)
c_v	specific heat at constant volume (J/kg·K)
D	diameter (m)
f_ℓ	volumetric PCM liquid fraction
g	gravitational acceleration (m/s^2)
h	enthalpy (J/kg)
h_{fg}	latent heat of evaporation (kJ/kg)
$h_{s\ell}$	latent heat of fusion (kJ/kg)
k	thermal conductivity (W/m·K)
L_a	HP adiabatic section length (m)
L_B	HP bottom section length (m)
L_M	HP middle section length (m)
L_T	HP top section length (m)
p	pressure (Pa)
q	heat transfer rate (W)
r,z	coordinate directions (m)
R	gas constant (J/kg·K)
s	source term in the temperature transforming model
t	time (s or h)
T	temperature (K)
T_m	melting temperature (K)
u	velocity component (m/s)

Greek

β	thermal expansion coefficient (K^{-1})
δT	half width of temperature range (K)
Φ	viscous dissipation (J/kg·m^2)

μ	dynamic viscosity (Pa·s)
ν	kinematic viscosity (m^2/s)
ρ	density (kg/m^3)

Subscripts

B	bottom
e	enclosure
eff	effective
hp	heat pipe
i	wick-vapor interface, inner
ℓ	liquid phase of PCM
o	outer
r,z	coordinate directions
ref	reference
s	solid phase of PCM
sat	saturation
T	top
v	vapor phase of heat pipe working fluid
w	wall of the heat pipe

Table 4.1. Thermophysical properties of components at T_m = 1076K.

	PCM	HP working fluid [19]	HP wall and wick [40]
Material	Cu-0.3Si	Sodium	Stainless steel
Density, ρ (kg/m^3)	5670[a]	760.2 (liquid)	7900
Thermal conductivity, k (W/m K)	300 [22]	53.16 (liquid) 0.0482 (vapor)	19.8
Specific heat, c_p (J/kg K)	597[a]	1267.415 (liquid) 265.2 (vapor)	557
Viscosity, μ (Pa s)	5×10^{-3} [a]	2.349×10^{-5} (vapor)	
Latent heat, h_{sl} or h_{fg} (kJ/kg)	721.3[a]	395.1	
Melting point, T_m (K)	1076 [22]		
Vapor pressure, p_{sat} (Pa)		4352	
Thermal expansion coefficient, β (K^{-1})	13.15×10^{-6} [a]		

[a] Estimated values based on the weighted average of Cu and Si properties provided in [41-45]

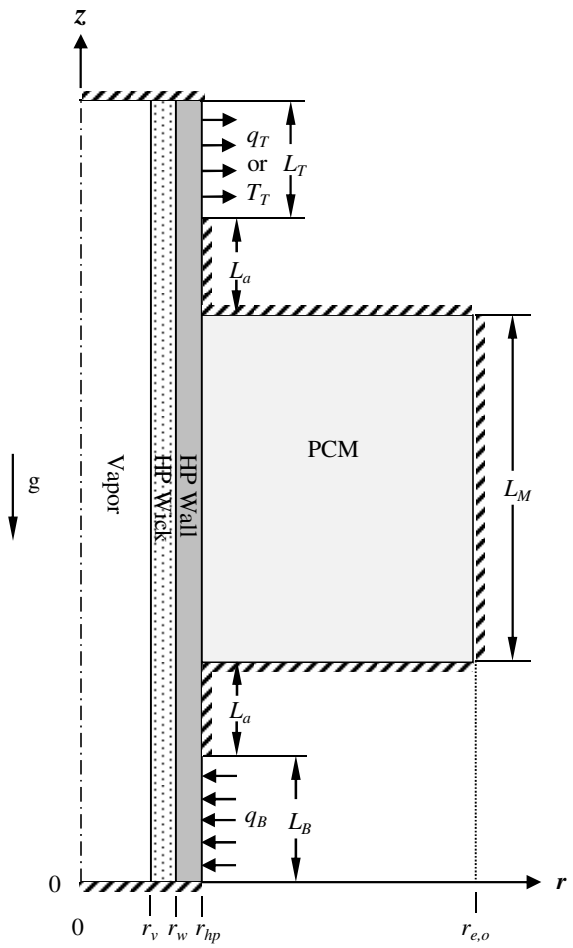

Fig.4.1 Physical model and computational domain for the HP and PCM.

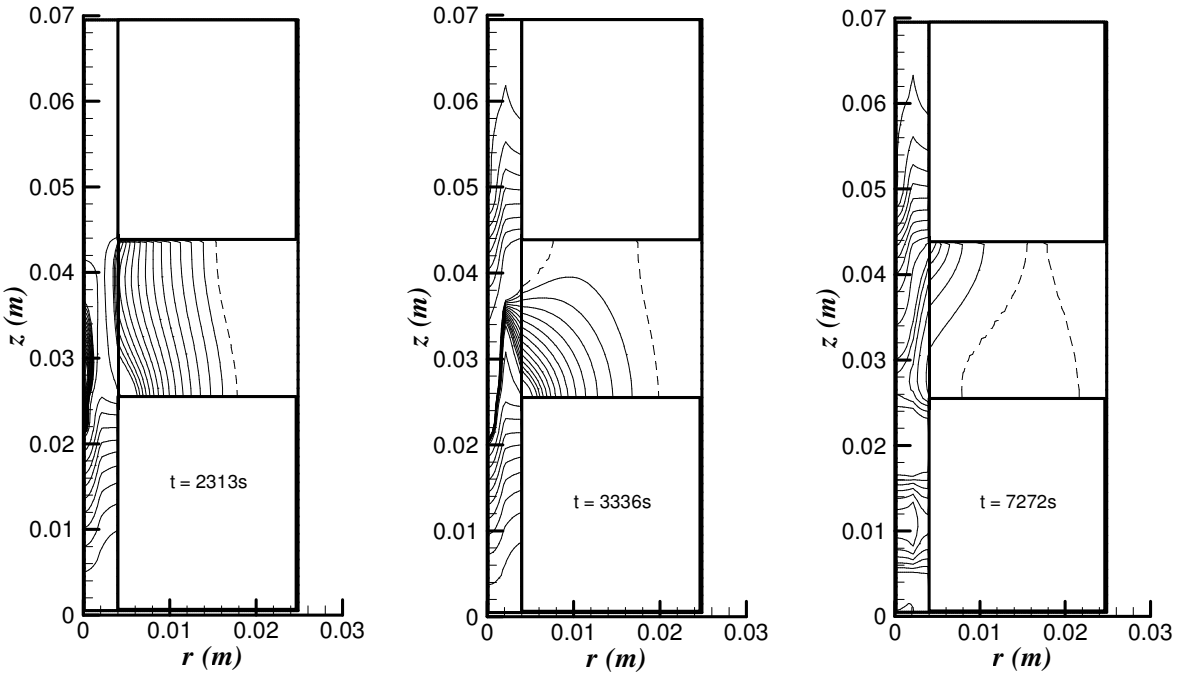

(a) L_M = 20 mm

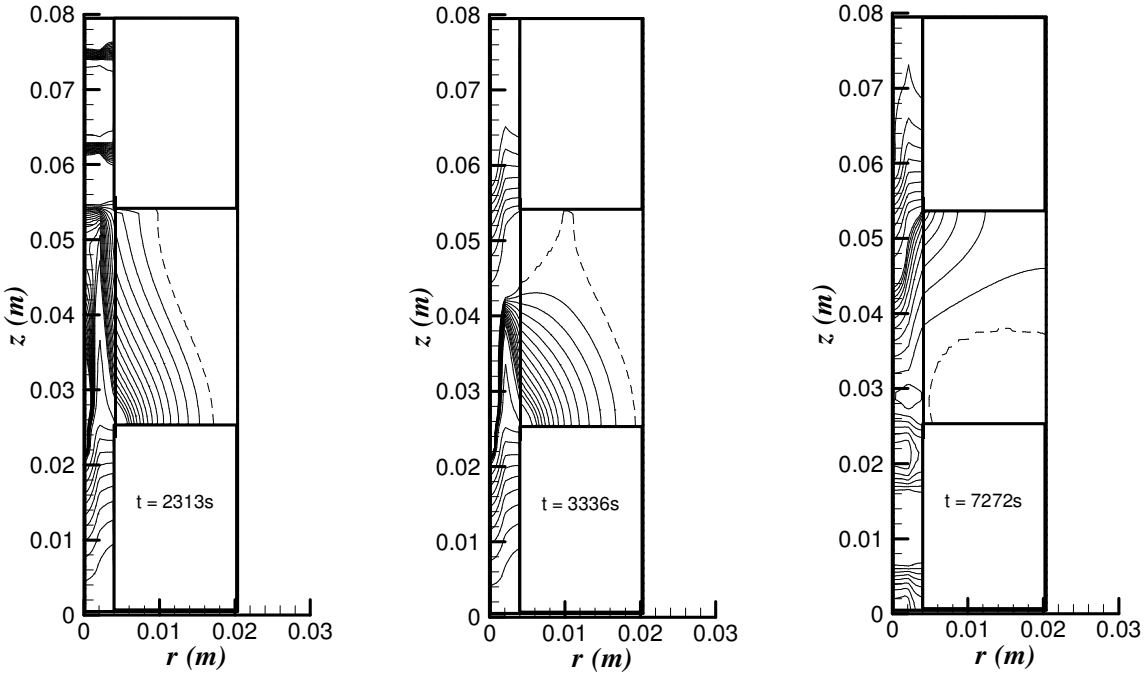

(b) L_M = 30 mm

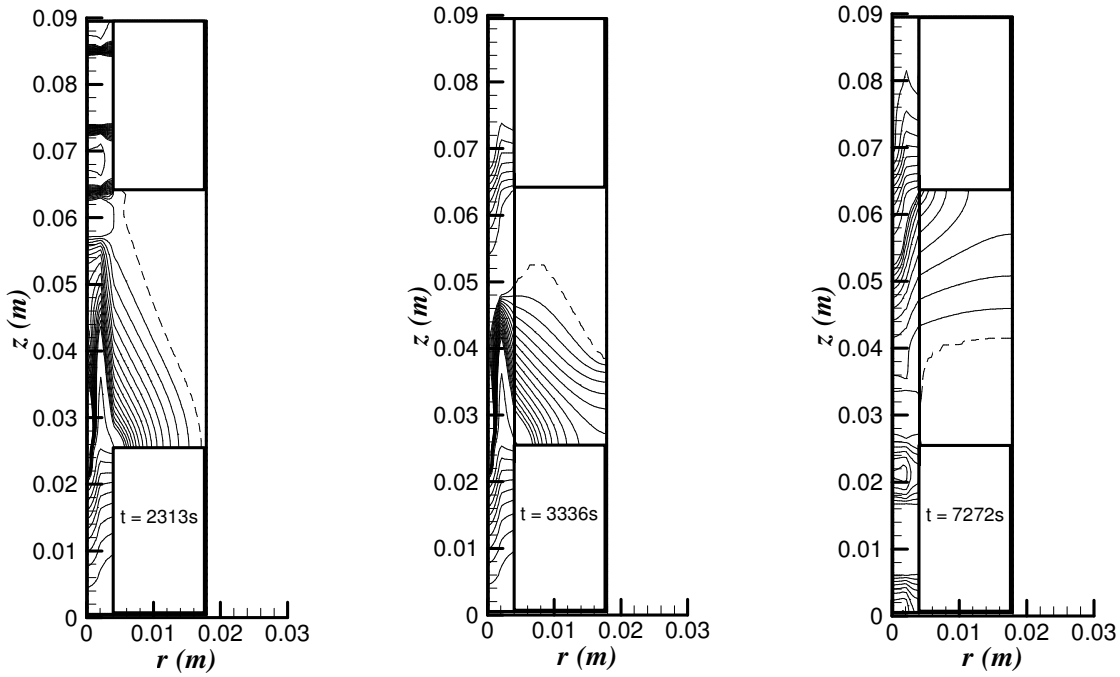

(c) L_M = 40 mm

Fig. 4.2. Temperature distributions of HP-PCM corresponding to Mode I (left), Mode II (middle) and Mode III (right) (q_B = 20W, q_T = -20 W). (a) L_M = 20 mm, (b) L_M = 30 mm, (c) L_M = 40 mm. Solid–liquid interfaces are shown as dashed lines.

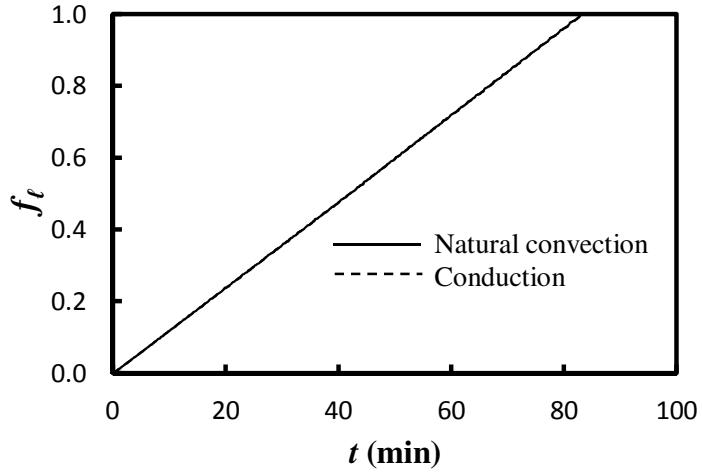

Fig. 4.3. Liquid fraction histories for complete melting corresponding to q_B = 20 W, q_T = 0 and L_M = 40 mm both with and without natural convection.

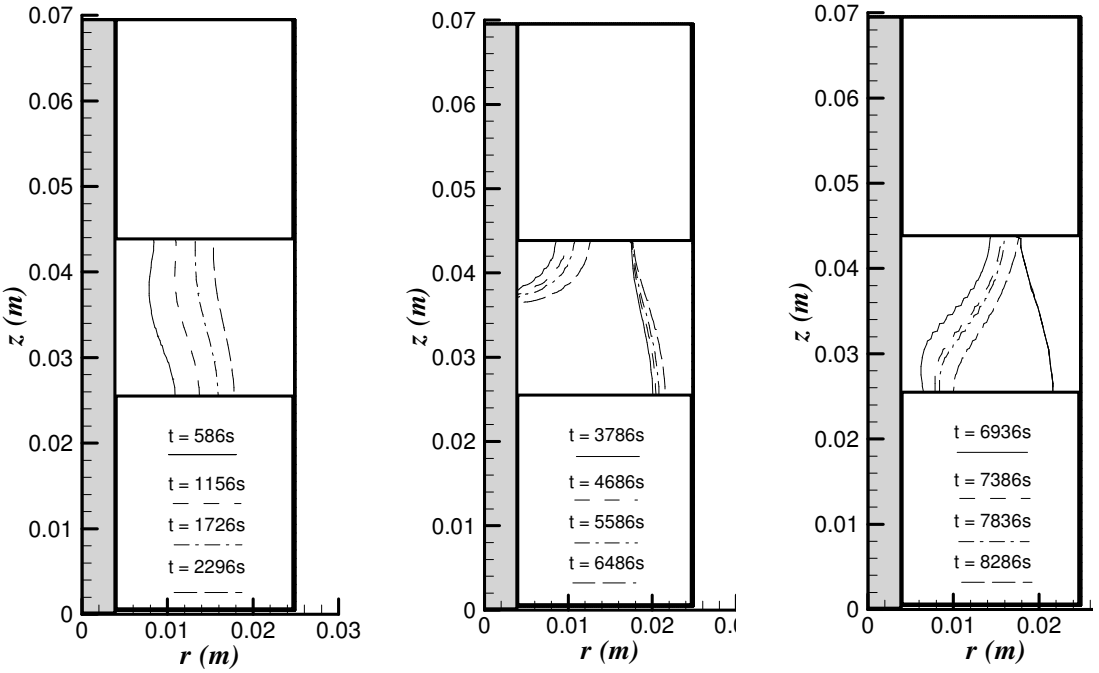

(a) L_M = 20 mm

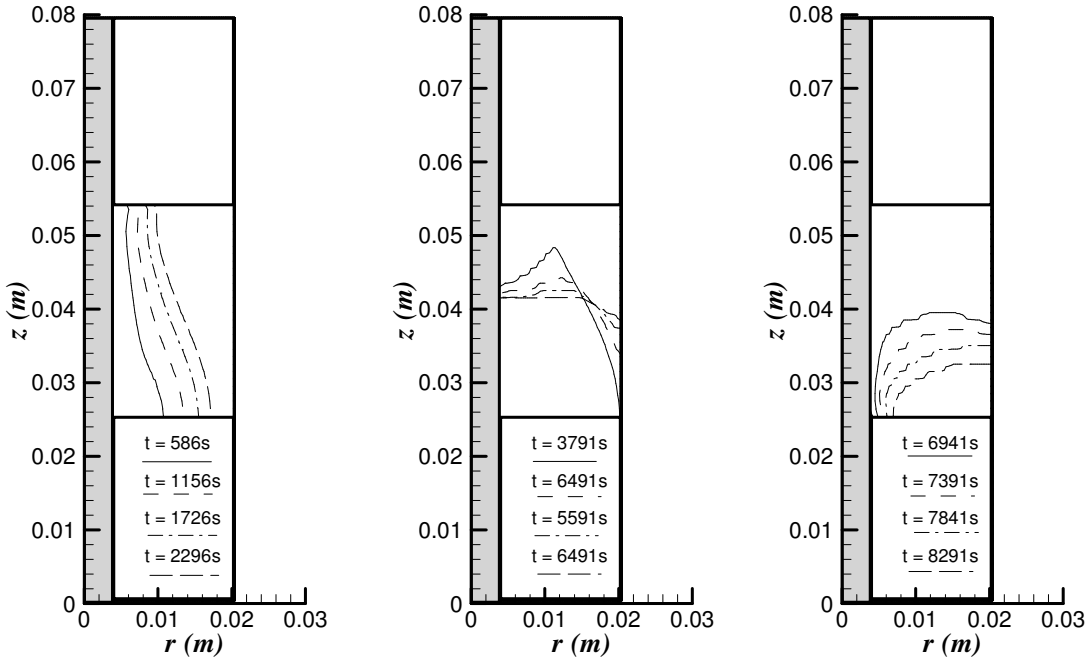

(b) L_M = 30 mm

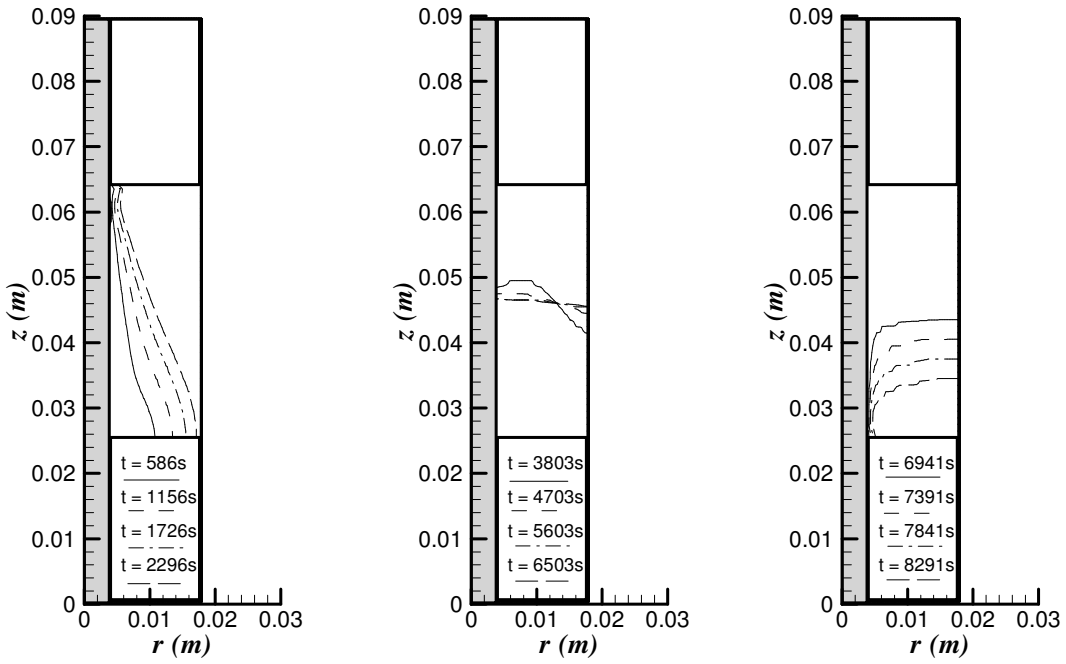

(c) L_M = 40 mm

Fig. 4.4. Solid – liquid interfaces at different times corresponding to Mode I (left), Mode II (middle) and Mode III (right) (q_B = 20W, q_T = -20 W). (a) L_M = 20 mm, (b) L_M = 30 mm, (c) L_M = 40 mm.

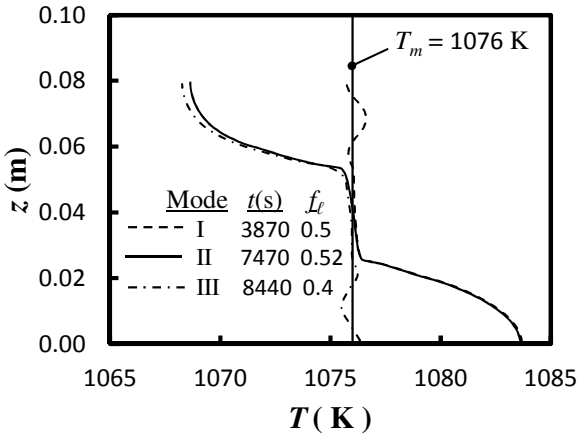

(a)

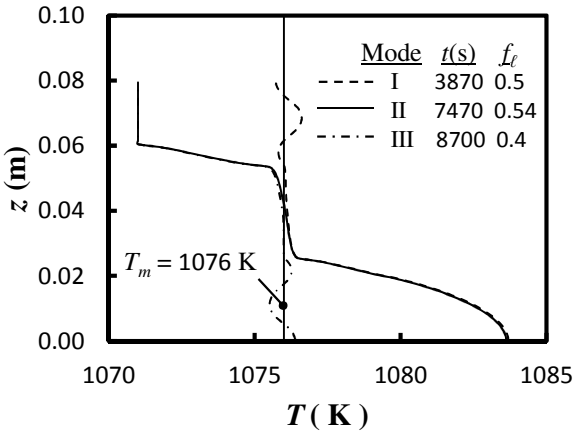

(b)

Fig. 4.5. HP axial temperature distributions for L_M = 30 mm and q_B = 15 W, (a) q_T = 0 or -15 W, (b) q_T = 0 or T_T = 1071 K.

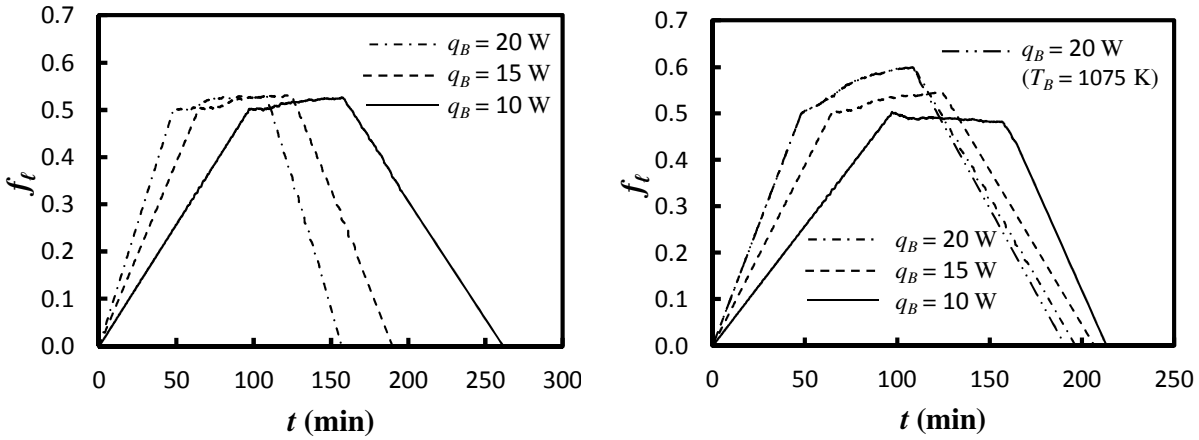

Fig. 4.6. Liquid fraction histories for Mode I+II+III corresponding to L_M = 30 mm. (a) q_T = - q_B , (b) T_T = 1071 K.

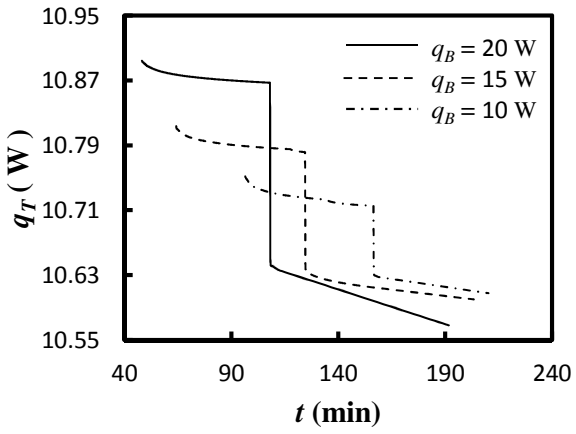

(a) L_M = 20 mm

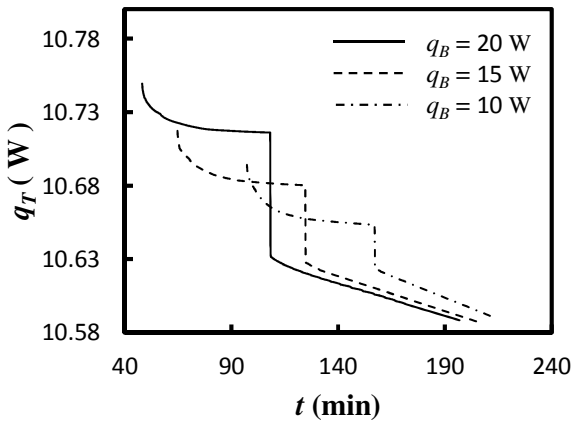

(b) L_M = 30 mm

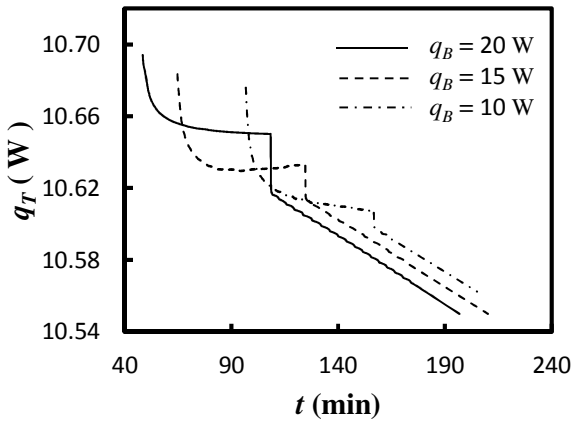

(c) L_M = 40 mm

Fig. 4.7. HP top section output power histories for different q_B (T_T = 1071 K, Mode II and Mode III). (a) L_M = 20 mm, (b) L_M = 30 mm, (c) L_M = 40 mm.

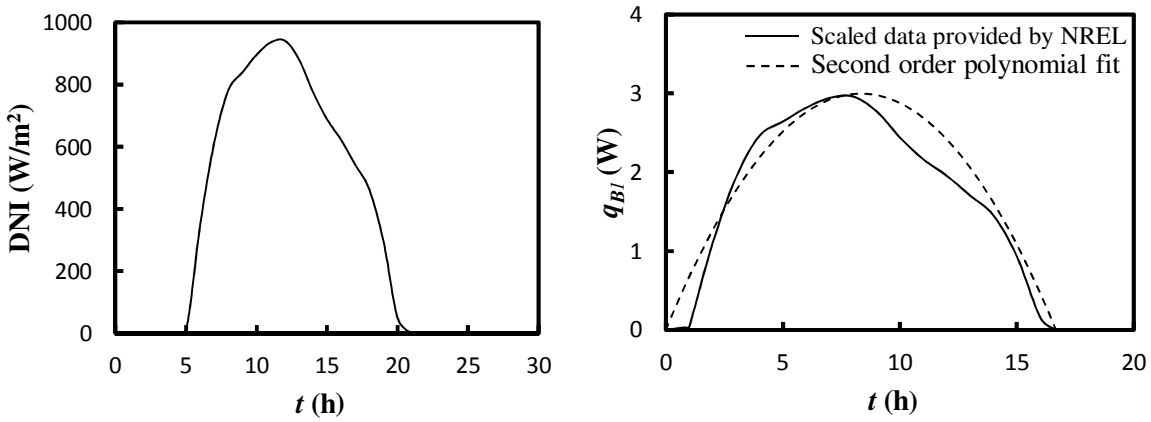

(a) (b)

Fig. 4.8. Average hourly DNI during June 2010 for Albuquerque, New Mexico. (a) DNI provided by NREL [46], (b) scaled input heat transfer rate.

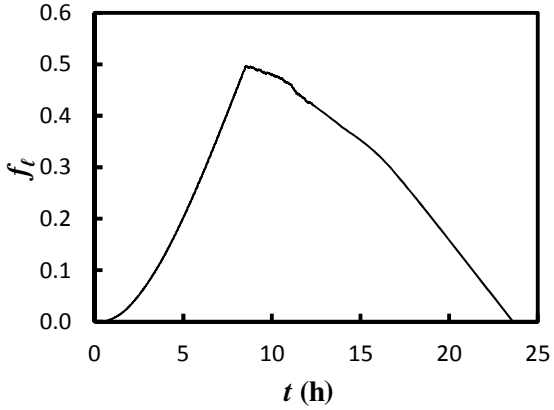

Fig. 4.9. Liquid fraction histories for Mode I+II+III corresponding to input heat transfer rate q_{B1} and T_T = 1074 K (L_M = 20 mm).

References

[1] B. Zalba, J.M. Marin, L.F. Cabeza, H. Mehling, Review on thermal energy storage with phase change: materials, heat transfer analysis and applications, Applied Thermal Engineering 23 (3) (2003) 251–283.

[2] M.M. Farid, A.M. Khudhair, S.A.K. Razack, S. Al-Hallaj, A review on phase change energy storage: materials and applications, Energy Conversion Management 45 (9–10) (2004) 1597–1615.

[3] S.D. Sharma, K. Sagara, Latent heat storage materials and systems: a review, International Journal of Green Energy 2 (1) (2005) 1–56.

[4] F. Agyenim, N. Hewitt, P. Eames, M. Smyth, A review of materials, heat transfer and phase change problem formulation for latent heat thermal energy storage systems (LHTESS), Renewable and Sustainable Energy Reviews 14 (2) (2010) 615–628.

[5] C.W. Lan, D.T. Yang, Dynamic simulation of the vertical zone-melting crystal growth, International Journal of Heat and Mass Transfer 41 (24) (1998) 4351-4373.

[6] S. Jegadheeswaran, S.D. Pohekar, Energy and exergy analysis of particle dispersed latent heat storage system, International Journal of Energy and Environment 1 (3) (2010) 445–458.

[7] H. Ettouney, I. Alatiqi, M. Al-Sahali, K. Al-Hajirie, Heat transfer enhancement in energy storage in spherical capsules filled with paraffin wax and beads, Energy Conversion and Management 47 (2006) 211–228.

[8] O. Mesalhy, K. Lafdi, A. Elgafy, K. Bowman, Numerical study for enhancing the thermal conductivity of phase change material (PCM) storage using high thermal conductivity porous matrix, Energy Conversion and Management 46 (6) (2005) 847–867.

[9] J.M. Martin, B. Zalba, L.F. Cabeza, H. Mehling, Improvement of a thermal energy storage using plates with paraffin-graphite composite, International Journal of Heat and Mass Transfer 48 (12) (2005) 2561–2570.

[10] A. Sari, C. Alkan, A. Karaipekli, O. Uzun, Microencapsulated n-octacosane as phase change material for thermal energy storage, Solar Energy 83 (10) (2009) 1757–1763.

[11] M.N.A. Hawlader, M.S. Uddin, M.M. Khin, Microencapsulated PCM thermal energy storage system, Applied Energy 74 (2003) 195–202.

[12] M. Lacroix, M. Benmadda, Numerical simulation of natural convection-dominated melting and solidification from a finned vertical wall, Numerical Heat Transfer Part A-Application 31 (1) (1997) 71–86.

[13] M. Lacroix, M. Benmadda, Analysis of natural convection melting from a heated wall with vertically oriented fins, International Journal of Numerical Methods for Heat and Fluid Flow 8 (4) (1998) 465–478.

[14] M.J. Huang, P.C. Eames, B. Norton, Thermal regulation of building-integrated photovoltaics using phase change materials, International Journal of Heat and Mass Transfer 47 (12– 13) (2004) 2715–2733.

[15] V. Shatikian, G. Ziskind, R. Letan, Numerical investigation of a PCM-based heat sink with internal fins, International Journal of Heat and Mass Transfer 51 (5-6) (2008) 1488-1493.

[16] R. Akhilesh, A. Narasimhan, C. Balaji, Method to improve geometry for heat transfer enhancement in PCM composite heat sinks, International Journal of Heat and Mass Transfer 48 (13) (2005) 2759–2770.

[17] M. Gharebaghi, I. Sezai, Enhancement of heat transfer in latent heat storage modules with internal fins, Numerical Heat Transfer Part A – Application 53 (7) (2008) 749–765.

[18] N. Sharifi, T.L. Bergman, A. Faghri, Enhancement of PCM melting in enclosures with horizontally-finned internal surfaces, International Journal of Heat and Mass Transfer 54 (19-20) (2011) 4182–4192.

[19] A. Faghri, Heat Pipe Science and Technology, Taylor & Francis, Washington, D.C., 1995.

[20] A. Faghri, Thermal Energy Storage Heat Exchanger, US Patent No. 4976308, 1990.

[21] A. Faghri, Micro Heat Pipe Energy Storage System, US Patent No. 5000252, 1991.

[22] C.E. Andraka, K.S. Rawlinson, N.P. Siegel, Technical feasibility of storage on large dish Stirling systems, Sandia report SAND2012-8352 (2012).

[23] Z. Liu, Z. Wang, C. Ma, An experimental study on heat transfer characteristics of heat pipe heat exchanger with latent heat storage. Part I: charging only and discharging only modes, Energy Conversion and Management 47 (2006) 944–966.

[24] Z. Liu, Z. Wang, C. Ma, An experimental study on heat transfer characteristics of heat pipe heat exchanger with latent heat storage, Part II: Simultaneous charging/ discharging modes, Energy Conversion and Management 47 (7-8) (2006) 967-991.

[25] C.W. Robak, T.L. Bergman, A. Faghri, Enhancement of latent heat energy storage using embedded heat pipes, International Journal of Heat and Mass Transfer 54 (15-16) (2011) 3476–3484.

[26] H. Shabgard, T.L. Bergman, N. Sharifi, A. Faghri, High temperature latent heat thermal energy storage using heat pipes, International Journal of Heat and Mass Transfer 53 (15-16) (2010) 2979–2988.

[27] H. Shabgard, C.W. Robak, T.L. Bergman, A. Faghri, Heat transfer and exergy analysis of cascaded latent heat storage with gravity-assisted heat pipes for concentrating solar power applications, Solar Energy 86 (3) (2012) 816-830.

[28] K. Nithyanandam, R. Pitchumani, Analysis and optimization of a latent thermal energy storage system with embedded heat pipes, International Journal of Heat and Mass Transfer 54 (21–22) (2011) 4596-4610.

[29] N. Sharifi, S. Wang, T.L. Bergman, A. Faghri, Heat pipe-assisted melting of a phase change material, International Journal of Heat and Mass Transfer 55 (13-14) (2012) 3458–3469.

[30] H. Shabgard, A. Faghri, T.L. Bergman, C.E. Andraka, Numerical simulation of heat pipe-assisted latent heat thermal energy storage unit for dish-Stirling systems, Journal of Solar Energy Engineering 136 (2) (2014) 021025-1-12.

[31] Y. Cao, A. Faghri, Transient two-dimensional compressible analysis for high-temperature heat pipes with pulsed heat input, Numerical Heat Transfer Part A - Applications 18 (4) (1990a) 483-502.

[32] A. Faghri, Y. Zhang, Transport Phenomena in Multiphase Systems, Academic Press, Elsevier, New York, 2006.

[33] A. Faghri, Y. Zhang, J. Howell, Advanced Heat and Mass Transfer, Global Digital Press, Columbia, Missouri, 2010.

[34] Y. Cao, A. Faghri, A numerical analysis of phase change problem including natural convection, ASME Journal of Heat Transfer 112 (1990b) 812-815.

[35] S. Wang, A. Faghri, T.L. Bergman, A comprehensive numerical model for melting with natural convection, International Journal of Heat and Mass Transfer 53 (9-10) (2010a) 1986-2000.

[36] S.V. Patankar, Numerical Heat Transfer and Fluid Flow, McGraw-Hill, New York, 1980.

[37] W.W. Jin, W.Q. Tao, Y.L. He , Z.Y. Li, Analysis of inconsistency of SIMPLE-like algorithms and an entirely consistent update technique-the CUT algorithm, Numerical Heat Transfer Part B – Fundamentals 53(4) (2008) 289-312.

[38] J.H. Ferziger, M. Peric, Computational Methods for Fluid Dynamics, Springer, New York, 1996.

[39] H.L. Stone, Iterative solution of implicit approximation of multidimensional partial differential equations, SIAM Journal on Numerical Analysis 5 (3) (1968) 530-558.

[40] T.L. Bergman, A.S. Lavine, F.P. Incropera, D.P. Dewitt, Fundamentals of Heat and Mass Transfer, seventh ed., Wiley, Hoboken, 2011.

[41] G.K. White, S.J. Collocot, Heat capacity of reference material: Cu and W, Journal of Physical and Chemical Reference Data 13 (4) (1984).

[42] P.D. Desai, Thermodynamic properties of iron and silicon, Journal of Physical and Chemical Reference Data 15 (3) (1986).

[43] M.J. Assael, A.E. Kalyva, K. D. Antoniadis, Reference data for the density and viscosity of liquid copper and liquid tin, Journal of Physical and Chemical Reference Data 39 (3) (2010).

[44] Y. Sato, Y. Kameda, T. Nagasawa, T. Sakamoto, S. Moriguchi, T. Yamamura, Y. Waseda, Viscosity of molten silicon and the factors affecting measurement, Journal of Crystal Growth 249 (2003) 404-415.

[45] http://www.engineeringtoolbox.com/

[46] NREL (National Solar Radiation Data Base at http://rredc.nrel.gov/solar/old_data/nsrdb/1991-2010/NCDCStationData/#C.

Chapter 5. Melting and Solidification Enhancement Using a Combined Heat Pipe, Foil Approach

Melting and solidification of a phase change material (PCM) is investigated, experimentally and computationally, using a novel heat pipe – metal foil approach. By embedding a PCM within a metal foil matrix, and delivering (or extracting) thermal energy to (or from) the matrix with a vertically-oriented heat pipe, overall thermal resistances between a working fluid and the PCM solid-liquid interface can be reduced. This leads to increased phase change rates relative to configurations involving only the heat pipe, or only a solid rod of the same physical dimensions as the heat pipe. For a small (approximately 1 percent) volume fraction of foil in the PCM - foil matrix, measured and predicted melting (solidification) rates associated with heat pipe – foil configurations are increased by approximately 300 percent (900 percent) relative to configurations involving the rod with no foil. Melting and solidification rates relative to configurations involving the heat pipe with no foil, are increased by approximately 200 percent and 600 percent. The influence of the heat pipe evaporator-to-condenser length ratio, as well as the overall temperature difference between the working fluid and the PCM fusion temperature, is also reported.

5.1. Introduction

Latent heat thermal energy storage (LHTES) is considered to be more advantageous than sensible TES for many applications because of its high energy density [1 - 6]. Also, because of the nature of phase change, the energy storage and delivery can occur with minimal temperature differences within a LHTES system. However, the low thermal conductivity of most inexpensive

phase change materials (PCMs) is a drawback, potentially limiting the heat transfer rates within, and phase change rates of the PCM.

Various strategies to overcome the large PCM thermal resistance have been proposed, including but not limited to use of high thermal conductivity porous matrices filled with PCM [7, 8], dispersion of high thermal conductivity particles within the PCM [9, 10], micro-encapsulation of the PCM [11, 12], use of extended surfaces [13 – 19], and use of heat pipes (HPs) which are capable of passively transferring large amounts of heat efficiently over considerable distances through small cross-sectional areas [20].

5.1.1. Heat pipe-assisted phase change (HP-PCM)

Two patents involving the integration of HPs with PCMs are held by Faghri [21, 22]. In related research, Horbaniuc et al. [23] analytically investigated the solidification of PCM surrounding a longitudinally-finned HP. It was shown that, as expected, addition of more fins to the HP increases PCM solidification rates. Similarly, incorporation of a HP heat exchanger in a LHTES system was investigated experimentally by Liu et al. [24] in which a circumferentially-finned, acetone-charged copper thermosyphon was considered, with stearic acid as the PCM. Water was the heat transfer fluid (HTF) used to, ultimately, melt or solidify the PCM. The influence of the HTF inlet temperature and the HTF mass flow rate on the heat transfer and phase change rates was of particular interest.

Motivated by applications involving concentrating solar power, Shabgard et al. [25] developed a thermal network model to simulate both charging (melting) and discharging (solidification) a high temperature LHTES system. Multiple HPs were positioned between the HTF and PCM in two distinct geometrical configurations; one with PCM surrounding a tube

through which flowed HTF, and the other involving PCM housed inside a tube across which the HTF flowed. The HPs increased the heat transfer rates to and from the PCM, and the improvement in phase change rates was quantified in terms of an effectiveness. The benefits associated with exploiting HP-assistance for LHTES were experimentally confirmed by Robak et al. [26] using an apparatus that consisted of a vertical cylindrical enclosure filled with n-octadecane. HPs were inserted between the HTF and the PCM, providing an effective thermal pathway to drive phase change. The measured thermal performance with HPs was compared to cases without HPs (i.e., transferring heat between the PCM and HTF through a plane wall) and again quantified in terms of an effectiveness. Melting rates for the HP configuration were approximately 60% higher than for the non-HP case, while solidification rates were approximately doubled relative to the plane wall case. The detailed numerical investigation of Sharifi et al. [27] provided additional insight into the heat transfer mechanisms responsible for the impressive thermal performance of the HP-PCM concept.

5.1.2. Foil-assisted phase change (Foil-PCM)

Melting and solidification rates can also be increased by adding high-thermal-conductivity material, such as metal foil, to a PCM. A representative numerical study considered the effect of integrating thin aluminum foils, arranged orthogonally with respect to the axis of a steam tube, within a PCM [28]. The PCM (a KNO_3 / $NaNO_3$ eutectic mixture) filled the spaces between individual foils, as well as between the foils and the tube. Predictions showed that the solidification time could be decreased by approximately 25% by either increasing the foil thickness or decreasing the foil pitch. In related work, Bayón et al. [29] experimentally tested a high temperature LHTES system charged by steam flowing from a parabolic-trough solar

collector. Expanded graphite foils were arranged on tubes in a sandwich configuration to increase the effective thermal conductivity of the PCM. The temporal variation of the outlet steam quality, along with the corresponding PCM (a KNO_3 / $NaNO_3$ eutectic mixture) temperature-time behavior showed that the complete charging time could be reduced significantly by incorporating the foils with the PCM. In a similar study, Sugawara et al. [30] investigated freezing of water around a horizontal copper tube, through which flowed a cold HTF. Copper foils of thickness 0.03 mm were positioned around the tube to increase the freezing rate. It was found that by using only 0.025 foil volume fraction, the solidification rate could be increased by a factor of four, relative to the case without foils.

In addition to increasing phase change rates for LHTES systems involving a HTF, use of foils offers other advantages relative to, for example, conventional finned heat transfer surfaces. First, foils are typically flexible because of their relatively small thickness compared to fins (or the interconnecting solid structures of metal porous foams) which are rigid. Structural flexibility is desirable, in that it can minimize the propensity for material damage or failure associated with the expansion and contraction of the PCM upon phase change, especially in high temperature applications where the metal itself may undergo considerable expansion from its initial cool state. Also, as will become evident, foils do not need to be physically attached to heat transfer surfaces by welding or fusion in order to increase, significantly, the thermal performance of a HTF-LHTES system. Finally, foils are typically inexpensive relative to conventional fins or metallic porous materials, in terms of both raw material and manufacturing costs.

Building on literature that has quantified the benefits of both (i) the HP-PCM and (ii) the Foil-PCM approaches, a novel concept (HP-Foil-PCM) is presented here that involves the integration of HPs with foils as a means to enhance the thermal performance of LHTES systems.

The objective is to experimentally and analytically determine the thermal performance of the HP-Foil-PCM concept.

5.2. Experimental apparatus

As shown in Fig. 5.1, a PCM is contained within an upright cylindrical enclosure that is formed by an acrylic tube of $D_{e,i}$ = 41 mm inner diameter, L_e = 125 mm height, and 4.6 mm wall thickness. The bottom of the enclosure consists of a 5 mm thick acrylic disk of 50.2 mm diameter, while the top of the enclosure is a 10 mm thick aluminum plate. A compartment of air overlies the PCM to allow for (i) PCM expansion and, as will become evident, (ii) measurement of the instantaneous PCM solid or liquid fraction. The enclosure is made air-tight by sealing the interfaces with synthetic O-rings, both of which are compressed by the all-threaded yoke structure.

A centrally-located, L_{hp} = 175 mm long, D_{hp} = 6 mm outer diameter, copper-water HP (Enertron, model HP-HD06DI17500BA) penetrates the bottom of the enclosure. The HP bottom and adiabatic sections (of lengths L_b + L_a, respectively) are located within an underlying heat exchanger, while the HP top section (of length L_t) is in the PCM. During solidification, the HP bottom section serves as the HP condenser, while evaporation of the HP working fluid occurs in the HP top section. During PCM melting, evaporation (condensation) occurs in the bottom (top) section of the HP. The HP is secured in place by silicone adhesive, which also ensures an air-tight seal.

Heat is supplied to, or extracted from, the bottom section of the HP by a HTF (water) flowing in a heat exchanger formed of five 10 mm thick welded aluminum plates, and an overlying acrylic plate of thickness 3 mm. The heat exchanger has overall dimensions of 140 mm

(length) × 100 mm (width) × 102 mm (height). To thermally isolate the PCM from the HTF (except through the thermal pathway provided by the HP), an air gap of 2 mm thickness separates the upper acrylic plate of the heat exchanger from the bottom acrylic disk of the PCM enclosure. In addition, air that is trapped in the uppermost 20 mm of the heat exchanger is not bled from the system, providing an additional thermal resistance between the HTF and the PCM. Lauda RM5 circulators were used to control the HTF temperature.

Prior to adding PCM (99% pure n-octadecane with a melting temperature of $T_m \approx 28°C$) to the enclosure, aluminum foils of thickness 0.017 mm, outer diameter of $D_{f,o} = D_{e,i} - 2$ mm = 39 mm, and inner diameter $D_{f,i} = D_{hp} - 2$ mm = 4 mm were press fitted along the top section of the HP (of length L_t). The installation method is sufficient to secure the foils in an approximately fixed location during phase change of the PCM. Once assembled, the entire apparatus was insulated with fiberglass batting (20 mm thick) held within a box constructed of 37 mm thick expanded polystyrene insulation. The thermophysical properties of the PCM and other components are listed in Table 5.1.

Local temperatures were measured with 15 Teflon-coated, 254 μm diameter chromel-alumel (K-type) thermocouples, the locations of which are provided in Table 5.2, (except for T_{14} and T_{15}, which were inserted in the heat exchanger inlet and outlet, respectively). The r - z coordinate system is shown in Fig. 5.1. All of the thermocouples were fabricated from the same spools of wire to minimize bias error when measuring temperature differences, and were calibrated using the boiling and freezing points of distilled water to within an estimated uncertainty of ± 0.1°C. The placement accuracy of the thermocouples, which were inserted through small holes drilled in the vertical wall of the acrylic cylinder that were subsequently sealed with silcone, is ± 1mm.

Thermocouple voltages were collected using a National Instruments data acquisition (NI CDAQ-9172) system at 1 second intervals using LabVIEW software.

In addition to local temperatures, the instantaneous PCM liquid fraction was determined by monitoring the air pressure and temperature within the air-tight enclosure, using the procedure reported in Appendix A. As such, a pressure transducer (Sper Scientific, Model PS100 - 2BAR) was installed in the top enclosure plate. The output voltage from the transducer was collected (Sper Scientific, Model 840065) at 60 s intervals. Using the sequential perturbation method [31], the uncertainty in the measured liquid fraction can be estimated, as discussed in Appendix A.

5.3. Experimental procedure

5.3.1. PCM melting

For the experiments involving melting, the PCM was first heated and de-gassed under vacuum. Once conditioned, a small amount of the molten PCM was poured into the enclosure, creating an initial liquid layer approximately 5 mm thick. The test cell was then shaken gently to remove, to the extent possible, air trapped between the individual foils. Subsequently, the heat transfer fluid, at $T_{htf,in} = T_{14} = 11°C$, was directed to the test cell to solidify the PCM layer, and the process was repeated until the desired total amount of PCM was added to the enclosure. After filling, the test cell was leveled, insulated, and allowed to equilibrate at room temperature for 12 hours.

Prior to the start of an experiment, the heat transfer fluid, at $T_{htf,in} = 25°C$, was circulated in the heat exchanger for approximately one hour to increase the solid PCM temperature to approximately 25°C. Subsequently, the HTF flow to the heat exchanger was curtailed, and the circulating bath temperature was increased to the experimental set point, $T_{htf,in} = T_{14} = 45°C$.

Once this temperature was achieved, the HTF was re-introduced to the heat exchanger, marking the start of an experiment. Each experiment was terminated when the PCM was completely melted, as determined by observing a constant air pressure. The mass of PCM used was approximately 0.09 kg, 0.08 kg or 0.072 kg, corresponding to L_t = 90 mm, 80 mm or 72 mm, respectively.

5.3.2. PCM solidification

Solidification experiments begin with liquid, de-gassed PCM within the enclosure. Warm HTF was circulated to bring the temperature of the liquid PCM to an initial value of approximately 31°C. Once the measured PCM temperatures reached the desired value, a second chiller (Lauda, RM5), circulated the heat transfer fluid to the heat exchanger with $T_{htf,in} = T_{14}$ = 11°C, marking the start of the experiment. Each solidification experiment was curtailed when the PCM solidified completely, as indicated by a constant measured air pressure.

Each experiment was conducted twice to ensure repeatability. Differences in the results of the two experiments were found to be minor with, for example, instantaneous liquid fractions in agreement to within 1 percentage point. The experimental results presented here correspond to the averaged measured values of the two experiments.

5.4. Physical model

A numerical model was developed to simulate the transient response of the conjugate system composed of the PCM and foils (or pure PCM without foils), the HP (or, a solid rod of the same exterior dimensions as the HP), and the enclosure walls. For cases without foils, natural convection occurs in the PCM, and the mass, momentum and energy equations are solved using

a transient, two-dimensional finite volume approach that incorporates the temperature-transforming model [32, 33]. For cases involving PCM *and* foils, both solidification and melting of the PCM are considered to be conduction-dominated.

Several additional assumptions are made regarding the physical system. The exterior of the PCM enclosure, as well as the top and bottom ends of the HP (or the solid rod) are adiabatic. All thermophysical properties are assumed to be constant except for the density of the HP working fluid, which is considered to be an ideal gas experiencing two-dimensional, laminar, and compressible flow. The HP wick is assumed to be fully saturated, and the HP working fluid at the wick-vapor interface is assumed to be in its saturated state. Liquid flow in the HP wick is neglected [34] since a sufficient capillary pressure is assumed to be provided by the HP wick to drive the liquid in the wick, for the operating conditions presented here. The Boussinesq approximation is applied to the molten PCM, and natural convection is assumed to be two-dimensional, incompressible, and laminar. Thermal radiation is assumed to be negligible, as are thermal contact resistances.

5.4.1. Computational domain

The computational domain is shown in Fig. 5.2a. As evident, the HP is segmented into three radial regions: the vapor phase of the HP working fluid, the wick (of thickness 0.4 mm), and the HP solid wall (of thickness 0.25 mm). The annular space between the HP and interior enclosure wall (both of length L_t) is filled with the foil-PCM composite, or with pure PCM. The lower portion of the system consists of the HP adiabatic section (of length L_a) and the HP bottom section (of length L_b).

5.4.2. Effective thermophysical properties

The effective thermophysical properties of the HP wick are calculated by averaging the properties of the HP working fluid and copper wick shown in Table 5.1, yielding k_{eff} = 201 W/m·K and $(\rho c_p)_{eff}$ = 3803 kJ/m^3·K [20].

The foil-PCM composite is considered to be an anisotropic PCM with distinct effective thermal conductivities in the radial and axial directions. Because of the foil dimensions, and the manner in which the foils are installed in the enclosure, care was taken to describe the effective properties in each of the three foil-PCM sub-regions described in Fig. 5.2b.

Region I. Region I is composed of the foils and the pure PCM and is not adjacent to the HP (or rod). Based upon the foil thickness and planar area, the number of foils, and the overall volume of Region I, the experimental foil volume fraction is calculated to be f_f = 0.0121. The effective thermophysical properties are calculated based upon this foil volume fraction, using the thermophysical properties of Table 5.1, and are shown in Table 5.3. Specifically, the effective thermal conductivities in the radial and axial directions of Region I are determined by considering the foil and PCM thermal resistances to be in parallel and series, respectively [35].

Region II. Intimate contact between the foil and the HP is not possible and, from the perspective of enhancing durability through multiple phase change cycles, is not desirable. Based upon microscopic inspection of the experimental apparatus, a gap usually exists between the foil and the HP, typically of width 0.0 mm $\leq$ $r_g - r_{hp}$ $\leq$ 0.02 mm. Based upon this inspection, a gap width of 0.01 mm is assumed. The radial dimension of the computational control volume (or cell) adjacent to the exterior of the HP is $r_{cell} - r_{hp}$ = 0.251 mm. Using this as the radial dimension of a unit cell within Region II, and $(t_{pcm} + t_f)/2$ as the cell's axial dimension, the unit

cell consists of a LHS sub-region consisting of pure PCM (extending from r_{hp} to $r_g = r_{hp} + 0.01$ mm), a RHS sub-region consisting of pure foil (extending from $r = r_g$ to $r = r_{cell}$), and a second RHS sub-region consisting of pure PCM (also extending from $r = r_g$ to $r = r_{cell}$). Based on the foil thickness and pitch, as well as the gap between the HP and foil, the foil volume fraction in Region II is $f_f = 0.0116$, yielding the effective densities, specific heats, and latent heats of fusion reported in Table 5.3. Radial conduction through the unit cell occurs through a lane consisting of pure PCM, and a second, parallel lane consisting of PCM and foil in series. Conduction in the axial direction occurs through a lane of pure PCM adjacent to the HP, and a second, parallel lane consisting of PCM and foil in series. The anisotropic nature of the foil-PCM composite is accounted for by the effective radial and axial thermal conductivities that are calculated using an equivalent resistance network approach [35] and are reported in Table 5.3.

Region III. Acrylic properties are applied in Region III.

5.4.3. Boundary and initial conditions

A constant and uniform temperature, T_b, is applied along the vertical exterior of the HP bottom section. Radial gradients of temperature, pressure, and the axial velocity component, as well as the radial velocity component, are zero at $r = 0$. The remaining external boundaries (including the top of the PCM and the HP at the same vertical location) are adiabatic. No-slip conditions are specified at all solid surfaces as well as at the top boundary of the domain. The entire domain is specified to be initially isothermal at 3ºC below (above) the fusion temperature of the PCM for the melting (solidification) simulations.

5.4.4. Numerical methodology

Without the foil, natural convection occurs in the PCM during melting, and the governing mass, momentum and energy equations for both the HP and PCM are described in [27]. For cases involving foil, heat transfer within the foil-PCM composite is conduction-dominated, requiring solution of only the energy equation in the composite, using the effective thermophysical properties of Table 5.3. Preliminary simulations were performed using grid sizes up to 240 × 120 ($z \times r$), for a L_t = 90 mm, L_b = 55 mm case. A 200 × 100 ($z \times r$) grid with a time step of Δt = 0.1 s was found to be sufficient to achieve grid size and time step independent solutions. A convergence criterion (maximum difference between two successive iterations and matrix residuals) of 10^{-5} was specified for all independent variables.

5.5. Results and discussion

Measured and predicted local temperatures for two representative melting experiments are reported in Fig. 5.3. For the HP case (Fig. 5.3a; no foil, L_t = 90 mm, L_b = 55 mm), the agreement between measured and predicted local temperatures is good, with modest differences attributed to heat losses in the experiments. When the melt front passes through a thermocouple location, a sharp increase in temperature occurs. Hence, melting proceeds from top-to-bottom along the vertical plane of the thermocouples, as expected when melting is influenced by natural convection. In contrast, for the HP-Foil case (Fig. 5.3b), melting occurs nearly uniformly in the outward radial direction, also as expected since natural convection is suppressed by the horizontal foils and the HP is of relatively uniform temperature. It should be noted that upon melting (or expansion) of PCM between two adjacent foils, approximately similar forces apply on the top and bottom of each foil, minimizing foil displacement. Therefore, during the phase

change the foil spacing remains small and noticeable natural convection flows are not established. The negligible foil displacement was also confirmed experimentally. Importantly, melting proceeds more rapidly for the case with foil, even though natural convection is suppressed. Note that for both cases of Fig. 5.3, the measured temperatures at the evaporation section of the HP are nearly constant at $T_{htf,in} = 45°C$.

Predicted temperature distributions for the HP-Foil, HP and Rod cases with $L_t = 90$ mm and $L_b = 55$ mm are shown in Fig. 5.4. The lower and outer boundaries of the PCM domain are identified with dashed lines, and the $T_m = 28°C$ isotherm (the isotherm furthest from the centerline) corresponds to the PCM solid-liquid interface. The predictions correspond to, from left to right, melt fractions of $f_\ell \approx 0.2$, 0.4, 0.6, and 0.8.

As evident, the HP-Foil configuration (Fig. 5.4a) experiences the most rapid melting, with attainment of $f_\ell \approx 0.8$ at $t \approx 1400$ s. In contrast, the $f_\ell \approx 0.8$ condition is attained at $t \approx 5800$ s and $t \approx 8200$ s for the HP (Fig. 5.4b) and Rod (Fig. 5.4c) cases, respectively. Superior melting rates are achieved by the HP-foil configuration with only $f_f \approx 1.21\%$ foil volume fraction, and are due to the increase in the effective thermal conductivity associated with usage of the foil, and to the reduced thermal mass of the HP relative to that of the solid rod.

Predicted and measured melting histories, reported in terms of the time variation of the liquid fraction, are shown in the LHS column of Fig. 5.5 for various L_t/L_b ratios. Regardless of the value of L_t/L_b, the HP-foil configuration promotes the highest melting rates, and the Rod configuration exhibits the slowest melting, as expected. For the $L_t = 90$ mm case (LHS Fig. 5.5a), the HP and Rod-Foil configurations yield nearly the same rates of melting. The relative insensitivity of the melting rate to L_t/L_b reflects the fact that the thermal resistances associated with the bottom section of the heat pipe are small, relative to the thermal resistance posed by the

PCM. Combining the HP with the foils results in an approximately 200% increase in the overall melting rate, compared to the HP configuration.

Melting performance may be quantified in terms of a melting effectiveness,

$$\varepsilon_m = \frac{f_\ell(t)}{f_{\ell,rod}(t)} \tag{1}$$

where the Rod configuration is considered to be the basis for comparison. The temporal variation of ε_m for various configurations is reported on the RHS of Fig. 5.5. The melting effectiveness is initially high for the HP-Foil case due to the combined effects of (i) the low thermal mass of the HP relative to the rod, and (ii) the large radial effective thermal conductivity of the PCM-foil composite. The effectiveness of melting for the HP and Rod-Foil configurations moderately exceed that of the base configuration (ε_m = 1). An average melting effectiveness may be defined as the average of the ε_m over the time of melting and dividing by the total melting time, yielding, for example, $\bar{\varepsilon}_m$ = 4.7 and 1.5 for the L_t = 90 mm case. As may be inferred from the LHS of Fig. 5.5, the average melting effectiveness values are insensitive to L_t / L_b for the range of parameters considered here.

Solidification results are reported in Fig. 5.6. Here, a solidification effectiveness is defined as

$$\varepsilon_s = \frac{1 - f_\ell(t)}{1 - f_{\ell,rod}(t)} \tag{2}$$

and is used to compare the performance of the various configurations. Note that the difference between the HTF inlet temperature and the PCM melting temperature is the same for solidification (Fig. 5.6) as for melting (Fig. 5.5).

A comparison of the results of Figs. 5.5 and 5.6 shows that, in general, solidification occurs faster than melting, the difference in phase change rates being attributed to the higher thermal conductivity of the solid PCM, relative to that of the liquid PCM (Table 5.1). For the HP-Foil cases, the solidification rates are relatively constant throughout the phase change process, reflecting the relatively low thermal resistance between the HP and the solid-liquid interface. In contrast, solidification rates decay with time for the non-foil cases, as expected since the thermal resistance between the HTF and solid-liquid interface increases with time for configurations without foil. Predicted and measured phase change rates are in good agreement early on, but the agreement deteriorates in the later stages of solidification, particularly for the non-foil cases. The difference between the measured and predicted solidification rates is attributed to the probable development of thermal contact resistances at the HP-solid PCM (or rod-solid PCM) interface. In addition, the performance of the HP may be less robust during solidification than during melting since gravitational forces oppose the flow of the liquid HP working fluid during solidification; this effect is not included in the model.

Trends similar to those noted for melting (Fig. 5.5) are also evident for solidification (Fig. 5.6). Measured solidification rates associated with the HP-Foil configuration are approximately 900% and 600% higher than those of the Rod and HP configurations, respectively. Also, solidification rates for the HP configurations are increased by approximately 50% relative to the Rod configuration. The solidification effectiveness is slightly more sensitive to L_t/L_b than the melting effectiveness, and the average solidification effectiveness is $\bar{\varepsilon}_s = 4.29$ and 1.18 for the HP-Foil and HP configurations, respectively, for the $L_t = 90$ mm case.

The influence of the overall temperature difference, $\left|T_{htf} - T_m\right|$, on the melting and solidification for the HP-Foil case with L_t = 90 mm and L_b = 55 mm is shown in Fig. 5.7. As expected, melting and solidification rates increase as the driving temperature increases. Again, the solidification rate is higher than the melting rate for each driving temperature because of the higher thermal conductivity of the solid phase.

5.6. Conclusions

An experimental and numerical investigation of melting and solidification involving a heat pipe acting in conjunction with metal foils has been conducted. The melting (solidification) rates associated with the HP-Foil configuration are approximately 300% (900%) higher than that of a bare copper rod of the same physical dimensions as the HP. Superior phase change rates are achieved by utilizing only 1.21% foil volume fraction within the PCM in conjunction with the HP, permitting nearly the same total amount of latent energy to be stored within a fixed storage volume.

Integration of HPs with foils may be a preferred option to improve, perhaps significantly, the heat transfer rates in a broad range of applications involving melting and solidification and/or latent thermal energy storage. Not only is the thermal performance considered to be very good, the integrated HP-foil concept involves usage of less metal than solid metallic extended surfaces (such as the rod considered here) and, as such, can be less expensive and lighter-weight than conventional configurations.

5.7. Appendix A. Measured Liquid Volume Fraction and Its Uncertainty

Of interest is the time variation of the PCM liquid volume fraction, defined as $f_\ell \equiv V_{\ell,PCM}/(V_{\ell,PCM} + V_{s,PCM})$, and its uncertainty. As suggested in Fig. 5.A.1, during melting the initially solid PCM occupies the volume $V_{s,i} = \pi L_t (r_{e,i}^2 - r_{hp}^2) - V_f$, and the overlying air is of volume $V_{air,i} = \pi r_{e,i}^2 (L_e - L_t)$ where L_e is the internal height of the enclosure. The initial air pressure and temperature are $p_{air,i}$ and $T_{air,i}$, respectively. The decrease in air volume due to PCM expansion upon melting, coupled with the change in air temperature, causes a variation in the air pressure that is detected by the pressure transducer of Fig. 5.1. The measured air temperature and pressure are ultimately used to determine the instantaneous liquid fraction as follows.

As the PCM melts, the change in the volume occupied by solid PCM, ΔV_s, can be determined from (i) knowledge of the change in air volume, $\Delta V_{air} = (V_{air} - V_{air,i})$, (ii) the conservation of mass principle ($\Delta m_s + \Delta m_\ell = 0$) which may be written

$$\rho_s \Delta V_s + \rho_\ell \Delta V_\ell = 0 \tag{A.1}$$

and (*iii*) recognition that the total volume is fixed, or

$$\Delta V_\ell + \Delta V_s + \Delta V_{air} = 0 \tag{A.2}$$

Combining Eqs. (A.1) and (A.2) yields

$$\Delta V_s = \frac{\Delta V_{air}}{\frac{\rho_s}{\rho_\ell} - 1} \tag{A.3}$$

Noting that $V_s = V_{s,i} + \Delta V_s$ and $V_\ell = \Delta V_\ell$, the definition of the liquid fraction and Eq. (A.3) may be combined to yield

$$f_\ell = \frac{V_\ell}{V_\ell + V_s} = \frac{\Delta V_\ell}{\Delta V_\ell + V_s} = \frac{\Delta V_s + \Delta V_{air}}{\Delta V_{air} - V_{s,i}} \tag{A.4}$$

Assuming the air is well-mixed and behaves as an ideal gas,

$$V_{air} = \frac{m_{air} R T_{air}}{p_{air}} \quad \text{and} \quad m_{air} = \frac{V_{air,i}\, p_{air,i}}{R T_{air,i}} \tag{A.5a,b}$$

and, using the expression $p_{air} = p_{air,i} + \Delta p_{air}$, Eqs. (A.4) and (A.5) may be combined with the definitions of the initial air and PCM volumes to yield

$$f_\ell = \frac{\dfrac{1}{1 - \dfrac{V_{s,ref}}{V_{\ell,ref}}} \times \pi r_{e,i}^2 (L_e - L_t) \times \left(\dfrac{p_{air,i}}{T_{air,i}} \dfrac{T_{air}}{(p_{air,i} + \Delta p_{air})} - 1 \right)}{\pi r_{e,i}^2 (L_e - L_t) \times \left(\dfrac{p_{air,i}}{T_{air,i}} \dfrac{T_{air}}{(p_{air,i} + \Delta p_{air})} - 1 \right) - \pi (r_{e,i}^2 - r_{hp}^2) L_t + \dfrac{m_f}{\rho_f}} \tag{A.6}$$

All of the parameters of Eq. (A.6) are known ($p_{air,i}$ is taken to be standard atmospheric pressure in Storrs, CT) except for Δp_{air}, and T_{air} which are determined experimentally. However, the liquid fraction calculated using Eq. (A.6) is highly sensitive to the ratio of the PCM phase densities, and substantial differences in the density ratio exist, based upon density values of the individual phases reported in the literature. As such, the density ratio was determined experimentally by solidifying a mass of de-gassed PCM in a graduated cylinder to determine the volume of the PCM in both solid phase ($V_{s,ref}$) and liquid phase ($V_{\ell,ref}$) as reported in Table 5.A.1.

The uncertainty of the PCM liquid volume fraction is determined using the sequential perturbation method [31]. The uncertainty of each independent variable appearing in Eq. (A.6) is calculated based on the resolution (*res*) and accuracy (*acc*) associated with its measurement as

$u = \sqrt{res^2 + acc^2}$. Note that the air is assumed to be well-mixed and T_{air} is taken as the average of T_5 and T_{10}. Since Δp_{air}, and T_{air} vary with time, the uncertainty in f_ℓ also changes with time and is calculated at each instant. A similar analysis is used for the solidification process.

Nomenclature

acc	accuracy
c_p	specific heat at constant pressure (J/kg·K)
D	diameter (m)
f_f	foil volume fraction
f_ℓ	volumetric liquid fraction
g	gravitational acceleration (m/s^2)
h_{fg}	latent heat of vaporization (kJ/kg)
$h_{s\ell}$	latent heat of fusion (kJ/kg)
HP	heat pipe
HTF	heat transfer fluid
k	thermal conductivity (W/m·K)
L	length (m)
m	mass (kg)
p	pressure (Pa)
r,z	coordinate directions (m)
R	gas constant (J/kg·K)
res	resolution
t	time (s or min), thickness (m)
T	temperature (K), thermocouple
u	uncertainty
V	volume (m^3)

Greek

β	thermal expansion coefficient (K^{-1})
ε	effectiveness
μ	dynamic viscosity (Pa·s)
ρ	density (kg/m^3)

Subscripts

a	adiabatic
air	air
b	bottom
cell	computational unit cell
e	enclosure
eff	effective
f	foil
g	gap
hp	heat pipe
htf	heat transfer fluid
i	inner, initial
in	inlet
ℓ	liquid phase of PCM
m	melting
o	outer
out	outlet
PCM	phase change material
r,z	coordinate directions
ref	reference
rod	rod
s	solid phase of PCM, solidification
sat	saturation
t	top
v	vapor phase of heat pipe working fluid
w	wall

Table 5.A.1. Measured parameters and the corresponding uncertainties. All parameters and uncertainties for the experiment involving the rod are the same as those involving the HP. The diameters of the HP and rod are equal.

Independent variable	Value	Resolution (*res*)	Accuracy (*acc*)	Uncertainty (*u*)
$r_{e,i}$ [1]	20.64 mm	0.025 mm	± 0.051 mm	± 0.057 mm
r_{hp} or r_{rod} [1]	3.01 mm	0.025 mm	± 0.051 mm	± 0. 057 mm
$p_{air,i}$ [2]	99.1 kPa	-	± 1 kPa	± 1 kPa
$T_{air,i}$ [3]	298 K	-	± 0.1 K	± 0.1 K
T_{air} [3]	$T_{air}(t)$	-	± 0.1 K	± 0.1K
Δp_{air} [4]	$\Delta p_{air}(t)$	0.1 kPa	± $0.02\Delta p_{air}(t)$	varies with time
m_f [5]	3.8 g	0.1 g	± 0.1 g	± 0.141 g
L_t	90 mm	1 mm	± 1 mm	± 1.41 mm
L_e	125 mm	1 mm	± 1 mm	± 1.41 mm
$V_{s,ref}$	22.7 ml	0.1 ml	± 0.15 ml	± 0.18 ml
$V_{\ell,ref}$	24.7 ml	0.1 ml	± 0.15 ml	± 0.18 ml

[1] $r_{e,i}$, r_{hp}, r_{rod}: http://ecatalog.mitutoyo.com/Dial-Calipers-Series-505-C1387.aspx
[2] $p_{air,i}$: http://www.idcide.com/citydata/ct/storrs.htm (elevation of Storrs, CT)
[3] $T_{air,i}$, T_{air} : http://www.ni.com/pdf/manuals/372499b.pdf (temperature accuracy/uncertainty)
[4] Δp_{air}: http://www.sperdirect.com/mas_assets/manuals/840065-i.pdf (meter resolution & accuracy)
[5] m_f : Mettler Toledo XS10001M Scale (mass resolution & accuracy)

Table 5.1. Thermophysical properties at $T = 301$K.

	PCM	HP working fluid	HP or Rod	Foil	Enclosure
Material	n-Octadecane [26]	Water [20]	Copper [35]	Aluminum [35]	Acrylic [36]
Density, ρ (kg/m^3)	770 (liquid) 800 (solid)	996.6 (liquid)	8933	2702	1150
Thermal conductivity, k (W/m·K)	0.148 (liquid) 0.358 (solid)	0.6132 (liquid) 0.01932 (vapor)	401	237	0.2
Specific heat, c_p (J/kg·K)	2160 (liquid) 1912 (solid)	4181 (liquid) 1882 (vapor)	385	903	1470
Viscosity, μ (Pa·s)	3.09×10^{-3}	8614×10^{-7} (liquid) 91.74×10^{-7} (vapor)			
Latent heat, h_{sl} or h_{fg} (kJ/kg)	243.5	2434.9			
Melting point, T_m (K)	301				
Vapor pressure, p_{sat} (Pa)		4352			
Thermal expansion coefficient, β (K^{-1})	9×10^{-4}				

Table 5.2. Thermocouple locations, See Fig. 5.1.

Thermocouple	*r*-coordinate (mm)	*z*-coordinate (mm)
T_1	13	105
T_2	13	125
T_3	13	145
T_4	13	165
T_5	13	195
T_6	-13	105
T_7	-13	125
T_8	-13	145
T_9	-13	165
T_{10}	-13	195
T_{11}	3	15
T_{12}	3	30
T_{13}	3	45

Table 5.3. Effective thermophysical properties.

	Region I, (f_f = 0.0121)	Region II (f_f = 0.0116)
ρ_{eff} (kg/m^3)	793(liquid) 823(solid)	792(liquid) 822(solid)
$c_{p,eff}$ (J/kg·K)	2109 (liquid) 1872(solid)	2110(liquid) 1873(solid)
$h_{sl,eff}$ (kJ/kg)	233.5(liquid) 233.8 (solid)	233.9(liquid) 234.2(solid)
$k_{eff,r}$ (W/m·K)	3.01(liquid) 3.21(solid)	0.188(liquid) 0.454(solid)
$k_{eff,z}$ (W/m·K)	0.149(liquid) 0.362(solid)	0.149(liquid) 0.362(solid)

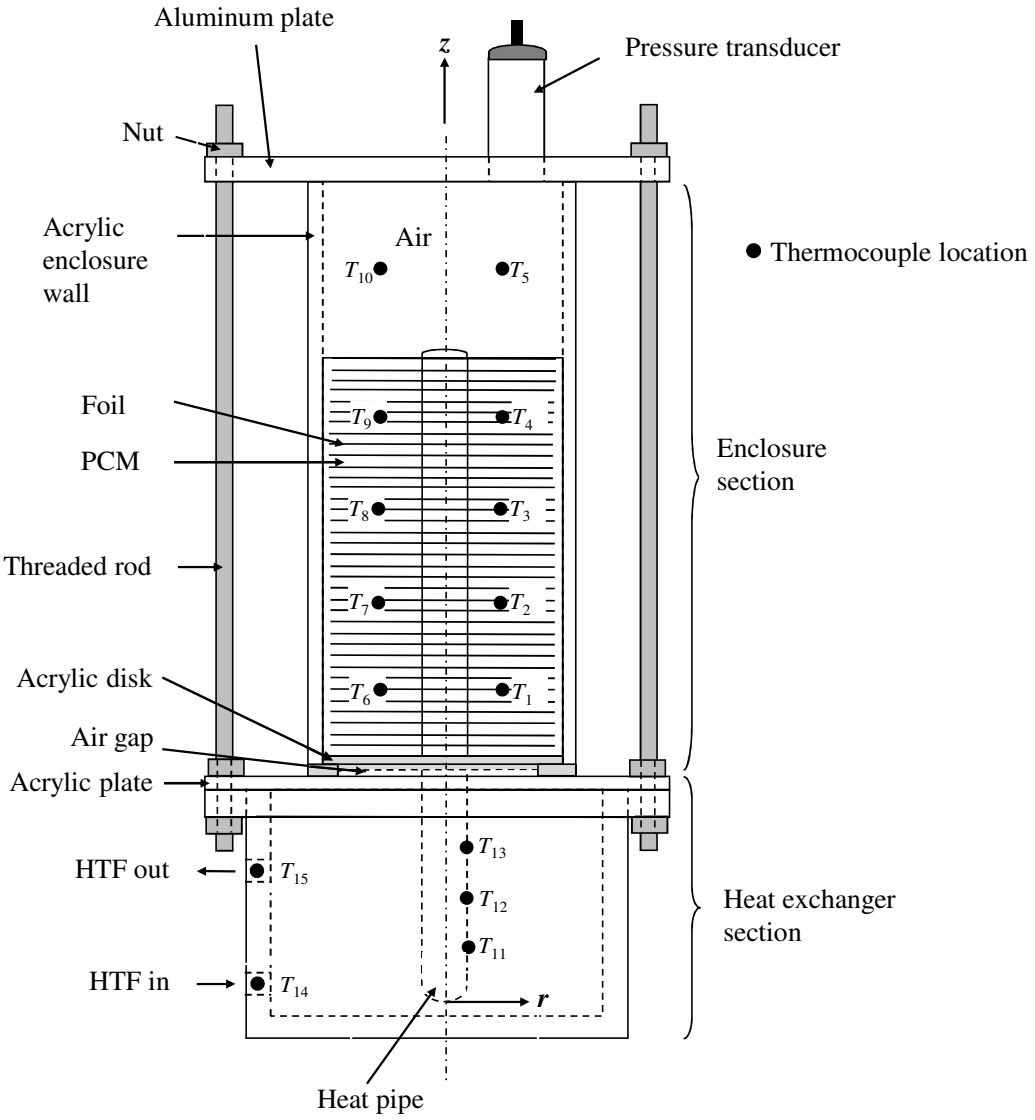

Fig. 5.1. Experimental setup.

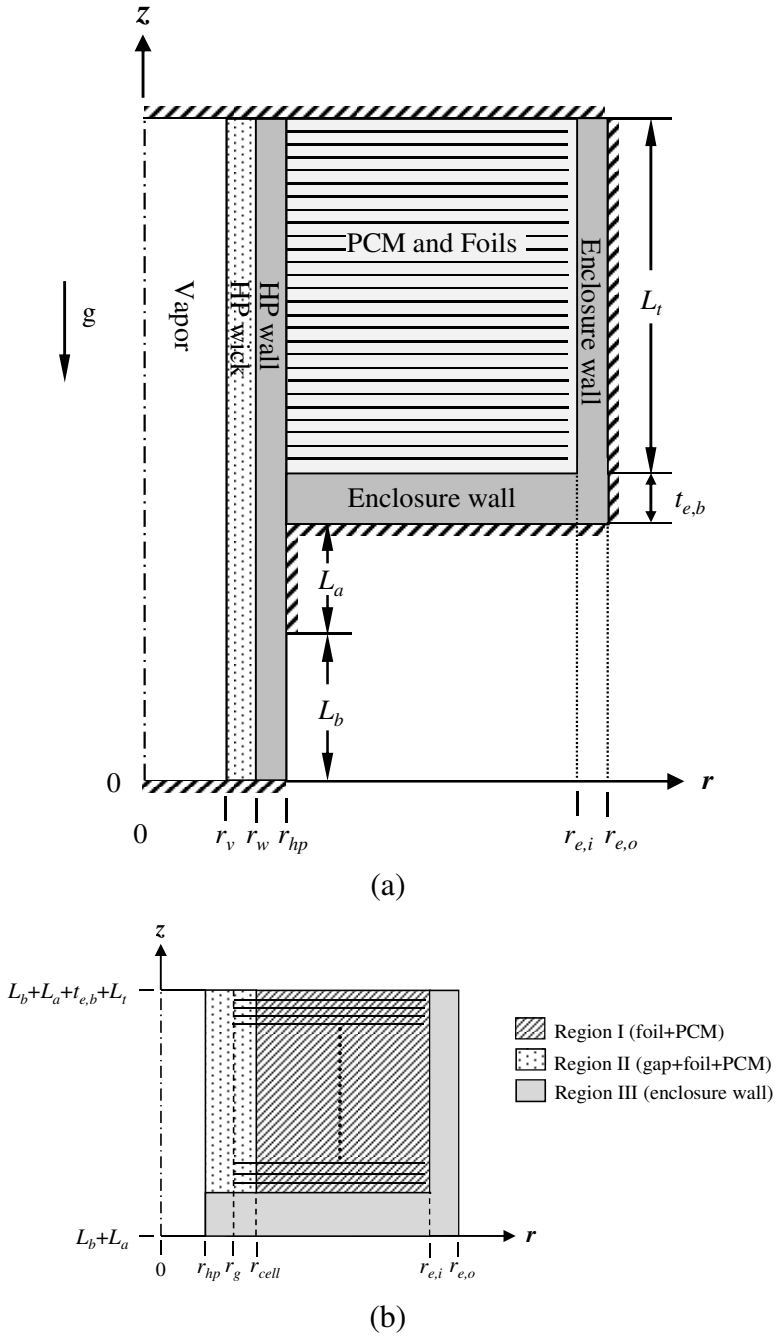

Fig. 5.2. Test cell geometry: (a) computational domain, (b) PCM sub-regions.

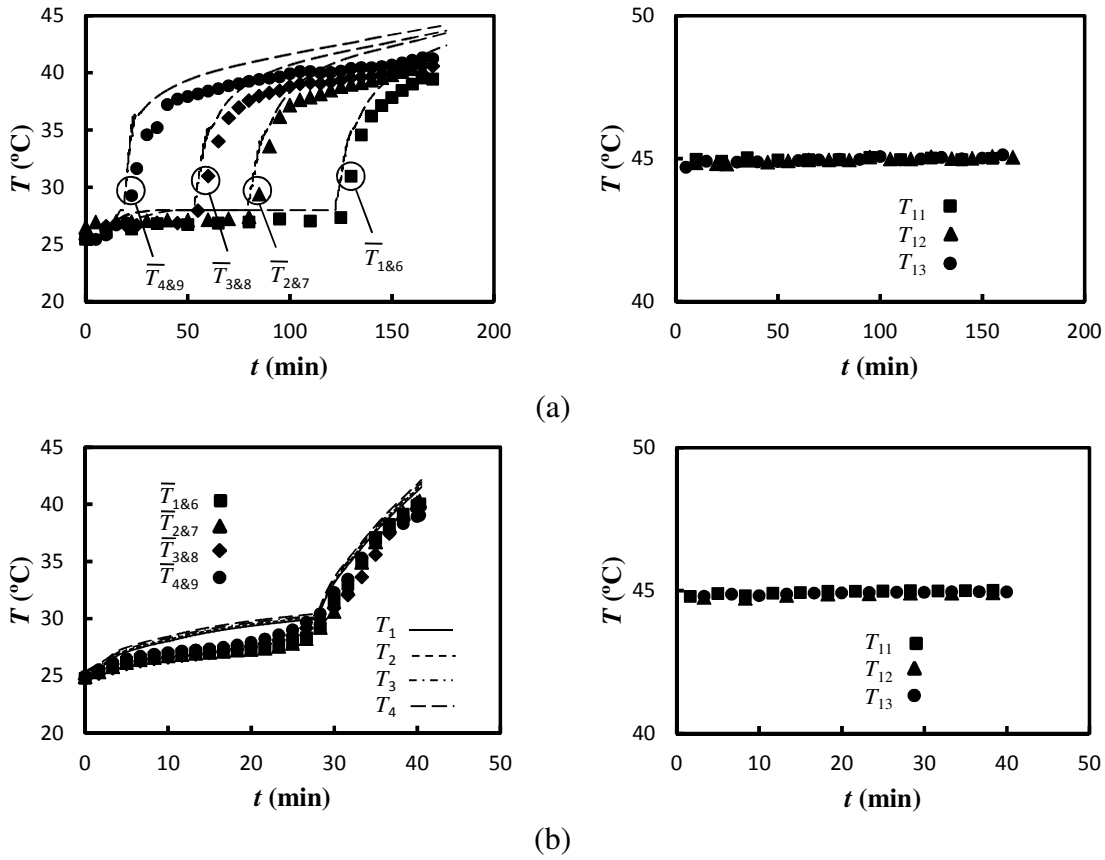

Fig. 5.3. Temperatures within the PCM (left) and on the HP evaporator section (right) during melting with L_t = 90 mm, L_b = 55 mm: (a) HP, (b) HP-Foil (f_f = 0.0121).

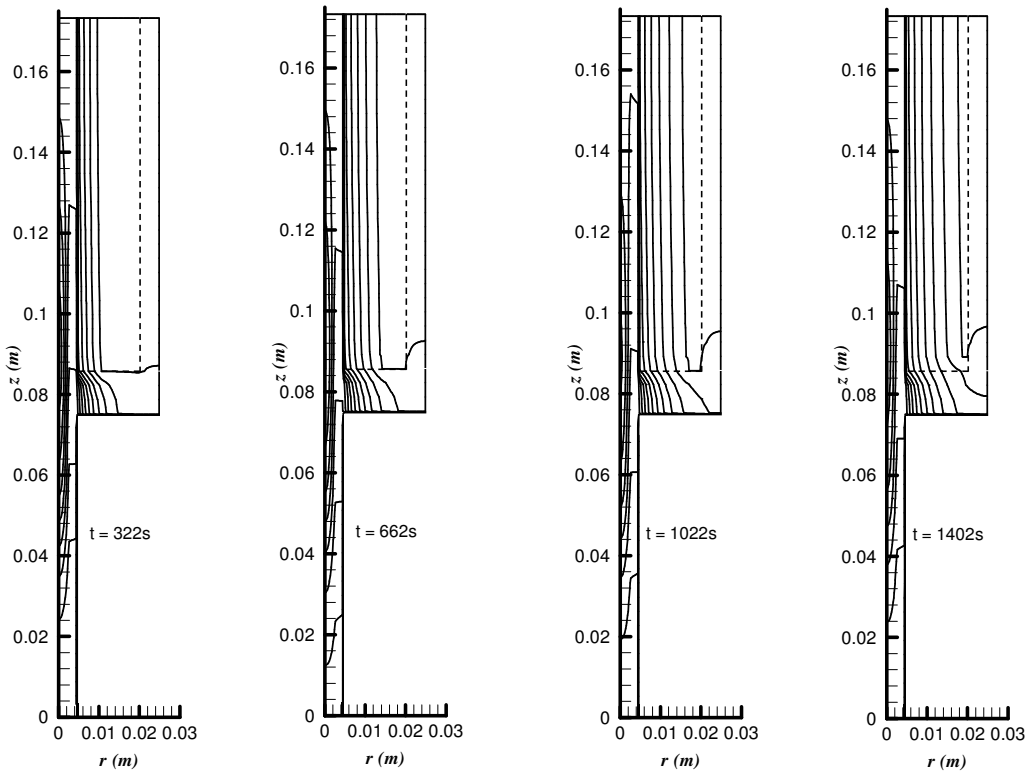
0.16
0.14
0.12
0.1
0.08
0.06
0.04
0.02
0
z (m)
t = 322s
t = 662s
t = 1022s
t = 1402s
0 0.01 0.02 0.03
r (m)

(a)

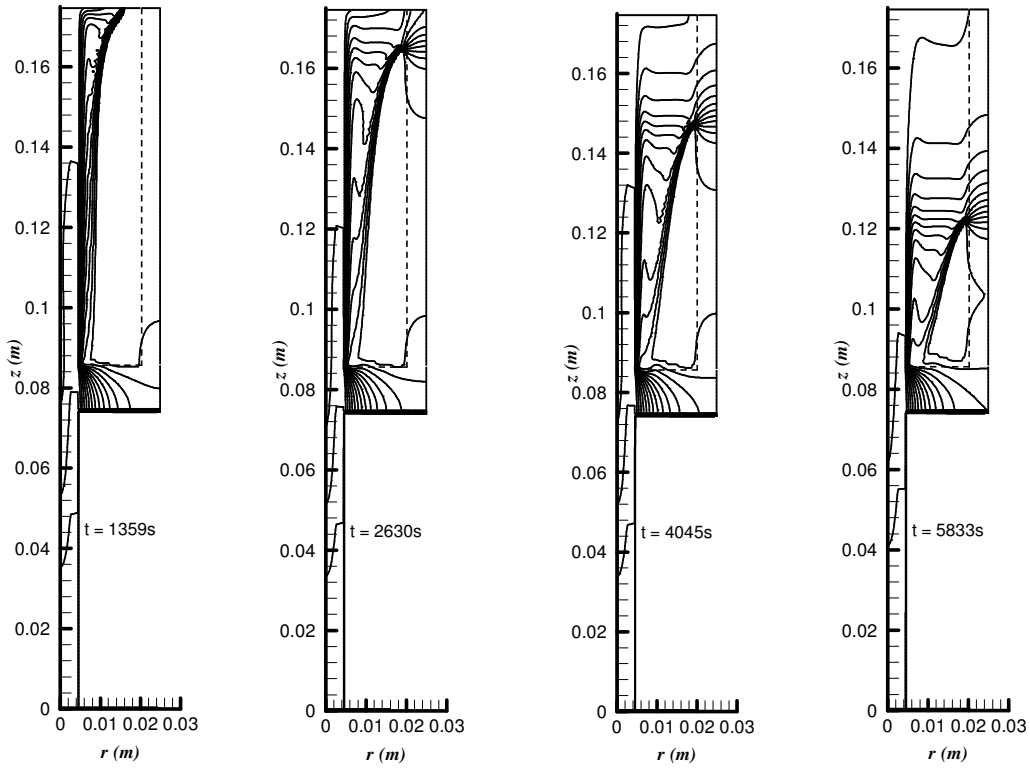
0.16
0.14
0.12
0.1
0.08
0.06
0.04
0.02
0
z (m)
t = 1359s
t = 2630s
t = 4045s
t = 5833s
0 0.01 0.02 0.03
r (m)

(b)

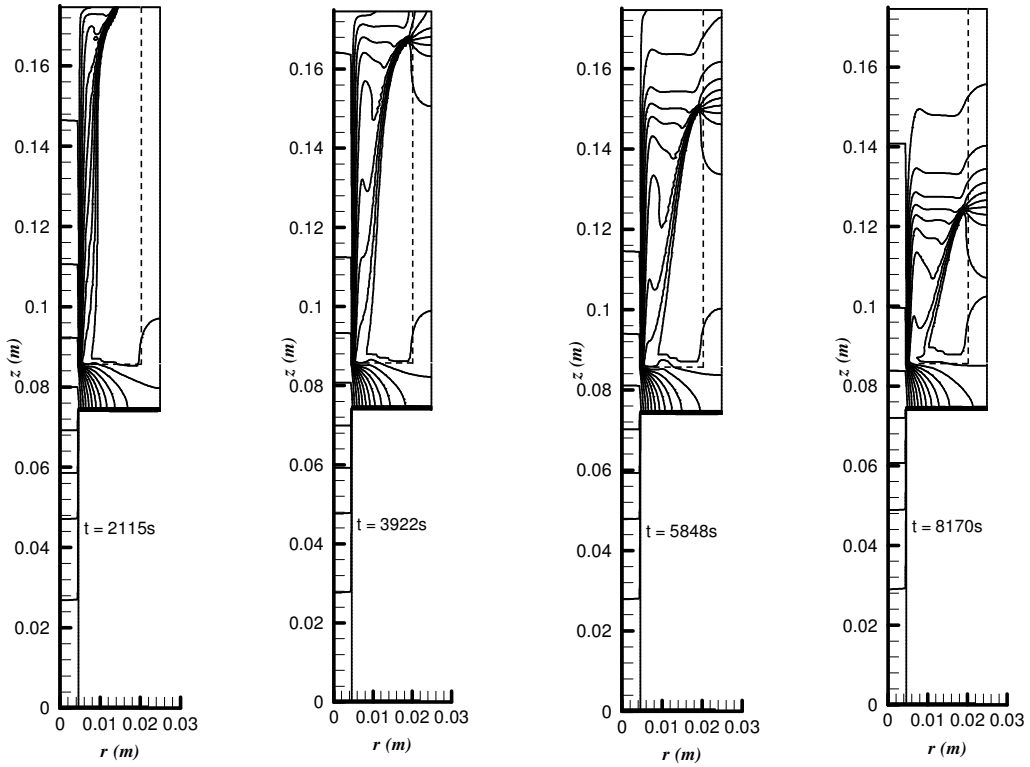

(c)

Fig. 5.4. Predicted temperature distributions for the conditions of Fig. 5.3. Results are for (a) HP-Foil (f_ℓ = 0.0121), (b) HP, and (c) Rod. Isotherms are shown at intervals of 1 K over the range 28°C ≤ T ≤ 45°C for all cases.

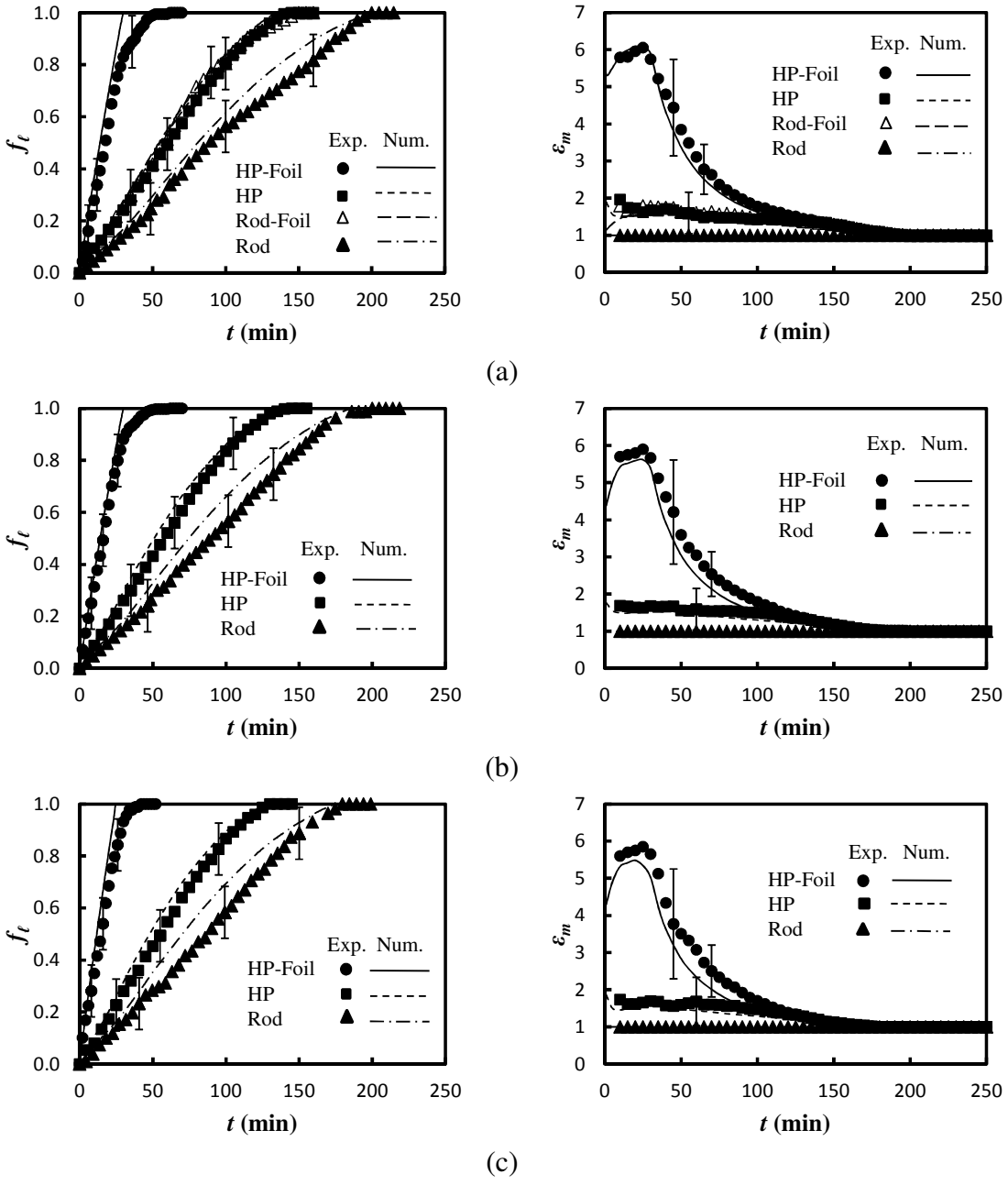

Fig. 5.5. Melting liquid fraction (left) and effectiveness (right) histories for T_{htf} - T_m = 17ºC and f_f = 0.0121: (a) L_t = 90 mm, L_b = 55 mm, (b) L_t = 80 mm, L_b = 65 mm, (c) L_t = 72 mm, L_b = 73 mm.

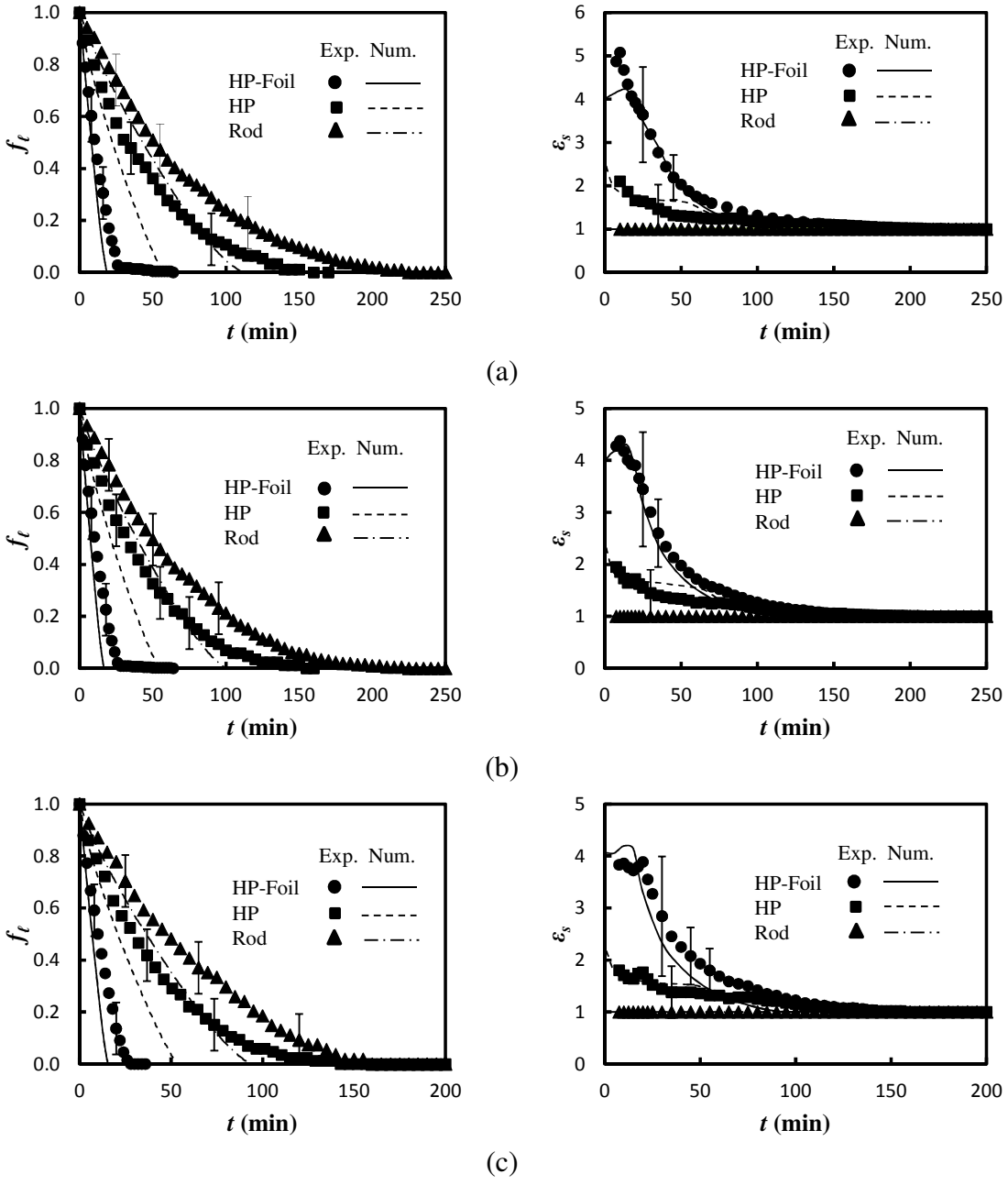

Fig. 5.6. Solidification liquid fraction (left) and effectiveness (right) histories for $T_m - T_{htf} = 17$ºC and $f_f = 0.0121$: (a) $L_t = 90$ mm, $L_b = 55$ mm, (b) $L_t = 80$ mm, $L_b = 65$ mm, (c) $L_t = 72$ mm, $L_b = 73$ mm.

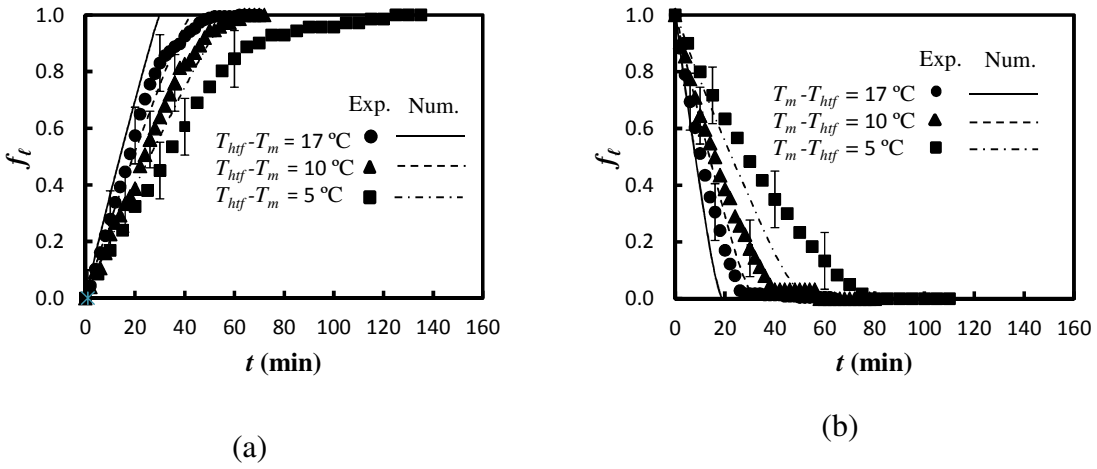

(a) (b)

Fig. 5.7. Liquid fraction histories for the HP-Foil configuration (L_t = 90 mm, L_b = 55 mm, f_f = 0.0121), (a) melting for various T_{htf}-T_m,(b) solidification for various T_m-T_{htf}.

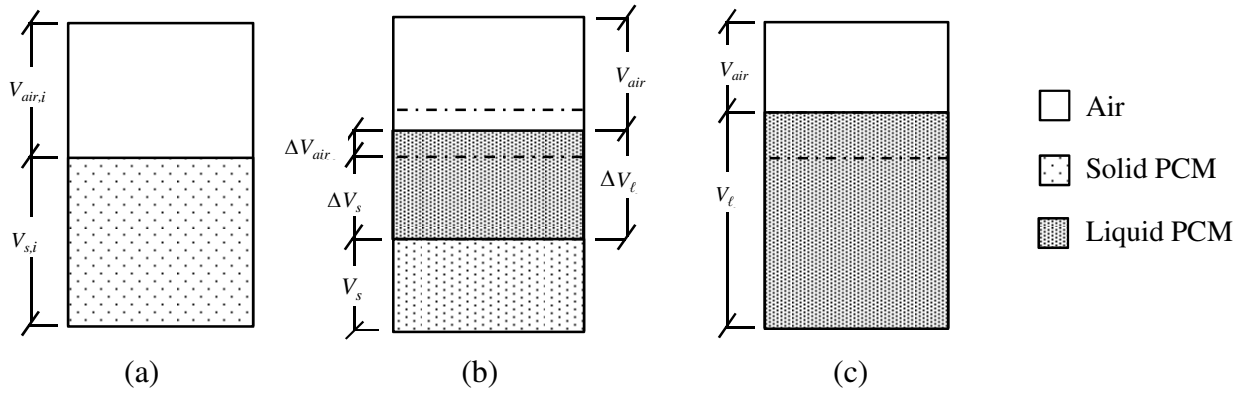

(a) (b) (c)

Fig. 5.A.1. Conceptual melting process: (a) initial (100% solid), (b) solid and liquid PCM, (c) final (100% liquid).

References

[1] B. Zalba, J.M. Marin, L.F. Cabeza, H. Mehling, Review on thermal energy storage with phase change: materials, heat transfer analysis and applications, Applied Thermal Engineering 23 (3) (2003) 251–283.

[2] M.M. Farid, A.M. Khudhair, S.A.K. Razack, S. Al-Hallaj, A review on phase change energy storage: materials and applications, Energy Conversion Management 45 (9–10) (2004) 1597–1615.

[3] S.D. Sharma, K. Sagara, Latent heat storage materials and systems: a review, International Journal of Green Energy 2 (1) (2005) 1–56.

[4] F. Agyenim, N. Hewitt, P. Eames, M. Smyth, A review of materials, heat transfer and phase change problem formulation for latent heat thermal energy storage systems (LHTESS), Renewable and Sustainable Energy Reviews 14 (2) (2010) 615–628.

[5] C.W. Lan, D.T. Yang, Dynamic simulation of the vertical zone-melting crystal growth, International Journal of Heat and Mass Transfer 41 (24) (1998) 4351-4373.

[6] Z. Liu, Z. Wang, C. Ma, An experimental study on heat transfer characteristics of heat pipe heat exchanger with latent heat storage, Part II: Simultaneous charging/ discharging modes, Energy Conversion and Management 47 (7-8) (2006) 967-991.

[7] O. Mesalhy, K. Lafdi, A. Elgafy, K. Bowman, Numerical study for enhancing the thermal conductivity of phase change material (PCM) storage using high thermal conductivity porous matrix, Energy Conversion and Management 46 (6) (2005) 847–867.

[8] J.M. Martin, B. Zalba, L.F. Cabeza, H. Mehling, Improvement of a thermal energy storage using plates with paraffin-graphite composite, International Journal of Heat and Mass Transfer 48 (12) (2005) 2561–2570.

[9] S. Jegadheeswaran, S.D. Pohekar, Energy and exergy analysis of particle dispersed latent heat storage system, International Journal of Energy and Environment 1 (3) (2010) 445–458.

[10] H. Ettouney, I. Alatiqi, M. Al-Sahali, K. Al-Hajirie, Heat transfer enhancement in energy storage in spherical capsules filled with paraffin wax and beads, Energy Conversion and Management 47 (2) (2006) 211–228.

[11] A. Sari, C. Alkan, A. Karaipekli, O. Uzun, Microencapsulated n-octacosane as phase change material for thermal energy storage, Solar Energy 83 (10) (2009) 1757–1763.

[12] M.N.A. Hawlader, M.S. Uddin, M.M. Khin, Microencapsulated PCM thermal energy storage system, Applied Energy 74 (1–2) (2003) 195–202.

[13] M. Lacroix, M. Benmadda, Numerical simulation of natural convection-dominated melting and solidification from a finned vertical wall, Numerical Heat Transfer Part A– Application 31 (1) (1997) 71–86.

[14] M. Lacroix, M. Benmadda, Analysis of natural convection melting from a heated wall with vertically oriented fins, International Journal of Numerical Methods for Heat and Fluid Flow 8 (4) (1998) 465–478.

[15] M.J. Huang, P.C. Eames, B. Norton, Thermal regulation of building-integrated photovoltaics using phase change materials, International Journal of Heat and Mass Transfer 47 (12–13) (2004) 2715–2733.

[16] V. Shatikian, G. Ziskind, R. Letan, Numerical investigation of a PCM-based heat sink with internal fins, International Journal of Heat and Mass Transfer 48 (17) (2005) 3689–3706.

[17] R. Akhilesh, A. Narasimhan, C. Balaji, Method to improve geometry for heat transfer enhancement in PCM composite heat sinks, International Journal of Heat and Mass Transfer 48 (13) (2005) 2759–2770.

[18] M. Gharebaghi, I. Sezai, Enhancement of heat transfer in latent heat storage modules with internal fins, Numerical Heat Transfer Part A – Application 53 (7) (2008) 749–765.

[19] N. Sharifi, T.L. Bergman, A. Faghri, Enhancement of PCM melting in enclosures with horizontally-finned internal surfaces, International Journal of Heat and Mass Transfer 54 (19–20) (2011) 4182–4192.

[20] A. Faghri, Heat Pipe Science and Technology, Taylor & Francis, Washington, D. C., 1995.

[21] A. Faghri, Thermal Energy Storage Heat Exchanger, US Patent No. 4976308, 1990.

[22] A. Faghri, Micro Heat Pipe Energy Storage System, US Patent No. 5000252, 1991.

[23] B. Horbaniuc, G. Dumitrascu, A. Popescu, Mathematical models for the study of solidification within a longitudinally finned heat pipe latent heat thermal storage system, Energy Conversion and Management 40 (15–16) (1999) 1765–1774.

[24] Z. Liu, Z. Wang, C. Ma, An experimental study on heat transfer characteristics of heat pipe heat exchanger with latent heat storage. Part I: charging only and discharging only modes, Energy Conversion and Management 47 (7–8) (2006) 944–966.

[25] H. Shabgard, T.L. Bergman, N. Sharifi, A. Faghri, High temperature latent heat thermal energy storage using heat pipes, International Journal of Heat and Mass Transfer 53 (15–16) (2010) 2979–2988.

[26] C.W. Robak, T.L. Bergman, A. Faghri, Enhancement of latent heat energy storage using embedded heat pipes, International Journal of Heat and Mass Transfer 54 (15–16) (2011) 3476–3484.

[27] N. Sharifi, S. Wang, T.L. Bergman, A. Faghri, Heat pipe-assisted melting of a phase change material, International Journal of Heat and Mass Transfer 55 (13–14) (2012) 3458–3469.

[28] C. Guo, W. Zhang, Numerical simulation and parametric study on new type of high temperature latent heat thermal energy storage system, Energy Conversion and Management 49 (5) (2008) 919–927.

[29] R. Bayón, E. Rojas, L. Valenzuela, E. Zarza, J. León, Analysis of the experimental behaviour of a 100 kWth latent heat storage system for direct steam generation in solar thermal power plants, Applied Thermal Engineering 30 (17–18) (2010) 2643-2651.

[30] M. Sugawara, Y. Komatsu, Y. Takahashi, Freezing enhancement around a horizontal tube using copper foil disks, Heat and Mass Transfer 47 (12) (2011) 1691-1698.

[31] R.S. Figliola, D.E. Beasley, Theory and Design for Mechanical Measurements, fourth ed., Wiley, Hoboken, 2006, pp. 148–190.

[32] A. Faghri, Y. Zhang, Transport Phenomena in Multiphase Systems, Academic Press, Elsevier, New York, 2006.

[33] A. Faghri, Y. Zhang, J. Howell, Advanced Heat and Mass Transfer, Global Digital Press, Columbia, Missouri, 2010.

[34] Y. Cao, A. Faghri, Transient two-dimensional compressible analysis for high-temperature heat pipes with pulsed heat input, Numerical Heat Transfer Part A - Applications 18 (4) (1990a) 483-502.

[35] T.L. Bergman, A.S. Lavine, F.P. Incropera, D.P. Dewitt, Fundamentals of Heat and Mass Transfer, seventh ed., Wiley, Hoboken, 2011.

[36] The engineering toolbox, website: http://www.engineeringtoolbox.com/